# THE EFFECT OF ACTIVATION ON THE DEACTIVATION OF A PRECIPITATED IRON BASED CATALYST

By

**JEZREEL CLOETE**
M.Sc. (Chemistry) (University of the Western Cape)

Supervisor: Professor Eric Van Steen

Thesis submitted for the Taught Masters in Catalysis degree in the Department of Chemical Engineering at the University of Cape Town.

August 2009

# Declaration

I know the meaning of plagiarism and declare that all the work in this document, save for that which is properly acknowledged, is my own.

_____

Jezreel Cloete

August 2009

# Acknowledgments

I would like to thank the following people and organisations for their help and support throughout this study:

Prof. Eric van Steen for his assistance and guidance as supervisor.

Sasol Technology, Research and Development Division for funding this research project.

Colleagues at Sasol Technology; Don Hauman, Ryno Kotze, Dr Johan Huyser, Dr Sam Mahomed, Stanley Manzini, Siyanda Lubhelwana and Willem Erasmus.

Kiara Maharaj.

# Abstract

There has been renewed interest in the Fischer-Tropsch process since diesel fuel derived from natural gas Fischer-Tropsch processes can meet the proposed future legislation standards for sulphur emissions without further processing. Oil refineries producing diesel fuel on the other hand would have to invest $4 – 13 billion to meet the proposed sulphur content requirements. Also, Fischer-Tropsch processes using coal as a feedstock could become an attractive alternative to oil refining due to the large differential between crude oil and coal prices.

Iron-based and cobalt-based catalysts are the most commonly used metals for commercial Fischer-Tropsch processes with the choice of whether to utilize an iron- or cobalt-based catalyst depending largely on the source from which the synthesis gas has been derived. Iron-based catalysts are well suited for the conversion of low hydrogen content ($H_2$/CO ratios of *ca.* 0.70 – 1.50) synthesis gas such as that derived from coal. Thus iron-based catalysts would be the preferred choice to produce diesel fuel *via* the coal-to-liquids process.

A study was undertaken in order to investigate the effect of low hydrogen content synthesis gas (as would be derived from coal) on the performance and lifetime of an iron-based catalyst during the low temperature Fischer-Tropsch process. In particular, the effect of the activation procedure on the lifetime of the iron-based catalyst (deactivation behaviour) was investigated.

It was hypothesized that although CO, according to literature, is a superior activating gas, it results in more rapid catalyst deactivation due to carbon deposition. Therefore, when using a CO rich gas as activating gas, deactivation would be due to the high CO content which leads to fouling of the catalyst due to carbon deposition.

It was however found that the combination of activating gas and $H_2/CO$ ratio of the synthesis gas during the Fischer-Tropsch synthesis determined the deactivation behaviour of the catalyst. CO activation resulted in superior catalyst activity provided, however, that the synthesis gas during the Fischer-Tropsch synthesis had a high $H_2/CO$ ratio. If CO activation was followed by the Fischer-Tropsch synthesis with a low $H_2/CO$ ratio synthesis gas, comparatively lower Fischer-Tropsch activity was achieved with deactivation also setting in from very soon after switching to Fischer-Tropsch synthesis conditions. Thus the $H_2/CO$ ratio of the synthesis gas during the Fischer-Tropsch synthesis appears to be the key factor if a catalyst was activated with CO; carbon deposition due to a low $H_2/CO$ ratio of the synthesis gas most likely leading to more rapid deactivation. Deactivation rate equations, including that which would describe deactivation due to carbon deposition, were fitted to the data obtained for each run. The deactivation rate equations fitted the actual data quite well and therefore could support the speculation that deactivation in a catalyst activated with CO and subjected to the Fischer-Tropsch synthesis with a low $H_2/CO$ ratio is due to carbon deposition.

Furthermore it was speculated that carbon deposition resulted in the inhibition of the cycle of dynamic transitions proposed by van Steen *et al.* (2008) which is required to maintain activity of a precipitated iron-based Fischer-Tropsch catalyst. The inhibition of these dynamic transitions could then lead to other contributing deactivation mechanisms such as sintering.

# TABLE OF CONTENTS

# LIST OF TABLES

# LIST OF FIGURES

## 1 INTRODUCTION

# 1 Introduction

## 1.1 Background

The Fischer-Tropsch synthesis is the process whereby synthesis gas (a mixture of $H_2$ and CO) is transformed into hydrocarbon products over a transition metal catalyst. It is in principle a carbon chain building process where *e.g.* $CH_2$ groups are added to a carbon chain. The resulting overall reaction can be represented as follows[1]:

$$nCO + 2nH_2 \rightarrow (-CH_2-)_n + nH_2O \qquad (1.1)$$

The major purpose of the process is to produce what is known as synthetic fuel which is derived, not from crude oil, but from coal, natural gas or biomass. The Fischer-Tropsch process is an established technology, being originally invented during the 1920's by Franz Fischer and Hans Tropsch to produce liquid fuels in petroleum-poor Germany. It was commercially operated in Germany during World War II, reaching a production of more than 124 000 barrels per day by 1944. The product distribution of the Fischer-Tropsch process can be shifted depending on the operating conditions. High temperature Fischer-Tropsch synthesis (HTFT) is performed at temperatures between 320-350°C at *ca*. 20-40 bar utilizing a fused iron catalyst. The main products in this process are short chain hydrocarbons ($C_3$ – $C_{11}$) to be used as petrol and as feedstock for the chemical industry. Low temperature Fischer-Tropsch synthesis (LTFT) is performed at temperatures between 200-270°C at *ca*. 10-30 bar utilizing either a cobalt-based or an iron-based catalyst[2]. The desired products in this process are long chain hydrocarbons, *i.e.* waxes ($>C_{20}$), which can subsequently be hydrocracked to produce diesel. A general process flow diagram as well as the different types of reactors used for the Fischer-Tropsch process is shown in Figure 1.1[3].

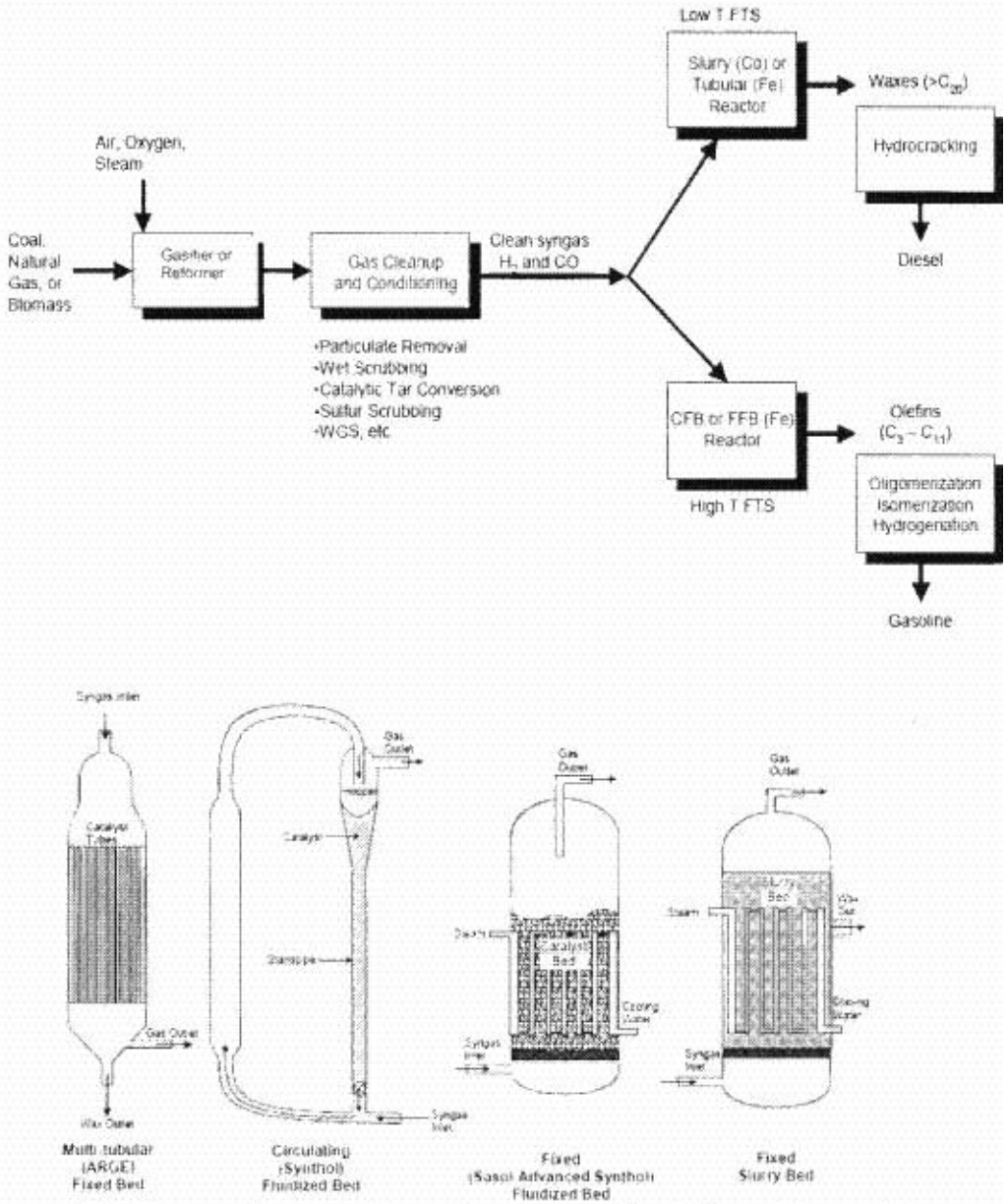


**Figure 1.1** General process flow diagram and the different types of reactors used for the Fischer-Tropsch process[3]

Both the high temperature and low temperature Fischer-Tropsch process was applied in South Africa during the country's Apartheid era (during which, amongst other sanctions, an oil embargo against the country was in place) to cover its energy needs. The petrochemical company Sasol was founded in 1950 to commercialize the Fischer-Tropsch process and today it provides most of South Africa's diesel fuel requirements. It currently

operates the only commercial coal-to-liquids (CTL) facility in the world with a capacity of 150 000 barrels per day as well as the largest gas-to-liquids (GTL) facility in the world. The recently opened Oryx GTL plant in Qatar is a joint venture between Qatar Petroleum (51%) and Sasol (49%) and has a potential production of 34 000 barrels per day (with plans to expand this by a further 100 000 barrels per day). Sasol is thus the leading company in the commercialization of synthetic fuel using the Fischer-Tropsch process[4].

Also based in South Africa, PetroSA produces diesel, distillates and alcohols of which *ca.* 3000 barrels per day are exported to the US, Europe, the Caribbean and the Middle and Far East. Shell also utilizes the Fischer-Tropsch process at its medium scale commercial facility in Bintulu, Malaysia operating since 1993. It produces 14,700 barrels per day of liquid products. Table 1.1 gives a summary of existing and planned plants for Fischer-Tropsch synthesis[4]. Other companies involved in Fischer-Tropsch activities include Syntroleum, ExxonMobil, Rentech, BP, Chevron, ConocoPhilips and Statoil.

**Table 1.1** Existing plants and plants under construction for Fischer-Tropsch Synthesis[4]

| Company | Site | Capacity [bpd (kt/a)] | Raw Material | Commissioning Date |
|---|---|---|---|---|
| Sasol | Sasolburg | 2500 (120) | Natural Gas* | 1955 |
| Sasol | Secunda | 85000 (4000) | Coal | 1980 |
| Sasol | Secunda | 85000 (4000) | Coal | 1982 |
| PetroSA | Mossel Bay | 30000 (1400) | Natural Gas | 1992 |
| Shell | Bintulu | 15000 (700) | Natural Gas | 1993 |
| Sasol/Qatar Petroleum | Qatar | 34000 (1600) | Natural Gas | 2006 |
| **Under Construction** | | | | |
| SasolChevron | Escravos | 34000 (1600) | Natural Gas | 2009 |
| Shell | Qatar | 140000 (6500) | Natural Gas | 2009 |

*Coal utilized as raw material until 2004

Fischer-Tropsch technology is associated with high capital, operational and maintenance costs. Its economic viability is determined by the fluctuating crude oil price and the price of feedstock (i.e. natural gas, coal or biomass).

Natural gas as a feedstock for the Fischer-Tropsch process is only economically viable if it is too expensive to transport (either by utilizing pipelines or by liquefaction) to a particular market. Hence, Fischer-Tropsch GTL technology will be typically used for remote, stranded gas fields. Capital costs for GTL projects currently tend to be double that of oil refineries at between $20 000 and $30 000 per daily barrel of capacity (as compared with oil refinery costs of $12 000 to $14 000 per daily barrel)[5]. Typical estimates indicate that expected oil prices would have to consistently average above $20 per barrel to allow positive economic returns from a GTL project. However future air pollution regulations for Europe and North America, which will require very low to zero sulphur content of diesel (in view of diesel powered motor vehicles and light trucks expanding their market shares and consequently increasing their fuel needs), may result in future GTL projects being economically viable. This is because diesel fuel derived from GTL processes can meet the standards for sulphur emissions without further processing whereas oil refineries producing diesel fuel would have to invest $4 – 13 billion to meet the proposed sulphur content requirements. Therefore as demand for ultra clean fuels increases, it is likely that the ultra clean fuels produced by Fischer-Tropsch GTL processes can command premium prices, allowing GTL investments to be profitable[5].

For Fischer-Tropsch CTL technology, crude oil prices averaging above $80 – 100$ per barrel are needed to generate a 20% return on investment[6]. At present however, a factor that plays a major role in making CTL technology attractive, is the large differential between crude oil and coal prices (Figure 1.2)[6] combined with the fact that the two largest oil consumers in the world –

the USA and China – are also the two most coal-rich countries in the world (Figure 1.3)[6]. Thus if operating at an adequate scale (at least *ca.* 50 000 barrels per day) together with remote coal reserves having no alternative value, CTL derived fuels will make an attractive alternative to crude oil derived fuels. Although the associated formation of $CO_2$ due to coal gasification (the gas produced from a Lurgi dry ash gasifier operating at 1000°C contains approximately 32% $CO_2$) could pose environmental risks, potential technological breakthroughs such as underground gasification of coal could help in managing emissions and also significantly improve CTL economics[7, 8].

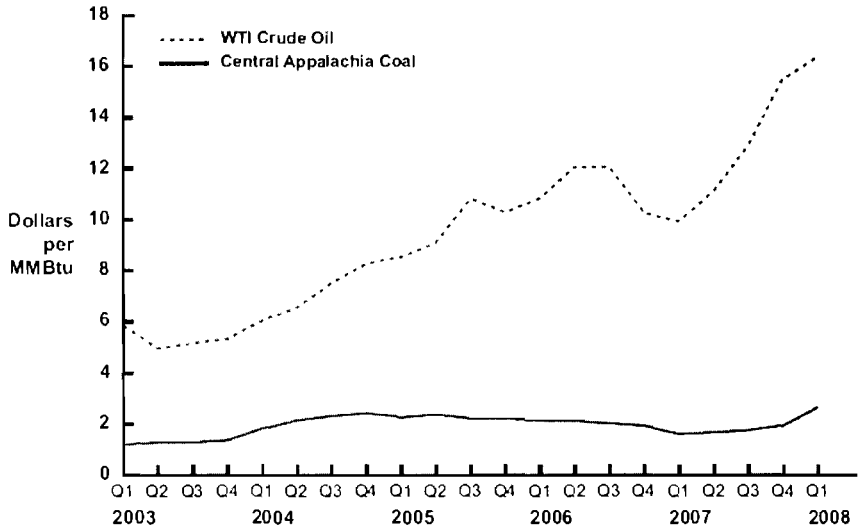


**Figure 1.2** Difference in crude oil and US coal prices (MMBtu = million British thermal units)[6]

The choice of whether to utilize an iron- or cobalt-based catalyst depends largely on the source from which the synthesis gas has been derived. Iron-based catalysts are well suited for the conversion of low hydrogen content ($H_2/CO$ ratios of *ca.* 0.70 – 1.50) synthesis gas such as that derived from coal. This is due to iron's promotion of the water-gas shift (WGS) reaction which occurs simultaneously with the production of hydrocarbons during Fischer-Tropsch synthesis (FTS) and which then increases the hydrogen to carbon ratio. The overall process therefore proceeds as follows[1]:

$$\text{FTS: } nCO + 2nH_2 \rightarrow (-CH_2-)_n + nH_2O \qquad (1.1)$$

$$\text{WGS: } CO + H_2O \rightarrow H_2 + CO_2 \qquad (1.2)$$

Thus with an iron-based catalyst the $H_2/CO$ ratio in the reactor can be adjusted using the WGS reaction although, if the WGS rate is too high, it can result in a loss in carbon yield of the liquid fuel product due to the conversion of a larger amount of CO to $CO_2$[1].

For conversion of synthesis gas with a higher hydrogen content ($H_2/CO$ ratios of *ca.* 2.0) as derived from natural gas, cobalt-based catalysts are preferred. With cobalt-based catalysts the WGS reaction does not occur and hence the conversion of CO to the desired long chain products at higher $H_2/CO$ ratios is more efficient *i.e.* a higher conversion per pass can be achieved with a cobalt-based catalyst when having a higher $H_2/CO$ ratio as compared with an iron-based catalyst under the same conditions[1].

Another factor to take into consideration when deciding which metal to use as catalyst for the Fischer-Tropsch synthesis is the fact that these catalysts are extremely sensitive to the presence of sulphur containing compounds. Sulphur poisoning of catalysts is one of the most serious deactivation problems in Fischer-Tropsch synthesis using synthesis gas derived from coal or biomass. A few ppm of $H_2S$ may reduce catalyst activity within a few hours and reduce catalyst lifetime by weeks[11]. Sulphur adsorbs so strongly

on metals and prevents or modifies the further adsorption of reactant molecules leading to the substantial or complete loss of activity in many reactions. Different sulphur species poison the catalyst to a different extent depending on the number of electron pairs available for bonding and the degree of shielding of the sulphur ion by ligands[11]. Therefore the order of decreasing toxicity for poisoning of a given metal by different sulphur species is $H_2S$, $SO_2$, $SO_4^{2-}$; which is in the order of increased shielding by oxygen. Figure 1.4 shows the steady-state methanation activities of Ni, Co, Fe and Ru relative to gas phase $H_2S$ concentration[11]. From this we can see that the sulphur tolerances of these metals are extremely low; showing 3-4 orders of magnitude loss in activity at 15 – 100 ppb concentrations of $H_2S$.

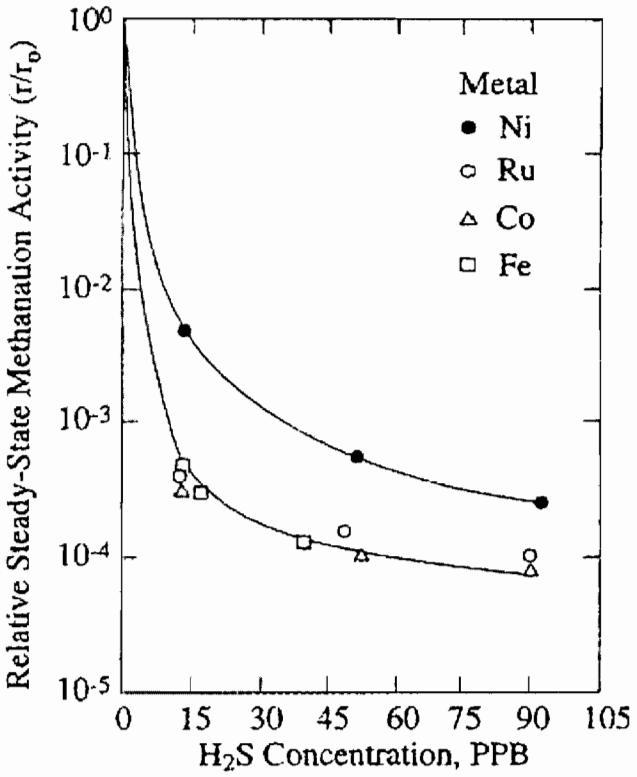


**Figure 1.4** Steady-state methanation activities of Ni, Co, Fe and Ru relative to gas phase $H_2S$ concentration[11]

prevent sintering and maintaining the catalyst particle size. Furthermore, the catalyst typically contains potassium, sodium, lithium, magnesium or calcium as a chemical promoter to enhance its activity and reduce the methane selectivity. The catalyst is typically spray-dried to obtain the required particle size distribution[2].

The high temperature Fischer-Tropsch process utilizes a fused iron catalyst. It is prepared by the fusion of iron oxide together with a chemical promoter such as $K_2O$ (to enhance catalyst activity and selectivity) and structural promoters such as MgO or $Al_2O_3$ (to enhance the surface area of the final catalyst). In the process a molten mixture of iron oxides and of the chemical and structural promoters are poured into ingots and rapidly cooled. The ingots are then crushed in a ball mill to the required particle size distribution for the fluidization in HTFT reactors. These catalysts have a high selectivity towards olefins and appear stable under high $H_2/CO$ syngas ratios. However there is excessive carbon formation on these catalysts, the elimination or reduction of which remains a challenge[2].

As mentioned in Section 1.1, diesel powered motor vehicles and light trucks are expanding their market shares and consequently increasing their fuel needs along with imminent stricter legislation regarding the sulphur content of diesel fuel. With ever increasing crude oil prices GTL or CTL derived diesel will make an attractive alternative to crude oil derived diesel since, along with already meeting the standards for sulphur emissions without further processing, further potential technological breakthroughs such as underground gasification of coal are making the economics of Fischer-Tropsch technology increasingly attractive. Added to this, vast coal reserves (Figure 1.3) with no alternative economic value suggests that there is great business potential to be gained by especially CTL technology.

It can thus be deduced that for CTL applications iron-based catalysts would be a potential catalyst for the conversion of coal using the low temperature Fischer-Tropsch process to produce diesel. Hence the focus of the rest of this work will be on precipitated iron-based catalysts.

#### 1.1.1.2 Composition of Precipitated Iron Catalysts

A typical iron-based catalyst for the low temperature Fischer-Tropsch process contains 25g $SiO_2$, 5g Cu and 5g $K_2O$ per 100g Fe. At this large ratio of $Fe/SiO_2$ (4 g/g) silica is not a classical support but rather acts as a binder and as a spacer, the latter inhibiting sintering of the high area iron oxide in the catalyst precursor[2].

#### 1.1.1.3 General Preparation of Precipitated Iron Catalysts

The precipitated iron catalyst can either be prepared in a batch process or in a continuous process. In the batch process a near boiling solution of iron and copper nitrate is rapidly poured into a hot solution of $Na_2CO_3$ with vigorous stirring until the pH reached is just below 7. In the continuous process a stream of metal nitrate solution is continuously mixed with a stream of sodium carbonate solution maintaining the pH at *ca.* 7[2].

The precipitate (mainly hydrated ferric oxide) is thoroughly washed with hot distilled water to remove the bulk of the sodium ions. The precipitate is then re-slurried with water and the appropriate amount of potassium waterglass is added to give the desired silica to iron ratio. Sufficient nitric acid is then added to the slurry so that after filtration the desired amount of $K_2O$ is retained by the gel-like catalyst cake. Investigation at Sasol indicated that when the potassium waterglass is added to the slurried hydrated ferric oxide precipitate, all the silica is precipitated or adsorbed onto the high area iron precipitate as subsequent washing can remove all of the potassium but none of the silica[2]. Thus it appears that the addition of nitric acid is to control the $K_2O$ content of the catalyst and not to precipitate the silica. Both the

BET surface area and total pore volume is increased as the silica content is increased[2].

The precipitate is subsequently spray-dried to produce spherical particles which are then calcined in a rotary kiln.

## 1.2. Catalyst Activation

Unlike the other Group VIII metals (Co, Ni, Ru) which remain in the metallic state during Fischer-Tropsch synthesis, iron catalysts tend to form a number of chemical phases, including various iron oxides and iron carbides during synthesis. Control of these phase transformations might be important in maintaining catalytic activity.

### 1.2.1 Effect of Activation Gas on Initial Activity and Productivity

After catalyst preparation the Fe catalyst for Fischer-Tropsch synthesis has to be transformed into its active form since the metal is typically still present as an oxide in the catalyst precursor. Hence the catalyst precursor is pre-reduced (or activated) under relatively mild conditions. In general there are three approaches employed for catalyst activation utilizing either CO, $H_2$ or syngas as the activating gas. The conditions for the pretreatment of the iron-based catalyst used for low temperature slurry phase Fischer-Tropsch synthesis have significant effects on its activity and selectivity[12].

Davis and co-workers found that activation in CO at 270°C for 24 h will provide close to the maximum conversion of a particular precipitated catalyst as compared to that obtained by other activation procedures and that in general, activation in syngas leads to a catalyst with lower activity than one activated in CO[13]. This is illustrated in Figure 1.5 which compares the initial percentage CO converted after activation as a function of $H_2$ partial pressure in the activating gas.

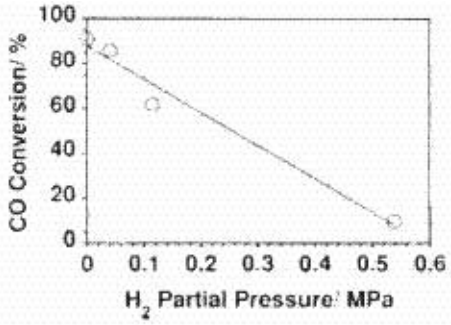


**Figure 1.5** CO conversion following activation with a syngas containing various partial pressures of $H_2$[13]

The data obtained in Figure 1.5 was for a catalyst that did not contain any copper (which is usually incorporated into iron-based catalysts to promote reduction). It was further found that even at a low $H_2$/CO ratio of ~0.70 initial activity was not as good as compared to when activating with CO. With copper added there was an improvement in initial activity when activating with syngas, but it was still not comparable to the initial activity obtained with CO activation.

Comparing $H_2$ activation to CO and syngas activation, Luo and Davis found that $H_2$ activation yielded the lowest CO conversion of the three[14]. This is shown in Figure 1.6 where percentage CO conversion is plotted as a function of time on stream.

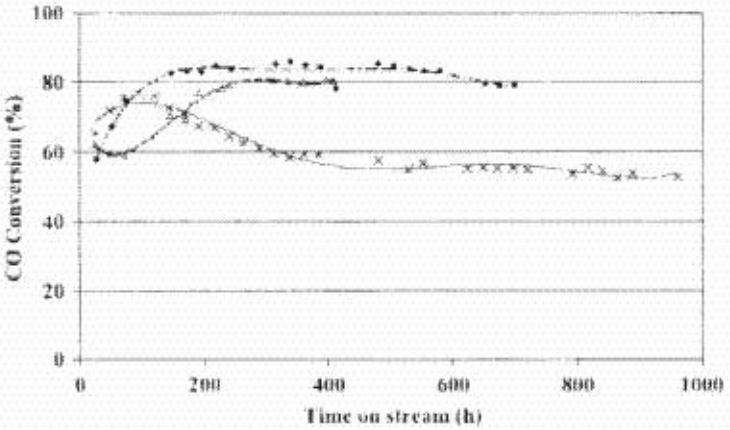


**Figure 1.6** Influence of activation gas type on CO conversion (♦ = CO activation, x = hydrogen activation, Δ = syngas activation – $H_2$/CO = 0.70)[14]

Bukur and co-workers' findings[15] regarding activity after activation with $H_2$, CO or syngas were similar to those of Luo and Davis[14]. Their results are presented in Figure 1.7. They found that the highest steady-state activity was achieved on the CO activated catalyst, followed by syngas pretreatment, with the $H_2$ activated catalyst being the least active.

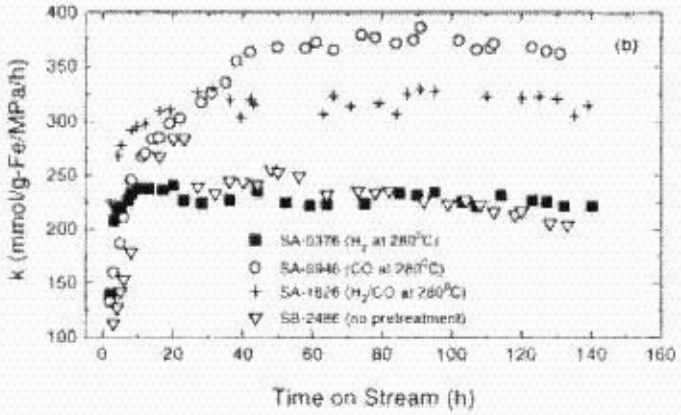


**Figure 1.7** First-order reaction rate constant with time-on-stream after different pretreatments[15]

It was however also found that the activity of $H_2$ reduced catalysts were very sensitive to the reduction conditions employed[15]. Figure 1.8 shows the effect on activity on a catalyst activated with $H_2$ at temperatures of 240, 250 and 280°C. By using a moderate temperature (250°C) the activity was found to be comparable to that of CO or syngas activated catalysts as shown in Figure 1.7.

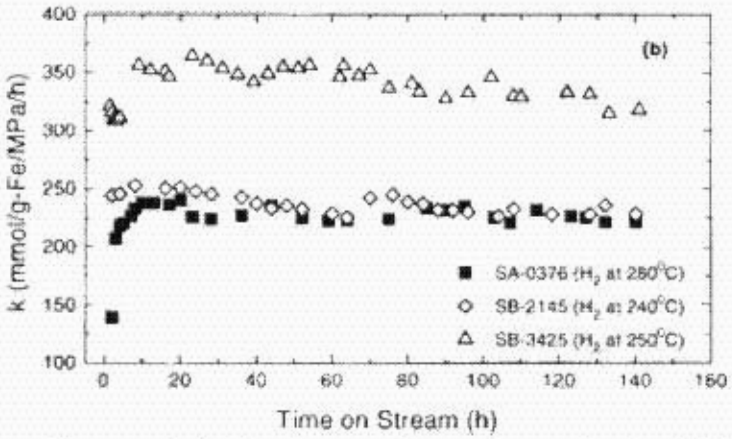


**Figure 1.8** Change in first-order reaction rate constant with time on stream for $H_2$ reduced catalysts at various temperatures[15]

In addition Luo and Davis[14] found that the gas used for activation also has an effect on hydrocarbon productivity; CO activation showing the best overall hydrocarbon productivity while the lowest productivity was obtained with $H_2$ activation (Figure 1.9).

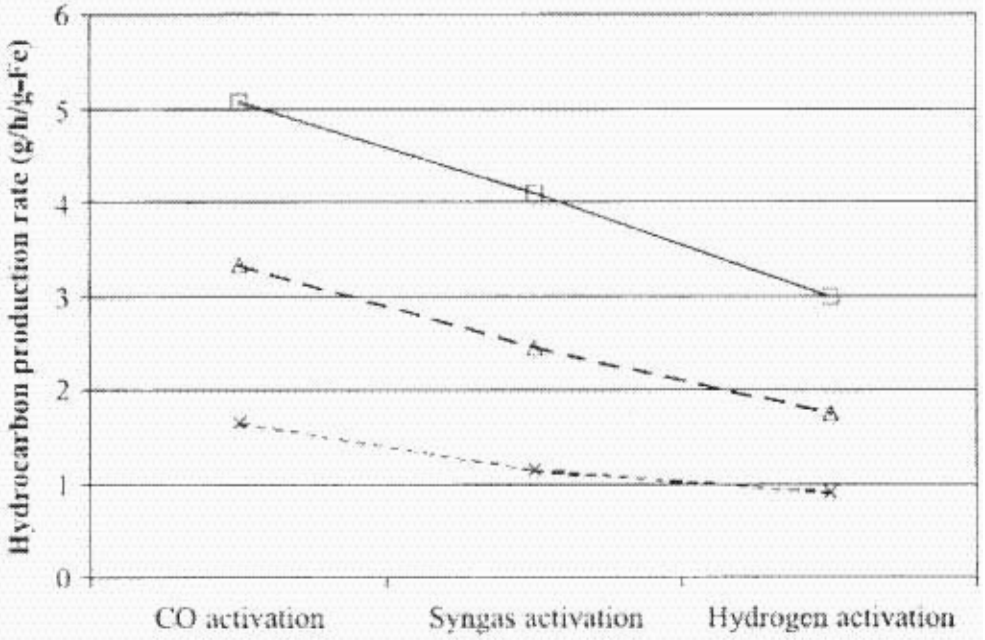


**Figure 1.9** Influence of activation gas on hydrocarbon production rate (FTS conditions: 270°C and 13 bar, activation: x = 230°C, Δ = 250°C, □ = 270°C)[14]

### 1.2.2 Phase Transformation of Fe Catalyst during Activation

It has been observed that hematite ($\alpha$-$Fe_2O_3$) in the iron-based catalyst precursor transforms to magnetite ($Fe_3O_4$) during activation[16]. This happens irrespective of the gas used during the activation process. Then, depending on the gas used during activation, the Fe-catalyst transforms from $Fe_3O_4$ to either iron carbide with different phases, or metallic iron. Figure 1.10 is a schematic representation of the morphological changes that accompany the phase changes that $\alpha$-$Fe_2O_3$ undergoes as a result of activation and reaction conditions.

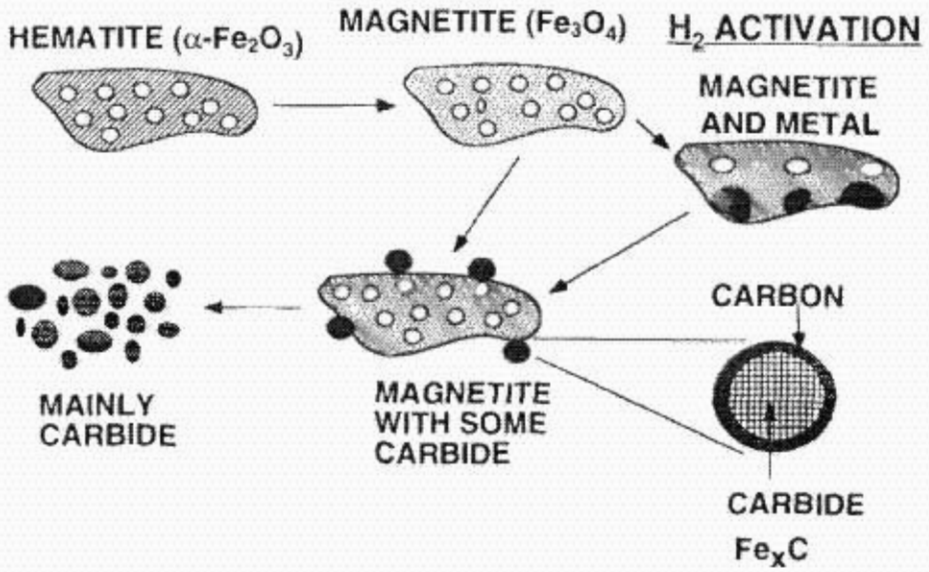


**Figure 1.10** Schematic representation of the morphological changes that accompany the phase changes that $\alpha$-$Fe_2O_3$ undergoes as a result of activation and reaction conditions[16]

Although there is continuing debate regarding the actual nature of the active phases, a correlation between the carbide content and FT activity has been established[17] with two models having been proposed to explain the role of the carbide phase.

The carbide model[18] proposes that FT synthesis occurs on the surface of a bulk iron carbide phase. It was found that the density of these sites was dependent on the extent of bulk carburization. The competition model[17] proposes that one or more carbon atoms together with metallic iron form the active site at which the carbon atoms are hydrogenated. Iron carburization and hydrocarbon formation from surface carbon containing species occur simultaneously in a competitive reaction. In both models, iron carbide formation needs to occur to result in an active FT synthesis catalyst.

The transformation of hematite into magnetite is relatively fast and is complete within 2 h at 543K whether the activation is carried out using $H_2$, CO or syngas. The subsequent transformation from magnetite to carbide is slow and is dependent on the activation environment. The carbide phase forms as small nodules on the surface of the magnetite with the phase transformation proceeding slowly into the bulk[16]. Based on this, and further work done by Davis, a general model for a stable iron catalyst during synthesis was proposed (see Figure 1.11)[13].

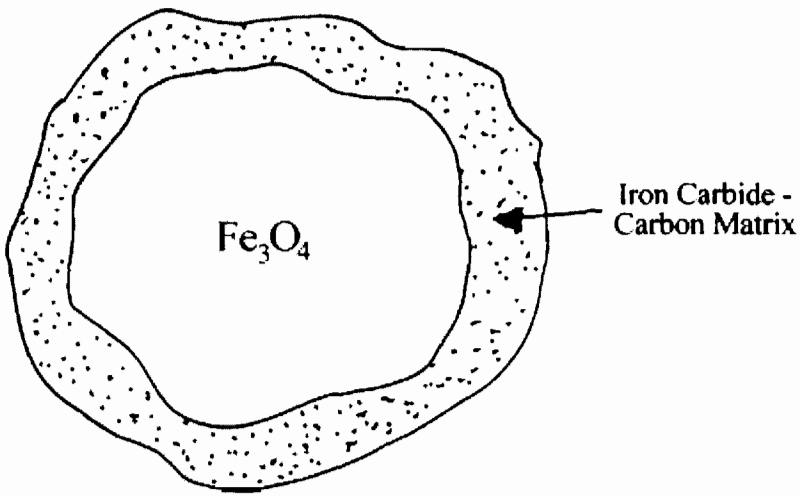


**Figure 1.11** Schematic of the phases present in a stable iron catalyst during synthesis

Further refining the general model for a stable iron catalyst, Bengoa *et al* proposed the evolution to a working catalyst at the steady state by studying the reduction of a supported iron catalyst[19]. The support used was glassy carbon which has very low metal-support interaction. This enabled them to obtain complete iron reduction which could be used as a reference for samples reduced to a lesser extent. Characterization of these fully and partially reduced catalysts by means of XRD, CO chemisorption, Atomic Absorption, Nitrogen Adsorption and Mössbauer spectroscopy enabled the piecing together of the steps in Figure 1.12.

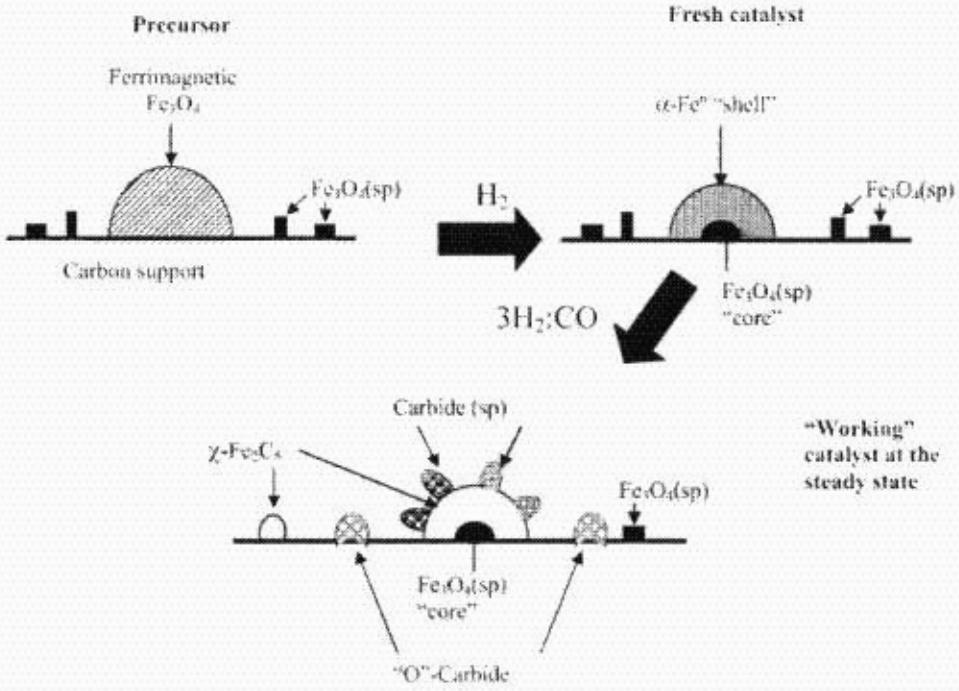


**Figure 1.12** Steps followed to reach the structure of the working catalyst at steady state[19]

The difference in Fischer-Tropsch activity of a catalyst with significant carbide phase and a material that is essentially magnetite is illustrated by Figure 1.13[13]. Here an iron catalyst was activated with synthesis gas and showed low (20%) CO conversion during approximately 100 h of synthesis. Samples of catalyst withdrawn during this period showed that it consisted mainly of the magnetite phase. After 100 h the catalyst was exposed to only

CO for 24 h which resulted in a material that contained *ca.* 35% carbide phase. This brought about an increase in CO conversion of ~70% (from ~20% to ~90%).

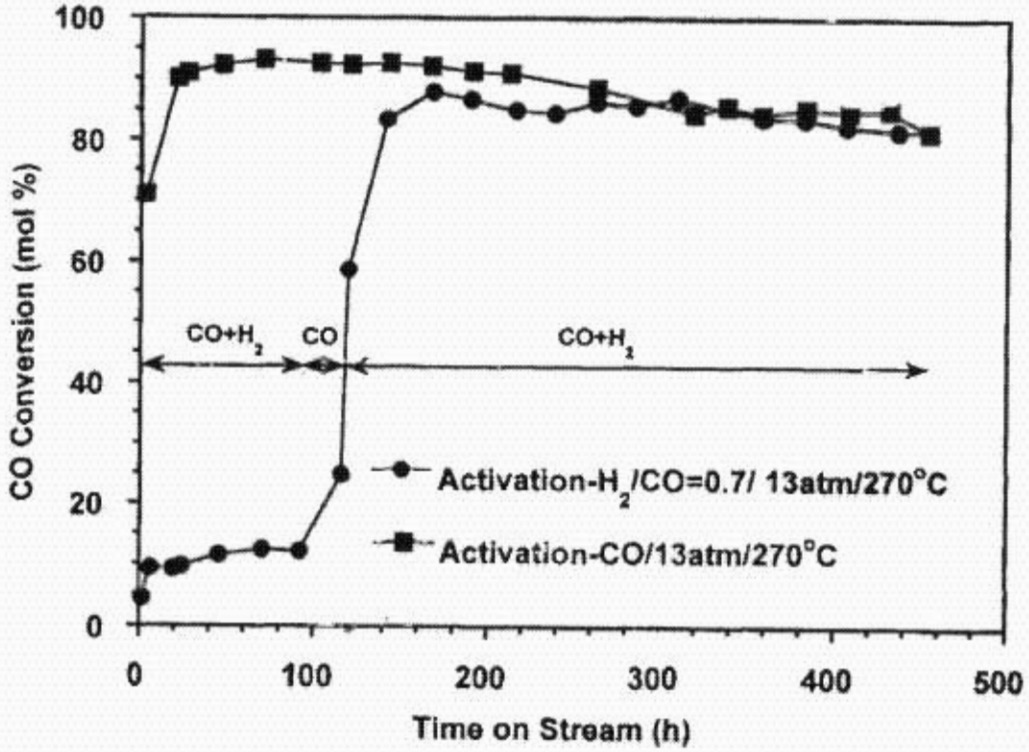


**Figure 1.13** CO conversion for portions of the same catalyst activated in CO (■) and in syngas ($H_2$/CO = 0.71) followed by activation in CO following about 100 h of synthesis (●)

Bukur *et* al. also found that the extent of reduction, as measured by the relative metallic iron content of the sample, was fairly low with hydrogen reduction even after long times at high temperatures[15]. The reduction rate was found to be significantly higher with CO or syngas. Work done by Shroff *et al.* also indicated that the reduction rate was higher when using CO as the reducing gas[16]. They showed that at 543K and *ca.* 1 bar pressure, CO activation transforms the iron oxide into the carbide phase most rapidly and hence results in the most active catalyst. Partial reduction with $H_2$ resulted in an active catalyst after an induction period required for carbide formation.

Activation with syngas was found to be the slowest when done at a reaction temperature of 543K thereby necessitating the need for syngas activation to be carried out at a slightly higher temperature to obtain higher catalyst activities at shorter times. Figure 1.14 is a schematic representation of the differences in the extent of transformation caused by different activation treatments.

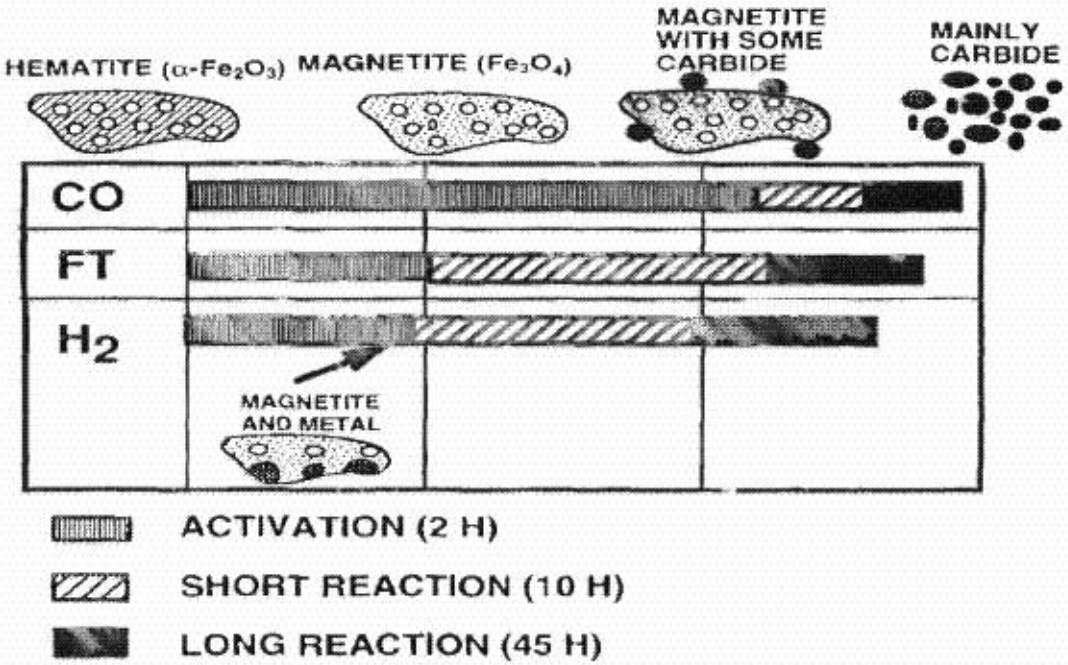


**Figure 1.14** Schematic representation of the differences in the extent of transformation caused by different activation treatments[16]

### 1.2.2.1 Effect of Activating Gas on Iron Phases Formed During Activation

With CO or syngas activation, iron carbide phases are formed. Among these, O-carbides (carbides with carbon atoms in octahedral interstices *i.e.* ε-$Fe_2C$, ε'-$Fe_{2.2}C$ and $Fe_xC$) and TP-carbides (carbides with carbon atoms in trigonal prismatic interstices *i.e.* χ-$Fe_{2.5}C$ and θ-$Fe_3C$) have been identified[20]. $H_2$ activation yields metallic iron ($Fe^0$) which then evolves into iron carbide species under Fischer-Tropsch synthesis.

The actual nature of the Fe phases then depends on the reactor conditions i.e. temperature, pressure, gas hourly space velocity and the feed gas composition ($H_2$/CO ratio). This is shown in work done by Bukur *et al*[21] where they determined the iron phases in pretreated and used Ruhrchemie catalysts by means of X-ray diffraction (XRD) after various pretreatment conditions with $H_2$, CO and syngas in a fixed bed reactor (see Table 1.3).

**Table 1.3** Iron phases in pretreated and used Ruhrchemie catalyst samples by XRD[21]

| Pretreatment Conditions | Pretreated Catalyst | Used Catalyst after FT Synthesis |
|---|---|---|
| $H_2$, 220°C, 1h<br>3550 $cm^3$/min | metallic Fe | Top: ε'-C, metallic Fe<br>Bottom: ε'-C, metallic Fe |
| $H_2$, 280°C, 1h<br>3160 $cm^3$/min | metallic Fe | Top: ε'-C<br>Bottom: ε'-C, metallic Fe |
| $H_2$, 280°C, 8h<br>125 $cm^3$/min | metallic Fe | Top: ε'-C<br>Bottom: ε'-C, metallic Fe |
| $H_2$, 280°C, 24h<br>125 $cm^3$/min | | Top: ε'-C<br>Bottom: ε'-C, metallic Fe |
| CO, 280°C, 12h<br>125 $cm^3$/min | χ-C, ε'-C | Average: metallic Fe |
| $H_2$/CO = 2, 310°C, 6h,<br>1200 $cm^3$/min | χ-C | Top: χ-C<br>Bottom: metallic Fe, χ-C |

The iron phases in the pretreated and used catalyst samples were assigned by matching the observed lattice spacing values to those published in literature[22]. The common carbides present were found to be χ-$Fe_5C_2$ (Hägg carbide) and ε'-$Fe_{2.2}C$.

Herranz *et al.* also subjected precipitated iron catalysts with varying amounts of Ce and Mn promoters to activation with CO, syngas ($H_2/CO$ = 2.0) or $H_2$ and determined the iron phases after activation and temperature programmed experiments using XRD[17]. The results are presented in Table1.4. From these results it could be seen that mainly cementite (θ-$Fe_3C$) was formed with CO activation and Hägg carbide (χ-$Fe_{2.5}C$) with syngas activation.

| Sample | Pretreatment | Phases after pretreatment | Phases after TPDe-Ar | Phases after TPSR-$H_2$ |
|---|---|---|---|---|
| 100Fe | 5% CO/Ar | $Fe^0$, $Fe_3O_4$ $\theta$-$Fe_3C$ | $Fe^0$; $\theta$-$Fe_3C$ | $Fe^0$ |
| | CO | $\theta$-$Fe_3C$ | | $Fe^0$ |
| | $H_2/CO$ | $\chi$-$Fe_{2.5}C$ | | $Fe^0$; $\theta$-$Fe_3C$ $Fe_3O_4$ (traces) |
| 95Fe5Ce | 5% CO/Ar | $Fe^0$, $Fe_3O_4$ $\theta$-$Fe_3C$ | $Fe^0$; $\theta$-$Fe_3C$ | $Fe^0$ |
| | CO | $\theta$-$Fe_3C$ | | $Fe^0$ |
| | $H_2/CO$ | $\chi$-$Fe_{2.5}C$ | | $Fe^0$; $\theta$-$Fe_3C$ $Fe_3O_4$ (traces) |
| 95Fe5Mn | 5% CO/Ar | $Fe^0$; $Fe_3O_4$ $\theta$-$Fe_3C$ | $Fe^0$; $\theta$-$Fe_3C$ | $Fe^0$; $\theta$-$Fe_3C$ |
| | CO | $\theta$-$Fe_3C$ | | $\theta$-$Fe_3C$ |
| | $H_2/CO$ | $\chi$-$Fe_{2.5}C$ | $Fe^0$ (traces) $\theta$-$Fe_3C$ | $\theta$-$Fe_3C$ |
| 70Fe30Mn | 5% CO/Ar | $Fe^0$; $Fe_3O_4$ FeO | $Fe^0$; FeO | $Fe^0$; $\theta$-$Fe_3C$ $Fe_xMn_{1-x}O$ |
| | CO | $\theta$-$Fe_3C$ $Fe_xMn_{1-x}O$ | | $\theta$-$Fe_3C$ $Fe_xMn_{1-x}O$ |
| | $H_2/CO$ | $\chi$-$Fe_{2.5}C$ $Fe_xMn_{1-x}O$ | $\theta$-$Fe_3C$ $Fe_xMn_{1-x}O$ | $\theta$-$Fe_3C$ $Fe_xMn_{1-x}O$ |

*Note*: $\chi$-$Fe_{2.5}C$: Hägg carbide; $\theta$-$Fe_3C$: cementite; $Fe^0$: metallic iron; $Fe_3O_4$: magnetite; $Fe_xMn_{1-x}O$: manganowustite

**Table 1.4** Phases detected by XRD after activation pretreatments and temperature programmed experiments for catalysts containing varying amounts Ce and Mn promoters[17]

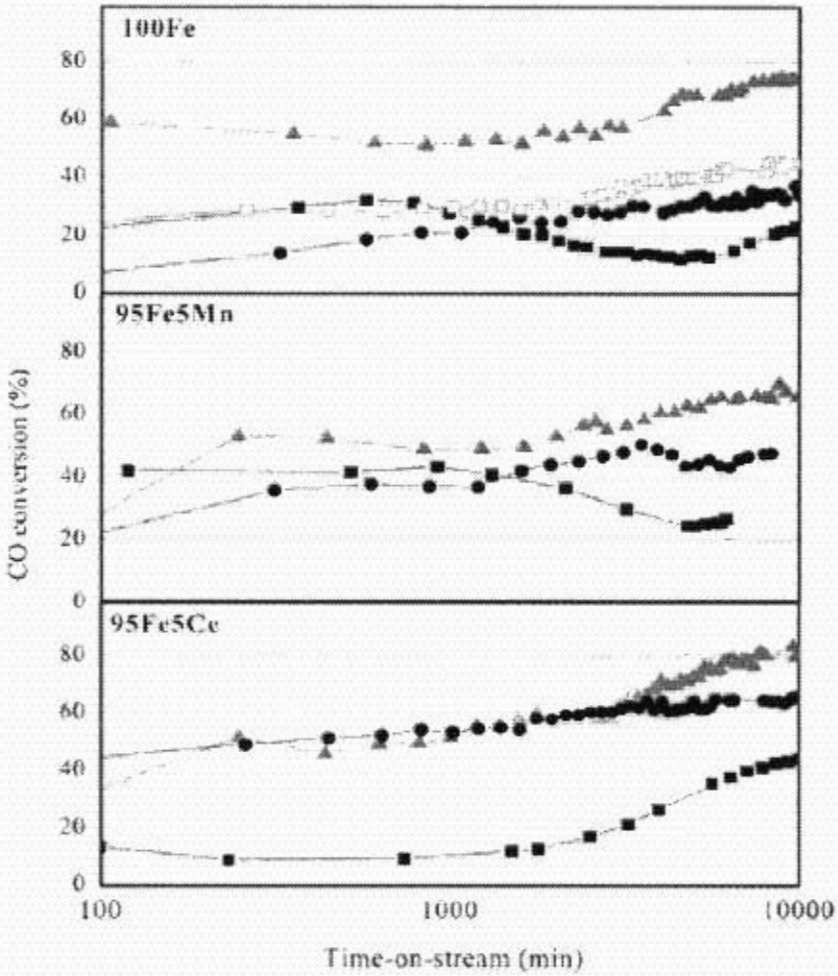


**Figure 1.15** CO conversion *vs.* time on stream after activation for different catalyst samples (activation: ■ = $H_2$, ▲ = syngas, ● = CO and □ = CO/Ar)[17]

Figure 1.15 shows the CO conversion versus time on stream for the different catalyst samples. Based on FTS results performed in a fixed bed micro-reactor and correlating the detected iron carbide phases with these results, it was concluded that the θ-$Fe_3C$ species was less active for FTS but that it can evolve into the more active χ-$Fe_{2.5}C$ species during reaction[17].

However Mansker *et al.* found in their work that the CO activated catalyst contained mainly monoclinic $Fe_{2.5}C$ along with some unreduced iron oxide[23]. Once FTS begins the $Fe_{2.5}C$ species then readily transforms into a mixture containing significant amounts of hexagonal $Fe_7C_3$ and trace amounts of

$Fe^0$. They then found that the catalyst appears to loose activity due to conversion of significant amounts of hexagonal $Fe_7C_3$ into monoclinic $Fe_{2.5}C$ and an accompanying growth in crystal size. They therefore concluded that in its most active form, the iron catalyst contains the $Fe_7C_3$ carbide. When monoclinic $Fe_{2.5}C$ was the predominant phase, the catalyst showed low activity.

The differences between the work done by Herranz *et al.* and Mansker *et al.* (and which could then possibly account for the difference in observations made) was that the activation and FTS was performed in a fixed bed micro-reactor as compared to a stirred tank reactor. Also, Mansker *et al.* analyzed the catalysts after activation and FTS by X-ray diffraction still coated in the waxy product, stating that the accuracy of the method is dependent on the concentration of the catalyst in the wax, the absorption characteristics of the various iron phases, the length of time over which the data is collected and the soundness of the iron phase crystal structure models employed. It is not mentioned in the Herranz work whether samples where characterized still coated in wax or whether the wax was removed by for example Soxhlet extraction; only that samples were passivated after activation and FTS.

Jung and Thomson have also suggested that for slurry-phase iron catalysts the active catalytic phase for FTS may be $\varepsilon'$-$Fe_{2.2}C$[24]. Over long periods $\varepsilon'$-$Fe_{2.2}C$ then converts to $\chi$-$Fe_{2.5}C$.

The above thus illustrates the debate which continues regarding the actual nature of the active iron phases for Fisher-Tropsch synthesis. Nonetheless, what is certain is that there is a correlation between carbide content and FT activity and that, with time-on-stream, catalysts appear to lose activity due to the conversion of a catalytically active carbide phase to a less active phase. However a change in carbide phase is not the only factor which can lead to

a loss in activity of a catalyst. What follows is a discussion on additional factors that will lead to a loss of activity of a FT catalyst.

### 1.3 Catalyst Deactivation

The loss of catalytic activity and/or selectivity is a source of concern for not only the Fischer-Tropsch process, but also many other industrial catalytic processes. Bartholomew reviewed the literature treating catalyst deactivation and mentions that although there are many intrinsic mechanisms of catalyst deactivation, they can be classified into six separate types *viz.* poisoning, fouling, thermal degradation, vapour compound formation accompanied by transport, vapour-solid and/or solid-solid reactions and attrition/crushing[11]. Figure 1.16 illustrates the different types of deactivation which could occur inside a catalyst particle.

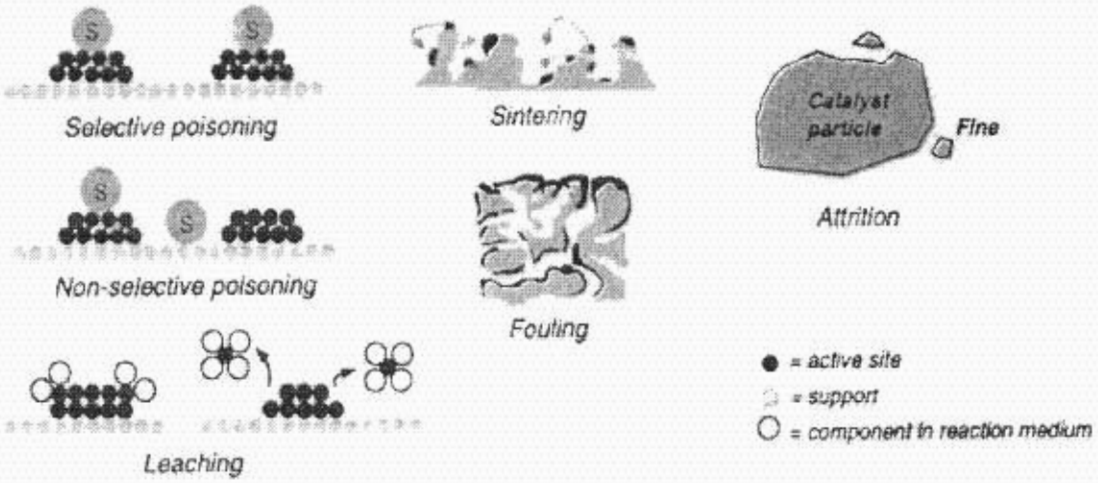


**Figure 1.16** Types of deactivation which could occur inside a catalyst particle[25]

However, Moulijn *et al.* mentions that the differing types of deactivation do not always occur in isolation, but that deactivation could also occur due to a combination of the above mentioned types[25]. The adsorption of sulphur on a platinum catalyst is given as an example. Here sulphur poisons the Pt sites

which, in turn, cause the Pt clusters to become more mobile leading to sintering. Bartholomew and Farrauto describe these combinations of deactivation mechanisms as either parallel or series deactivation mechanisms[26]. In parallel deactivation, the rate of deactivation depends on reactant concentrations and, in series deactivation, the rate depends on product concentration.

### 1.3.1 Deactivation due to Poisoning

Bartholomew defines poisoning as the strong chemisorption of reactants, products or impurities on sites that would otherwise be available for catalysis. This chemisorption can either be reversible or irreversible[25], but sometimes a clear distinction between temporary and permanent poisoning cannot be made since poisons that are strong poisons at low temperatures are less harmful in high temperature processes[11]. Catalyst poisons exist in various forms and can be classified by chemical makeup, selectivity for active sites and according to the types of reactions poisoned. Examples of catalyst poisons are given in Table 1.5. Common poisons can be classified according to chemical structure (Table 1.6).

**Table 1.5** Examples of catalyst poisons[11]

| Type of Poison | Examples |
|---|---|
| Strong Chemisorber | $H_2S$<br>$NH_3$ |
| Surface active metal or ion | Cu in Ni<br>Ni in Pt<br>Fe in Pt<br>Pb or Ca in $Co_3O_4$<br>Pb in $Fe_3O_4$ |
| High molecular weight product producer | Acetylenes<br>Dienes |

**Table 1.6** Poisons classified according to chemical structure[11]

| Chemical Type | Examples | Type of interaction with metals |
|---|---|---|
| Groups VA and VIA | N, P, As, Sb, O, S, Se, Te | Through s- and p-orbitals; shielded structures are less toxic |
| Group VIIA | F, Cl, Br, I | Through s- and p-orbitals; formation of volatile halides |
| Toxic heavy metals and ions | As, Pb, Hg, Bi, Sn, Zn, Cd, Cu, Fe | Occupy d-orbitals; may form alloys |
| Molecules which adsorb with multiple bonds | CO, NO, HCN, benzene, acetylene, other unsaturated hydrocarbons | Chemisorption through multiple bonds and back bonding |

The interaction of group VA-VIIIA elements with a catalyst depends on how many electron pairs are available for bonding and the degree of shielding. In the case of toxic heavy metals or compounds that are reducible to metals, reaction conditions may cause them to alloy with the active catalyst metal, thereby reducing the effectiveness of the latter. Examples are Cu in Ni and Fe in Pt.

Furthermore, poisons can be classified as selective, anti-selective or non-selective[11]. Selective poisons adsorb preferentially on the most active sites of the catalyst at low concentrations. If sites of lesser catalytic activity are initially blocked the poison is then classified as anti-selective. If activity loss is observed to be proportional to the concentration of the adsorbed poison, the poisoning is said to be non-selective. Figure 1.17 illustrates the different mechanisms of poisoning.

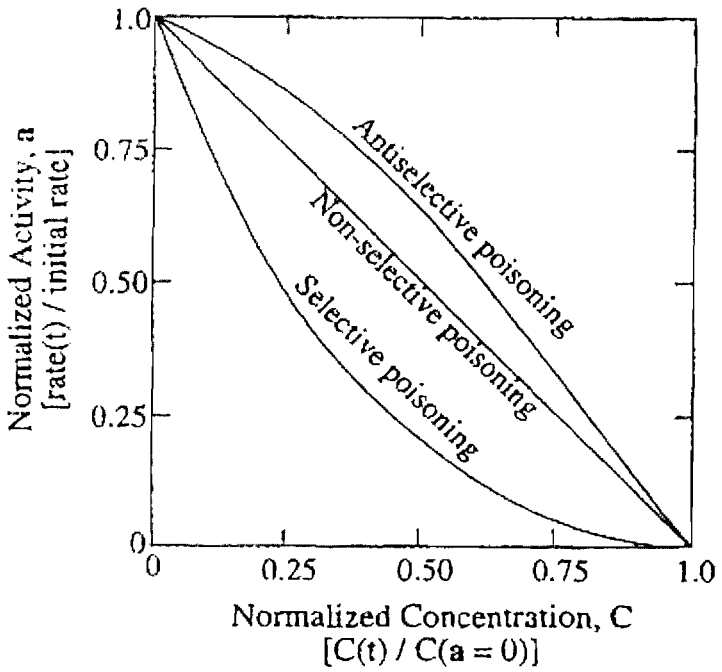


**Figure 1.17** Kinds of poisoning behaviour in terms of normalized activity *vs.* normalized poison concentration[11].

An example of selective poisoning is the deactivation of platinum by CO during *para*-$H_2$ conversion, while Pb poisoning of CO oxidation on Pt is anti-selective. Arsenic poisoning of cyclopropane hydrogenation on Pt is non-selective.

Figure 1.17 is based on the assumption of uniform poisoning of the catalyst surface with negligible pore diffusional resistance. This is however rarely the case in industrial processes because of high temperature and pressure which bring about a high pore diffusional resistance for either the main reaction or poisoning reaction or both. Thus poisoning may occur preferentially in the outer shell of the catalyst particle or the catalytic reaction may occur preferentially in the outer shell or both. For example, if the main reaction is limited to an outer shell in a pellet where poison is concentrated, the drop in activity with concentration will be sharp. Typical poisons affecting iron- and cobalt-based catalysts for Fischer-Tropsch

synthesis are $H_2S$ and COS (discussed in Section 1.1.1), As, $NH_3$ and metal carbonyls.

### 1.3.2 Deactivation due to Fouling

Fouling is defined as the covering of a catalytic surface by a deposit[11]. The origin of the deposit could be due to the formation of by-products because of the catalytic process or external factors such as the deposition of dust from combustion residues or mechanical wear of equipment. In the case where by-products lead to fouling, it could happen that due to the catalytic process, several reactions can occur that lead to coke or carbonaceous material.

The chemical structures of coke or carbon formed in catalytic processes vary according to reaction type, catalyst type and reaction conditions. For example, carbon can be a product of CO disproportionation as illustrated in Equation 1.3. Bukur *et al* found that reduction with hydrogen and CO decreased the BET surface area significantly, with the reduction in BET surface area being more pronounced when using CO[15]. This greater decrease in BET surface area when using CO was ascribed to the formation of carbonaceous deposits which blocked the pores of the catalyst thus resulting in a lower measured surface area. As such, deactivation due to the formation of carbon overlayers could be considered inherent to the Fischer-Tropsch process and is caused by CO dissociation leading to the formation of surface carbon[10].

$$CO_{(adsorbed)} \longrightarrow C_{\alpha(adsorbed)} + O_{(adsorbed)} \qquad (1.3)$$

Coke can be produced by decomposition or condensation of hydrocarbons on catalyst surfaces and typically consists of polymerized heavy hydrocarbons.

### 1.3.2.1 Carbon Formation

Carbons can have a number of different structures ranging from near amorphous to highly crystalline. Gas phase carbon (or soot) is produced in spherical particles formed by small crystallites which then tend to link together in chain-like structures. Surface carbons, on the other hand, have bigger crystallites, lower interlayer spacing and higher densities and form films deposited on solid subtrates. Ni, Co and Fe are highly effective substrates for carbon formation[25].

Carbon deposits can be characterized according to their appearance and microstructure into three categories *viz.* laminar graphite, non-orientated carbon and fibrous carbon[27].

Laminar graphite has a structure close to that of ideal graphite and can be obtained under conditions of relatively low hydrocarbon pressure and high substrate temperature.

Non-orientated carbons (also known as polycrystalline carbons) are formed by small crystallites lacking orientation with the substrate. They are produced under conditions that favour high supersaturation of carbon on metal. Laminar graphite is usually also present in the deposits, with the nature of these two forms being interchangeable.

Bartholomew identified various carbonaceous species having various degrees of reactivity on the surface of nickel catalysts after deposition from CO and hydrocarbons (Table 1.7)[11]. Similar species were identified on the surface of iron-based catalysts after the Fischer-Tropsch reaction[21].

**Table 1.7** Forms and reactivities of carbon species formed by decomposition of CO on nickel

| Structural Type | Designation | Temperature of formation (°C) | Peak temperature for reaction with $H_2$ |
|---|---|---|---|
| Adsorbed, atomic (surface carbide) | $C_\alpha$ | 200-400 | 200 |
| Polymeric, amorphous films or filaments | $C_\beta$ | 250-500 | 400 |
| Vermicular filaments, fibers and/or whiskers | $C_v$ | 300-1000 | 400-600 |
| Nickel carbide (bulk) | $C_\gamma$ | 150-250 | 275 |
| Graphitic (crystalline platelets or films) | $C_c$ | 500-550 | 550-850 |

Niemantsverdriet *et al.* proposed reaction pathways which compete for carbon deposition on the surface of an iron catalyst by dissociation of CO. The proposed pathways are given by Equations 1.4 - 1.6[28] and illustrated in Figure 1.18.

Carburization : $C^* + \text{iron} \rightarrow \text{carbide}$ (1.4)

Synthesis : $C^* + xH^* \rightarrow CH^*_x$ (1.5)

Deactivation : $C^* + yC^* \rightarrow \text{inactive carbon}$ (1.6)

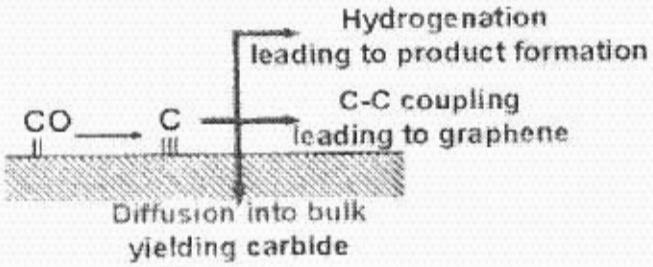


**Figure 1.18** Formation and consumption of surface carbon in the Fischer-Tropsch synthesis[10]

Under mild steady-state conditions Eliason and Bartholomew state that Equation 1.4 is not a serious competitor for carbon atoms[29]. As reaction temperatures however increase, it plays a significant role. Equations 1.7 and 1.8 show their proposed parallel model for loss of activity during CO hydrogenation on Fe at high temperature and is illustrated in Figure 1.19.

$$C^* + yC^* \rightarrow C^*_{y+1} \text{ (polymeric } \beta\text{-carbon)} \rightarrow [\ -C^*_{y+1}-]_n \text{ (graphitic } \delta\text{-carbon)} \quad (1.7)$$

$$\varepsilon'\text{-}Fe_{2.2}C \rightarrow \chi\text{-}Fe_{2.5}C \rightarrow \theta\text{-}Fe_3C \quad (1.8)$$

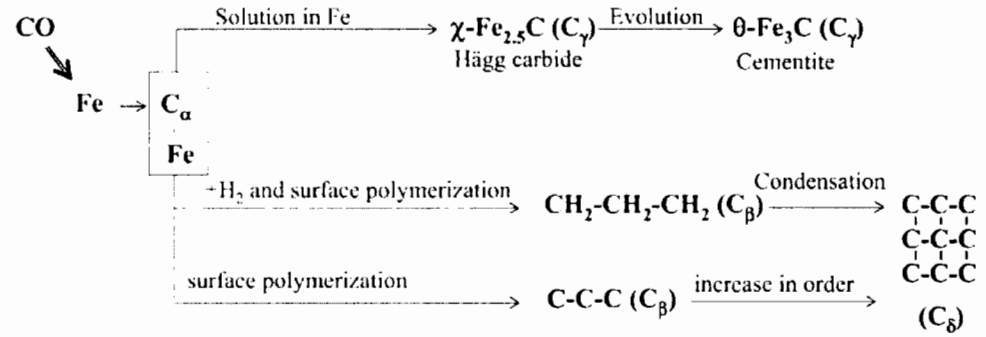


**Figure 1.19** Routes of formation of carbonaceous species[17]

Filamentous carbon growth (formation of the $C_\beta$ or $C_v$ species in Table 1.), which inhibits catalyst activity, occurs in parallel with carbide formation (Figure 1.20). Kock *et al.* determined that the carbon filaments grew by the continuous decomposition of metastable carbide intermediates[30]. These metastable carbide intermediates were proposed to be ε-$Fe_2C$ or ε'-$Fe_{2.2}C$. The driving force for filament growth is thought to be a gradient in the carbon content of nonstoichiometric carbides which decreases in the direction to the metal-carbon interface. The movement of carbon atoms causing the gradient is due to Gibbs free energy of the metal carbide which is thought to be higher than that of its constituent elements.

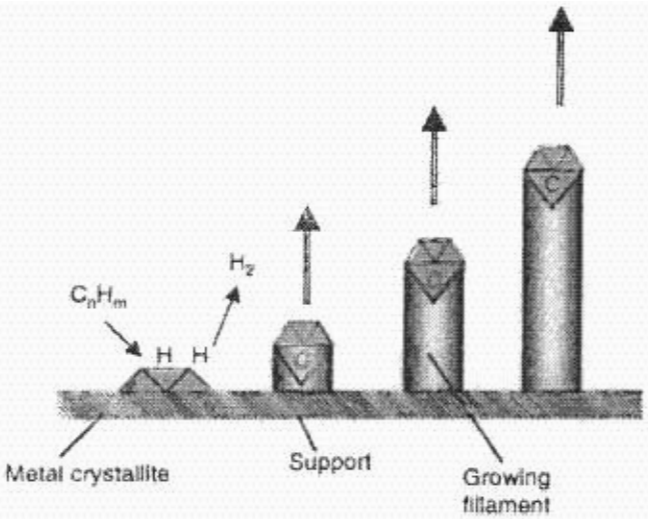


**Figure 1.20** Schematic of carbon filament formation on a supported metal catalyst[25]

Filamentous carbon growth occurs in the temperature range where most Fischer-Tropsch synthesis reactions are performed (LTFT and HTFT) and is the most detrimental form of carbon since, due to its high mechanical strength, continuous filamentous carbon growth can lead to the disintegration of the catalyst particle[31].

### 1.3.2.2 Coke Formation

In reactions involving hydrocarbons, coke may be formed in the gas phase and deposited on both non-catalytic and catalytic surfaces. Coke contains high boiling point polycyclic aromatic compounds which may contain heteroatoms and ordered or disordered carbon originating in the gas phase or on a surface[27].

The production of aromatics can be related to the concentration of olefins in a reactor. Figure 1.21 illustrates the formation of aromatics in terms of a Diels-Alder type of condensation reaction involving butadiene. This may be a simplistic manner in which to account for the total production of aromatics, but addition/polymerization reactions of this type can be expected to be involved in the formation of polycyclic aromatics. The order of reactivity for

coke formation is structure dependent and in the order polynuclear aromatics > aromatics > olefins > branched alkanes > normal alkanes[27].

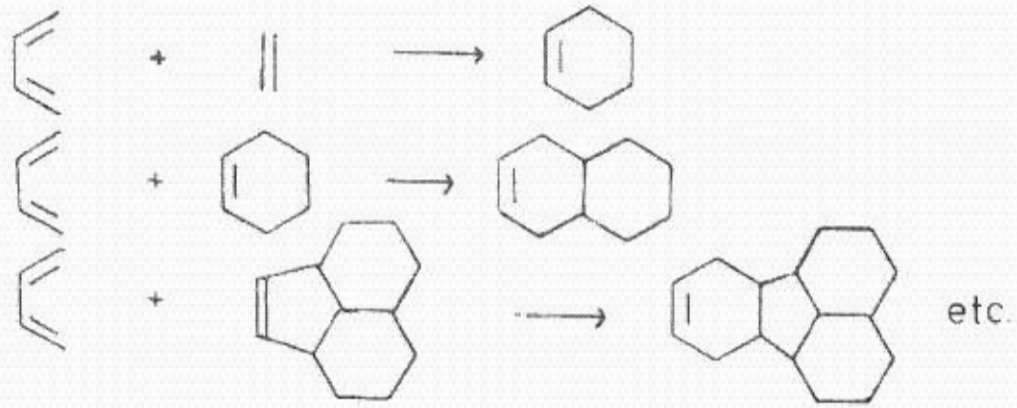


**Figure 1.21** Formation of aromatics by Diels-Alder type condensation reactions

### 1.3.3 Deactivation due to Sintering

Thermal degradation is a physical process leading to catalyst deactivation because of sintering, chemical transformations or evaporation. Sintering is the loss of catalyst active surface due to crystallite growth of either the support material or the active phase and is strongly temperature dependent[25]. Figure 1.22 illustrates the sintering phenomena.

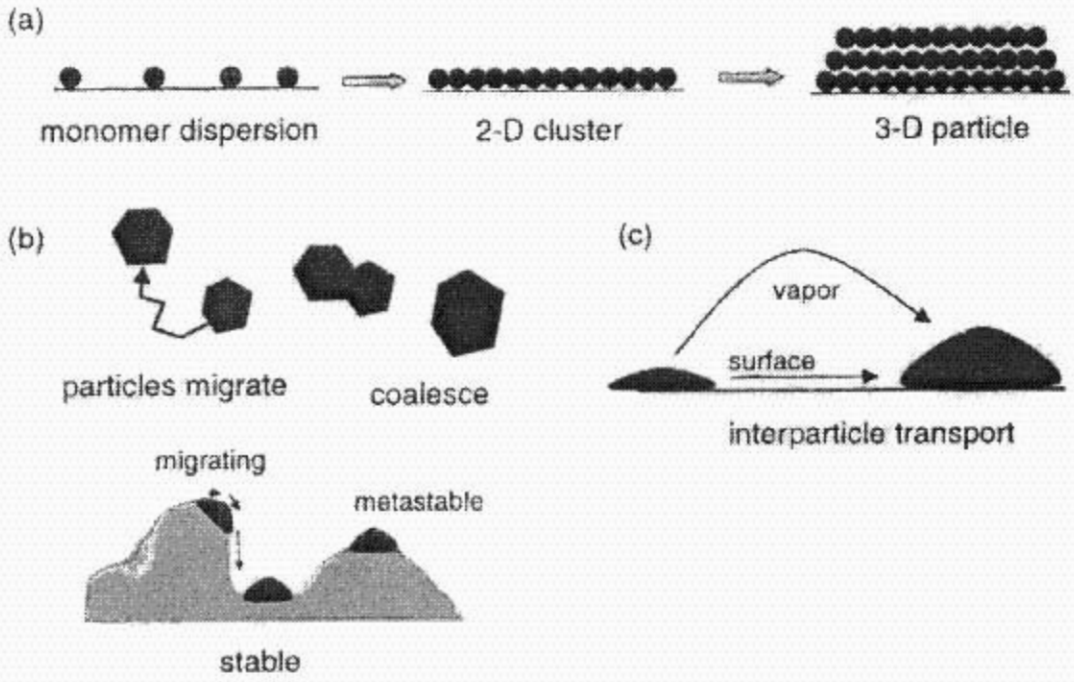


**Figure 1.22** Various stages in the formation and growth of particles from monomer dispersion[25]

The underlying mechanism for sintering is surface diffusion or at sufficiently high temperatures, mobility of larger aggregates[11]. However there exist three principal mechanisms of sintering *viz.* crystallite migration, atomic migration and vapour transport (at very high temperatures).

Crystallite migration involves the migration of entire crystallites over a support surface followed by coalescence. The most important mechanism for sintering of small particles is the movement of atoms rather than particles and involves the detachment of metal atoms from crystallites, migration of these atoms on a support surface and finally the capture by larger crystallites.

Parameters affecting rates of sintering and redispersion are temperature, atmosphere, metal type, metal dispersion, promoters/impurities and support surface area, texture and porosity. Sintering rates increase exponentially

with temperature. Also metals sinter relatively rapidly in oxygen and relatively slowly in hydrogen.

Sintering resembles crystallization *i.e.* larger particles grow at the expense of smaller ones. In addition, the position of a particle contributes to sintering. A "valley" position (see Figure 1.22(b)) is stable, while a particle positioned higher up is highly unstable[25].

### 1.3.4 Deactivation due to Mechanical Failure of Catalysts (e.g. attrition and crushing)

There are various forms and mechanisms of mechanical failure which can include crushing due to load, attrition leading to fines and erosion of catalyst particles. The formation of fines or erosion of catalyst particles can lead to the loss of catalytic material through for example the filtration system of a slurry bed reactor or the cyclones of a fluidized bed reactor. Hence mechanical failure due to attrition or collapse of agglomerates is a serious or limiting problem in many commercial catalytic processes[11].

Crushing can occur during transport and loading of the catalyst in a reactor. Attrition is evident by a reduction in the particle size or a rounding or smoothing of the catalyst particle which can be easily observed under an optical or electron microscope. Attrition occurs especially in fluid or slurry bed reactors.

The shape of a catalyst particle influences its mechanical strength; a spherical shape being the most favourable. Mechanical strength is also related to porosity where, for example, macropores will lead to reduced strength.

### 1.3.5 Deactivation due to vapour-solid and/or solid-solid reactions

Vapour-solid and/or solid-solid reactions are chemical routes leading to catalyst deactivation[11]. There can be reactions of the vapour phase with the catalyst surface to produce inactive bulk and surface phases or volatile compounds which exit the catalyst and reactor in the vapour phase. There can also be catalytic solid/support or catalytic solid/promoter reactions and solid-state transformations of the catalytic phases during reaction.

An example of a vapour-solid reaction is the oxidation of Fe carbide during the Fischer-Tropsch process. Here $Fe_5C_2$ can be transformed to $Fe_3O_4$ due to oxidation at high CO conversion by $H_2O$ and $CO_2$. Although the loss of activity could be linked to poisoning, the difference compared to poisoning is that activity loss is not due to adsorption of oxygen, but rather due to the formation of an altogether new phase.

Vapour-solid reactions can also produce volatile metal compounds like metal carbonyls. This leads to deactivation due to metal loss because of vapourization of volatile metal compounds.

Catalyst deactivation by solid-solid reactions is an important mechanism for degradation of complex multi-component catalysts in dehydrogenation, synthesis, partial oxidation and total oxidation reactions. These reactions are processes in which there is the formation of a new bulk phase due to diffusion or solid-state reaction. An example of this is the transformation of active carbides to inactive carbides during Fischer-Tropsch synthesis using a Fe/K/Cu catalyst.

### 1.3.6 Modeling Deactivation

In general the activity of a catalyst, $a(t)$, at time $t$ can be defined as the ratio of the rate of reaction on a catalyst that has been used for a time $t$, to the rate of reaction on a fresh catalyst[32]:

$$a(t) = \frac{-r'A(t)}{-r'A(t)(t = 0)} \tag{1.9}$$

Combining Equation 1.9 with the equation for the rate of disappearance of a reactant A on a catalyst that has been utilized for a time $t$ we get the reaction rate law accounting for catalyst activity:

$$-r'_A = a(t)k(T)f(C_A, C_B, \ldots, C_P) \tag{1.10}$$

where $a(t)$ = catalytic activity, time dependent
$k(T)$ = specific reaction rate, temperature dependent
$C_i$ = gas-phase concentration of reactants or products

The rate of catalyst decay, $r_d$, can be expressed in a rate law similar to Equation 1.10:

$$r_d = -da/dt = p[a(t)]k_d(T)h(C_A, C_B, \ldots, C_p) \tag{1.11}$$

where $k_d$ = specific decay constant
$h(C_i)$ = functionality of $r_d$ on the reacting species concentrations

$h(C_i)$ can be either independent of concentration ($h = 1$) or be a linear function of species concentration ($h = C_i$).

The activity term, $p[a(t)]$, can take a variety of forms. For a first-order decay, $p(a) = a$ and for a second-order decay $p(a) = a^2$ and will vary with the gas used and the mechanism of decay.

Various equations exist for the different types of deactivation mechanisms. For example, Table 1.7 gives the rate equation pairs for different types of deactivation[33, 26].

**Table 1.8** Rate equation pairs for different types of deactivation

| Deactivation Type[a] | Rate Equations |
|---|---|
| Parallel deactivation<br>$A \rightarrow R$<br>$A \rightarrow P\downarrow$ | $-dC_A/dt = k(C_A)^n a$<br>$-da/dt = k_d(C_A)^m a^d$ |
| Series deactivation<br>$A \rightarrow R \rightarrow P\downarrow$ | $-dC_A/dt = k(C_A)^n a$<br>$-da/dt = k_d(C_R)^m a^d$ |
| Impurity deactivation<br>$A \rightarrow R$<br>$P \rightarrow P\downarrow$ | $-dC_A/dt = k(C_A)^n a$<br>$-da/dt = k_d(C_P)^m a^d$ |
| Independent deactivation<br>(concentration independent)<br>$A \rightarrow R$ | $-dC_A/dt = k(C_A)^n a$<br>$-da/dt = k_d{}^m a^d$ |

[a]A, R, P refer to reactant, desired product and poison respectively

According to the stated hypothesis, activation and FTS with a CO rich gas will lead to deactivation due to carbon deposition. The amount of carbon on the surface of a catalyst after a time $t$ has been found to obey the empirical relationship

$$C_C = At^n \tag{1.12}$$

where $C_C$ = concentration of carbon on the surface
$A$, $n$ = fouling parameters

The expression was originally developed by Voorhies[34] and has been found to hold for a wide variety of catalysts and feedstreams. Different functionalities between the activity and amount of carbon on a catalyst have been observed. One commonly used form is

$$a(t) = 1/C_C{}^P + 1 \tag{1.13}$$

or, in terms of time, $$a(t) = 1/A^P t^{np} + 1 \tag{1.14}$$

For this project then it will be attempted to fit rate expressions such as Equation 1.14 to the slope of the tangent of the deactivation curve at various times $t$ of time-on-stream. If deactivation follows the same mechanism the parameters $A$ and $n$ (if Equation 1.14 is used) should have similar values at the various time periods where the rate expression is applied. Along with characterization data obtained we will then be able to prove or disprove the hypothesis of deactivation due to carbon deposition when using a CO rich gas during activation and synthesis.

### 1.4 Scope of Project

As previously discussed, iron catalysts need to form a number of chemical phases, including various iron oxides and iron carbides to be active for the Fischer-Tropsch synthesis. The final or most stable phase under Fischer-Tropsch synthesis conditions then determines the performance of the catalyst.

The gas used for the activation ($H_2$, CO or syngas) plays a major role in the catalyst composition and subsequent performance with reactor conditions contributing further in determining the actual nature and composition of the iron phases and carbide species. Literature suggests that utilizing CO would result in an activity that is much higher compared to when hydrogen or syngas is used[14, 15].

The reason for the lower activity shown by $H_2$ pretreated catalysts is because during activation the catalyst precursor transforms from hematite to magnetite and finally metallic iron. Metallic iron is prone to sintering at the temperatures employed in the activation studies discussed previously, but when a more moderate temperature was used during $H_2$ reduction, catalyst activities comparable to CO and syngas pretreatment were achieved.

With CO or syngas activation iron carbide phases are formed. Metallic iron is formed during $H_2$ activation which evolves into iron carbide species under Fischer-Tropsch synthesis. A correlation between carbide content and Fischer-Tropsch activity has been established although the actual nature of the active iron phases for the Fischer-Tropsch synthesis is largely debated. For example Herranz *et al.* suggests that the active phase is $\chi$-$Fe_{2.5}C$, whereas Mansker *et al.* present evidence for $Fe_7C_3$ being the active phase. Furthermore Jung and Thomson also suggested that for slurry-phase iron catalysts the active catalytic phase for FTS may be $\varepsilon$'-$Fe_{2.2}C$ which over long periods then transforms from $\varepsilon$'-$Fe_{2.2}C$ into $\chi$-$Fe_{2.5}C$.

Whatever the active carbide species though, it has also been noted that with time-on-stream, catalysts appear to loose activity due to the conversion of a catalytically active carbide phase to a less active phase. However a change in carbide phase cannot alone be ascribed to a loss in activity. There are also various other mechanisms responsible for catalyst deactivation as discussed previously and, with the exception of poisoning, these mechanisms can all be related to the activation and/or conditions prevalent during synthesis.

One of the deactivation mechanisms mentioned was fouling due to carbon deposition. Deactivation due to the formation of carbon overlayers can be considered inherent to the Fischer-Tropsch process and is caused by CO dissociation which leads to the formation of surface carbon.

Thus it can be hypothesized that although CO, according to literature, is a superior activating gas, it results in more rapid catalyst deactivation due to carbon deposition. Therefore, when using a CO rich gas as activating gas and during the Fischer-Tropsch synthesis, deactivation is due to the high CO content and not a change in iron phase. In this project therefore, the

effect of activation on the deactivation of a precipitated iron based catalyst will be studied.

To prove or disprove the above hypothesis, catalysts will be pretreated and subjected to the Fischer-Tropsch synthesis with syngas having varying $H_2$/CO ratios and compared by means of characterization of the untreated, activated and spent catalysts. Transmission Electron Microscopy (TEM) will be used in order to monitor carbon formation on the catalyst surface[35].

In order to prove or disprove that a change in the iron phase is not responsible for catalyst deactivation, X-ray Diffraction (XRD) and Mössbauer Absorption Spectroscopy (MAS) will be employed.

XRD can be used to identify bulk phases, monitor the kinetics of bulk transformations and in addition can also estimate particle sizes (thus also potentially providing information as to the degree that the sintering mechanism plays a role in the deactivation of the catalyst)[35].

To compliment the XRD analysis, MAS will also be used for the determination of phases, kinetics of bulk transformations, structural information and of oxidation states[35].

Also, to prove or disprove the above hypothesis, it will be attempted to fit the rate equations of deactivation due to carbon deposition to the activity data obtained during Fischer-Tropsch synthesis.

# 2 Experimental

## 2.1 Experimental Reactor System

The experimental system consisted of a gas delivery system, reactor system, hot and cold traps, back pressure regulator, on-line gas chromatograph for the analysis of the tail gas and vent system. The system flow scheme is shown in Figure 2.1. Table 2.1 gives the general parameters the system is operated at.

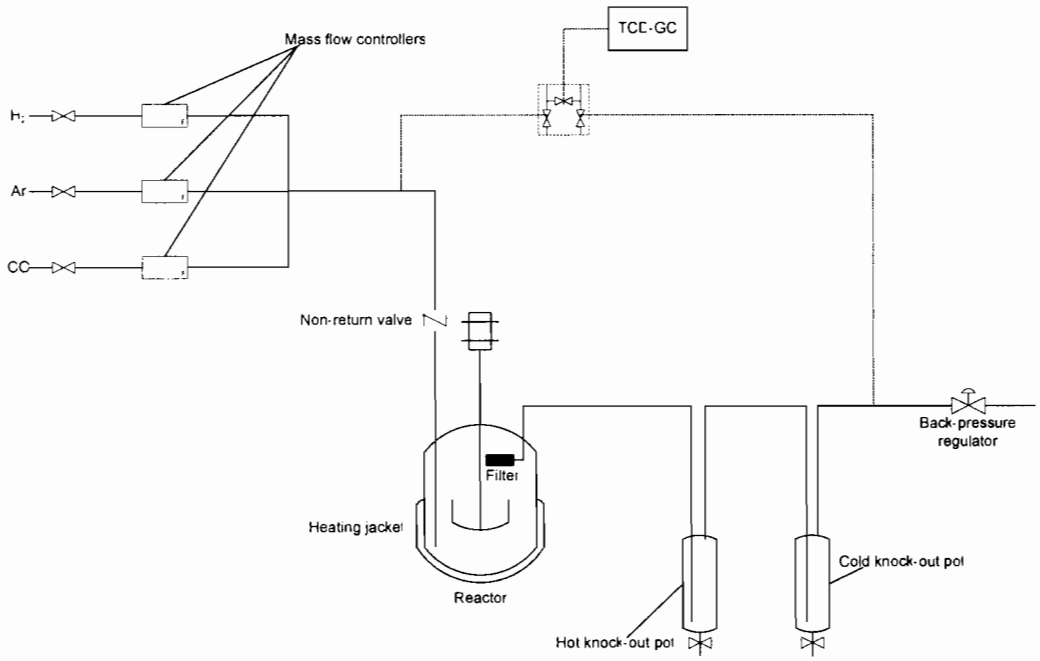


**Figure 2.1** Flow scheme of Micro-Slurry Reactor System

**Table 2.1** General operating parameters employed for CSTR

| | |
|---|---|
| Catalyst | Precipitated iron based Fischer-Tropsch catalyst, *ca.*10- 20 g |
| Slurry Medium | Sasolwax H1[a], *ca.* ¾ of reactor volume |
| Stirring Speed | *ca.* 300-500rpm |
| Synthesis Gas Hourly Space Velocity | *ca.* 6000-10000 ml/$g_{cat}$.h |
| System pressure | *ca.* 14 – 35 bar |
| Reactor Temperature | 230 – 260°C |
| Line, Hot Trap and Sample Point Temperatures | 200-220°C |

*a* = Commercial high molecular weight Fischer-Tropsch wax produced and sold by Sasol Chemical Industries Limited

### 2.1.1 Reactor Vessel

A continuously stirred tank reactor (CSTR) was used for activation and Fischer-Tropsch synthesis at syngas ratios of 1.0, 2.0 and in pure CO. The reactor unit is a 670 ml liquid volume (78 mm ID) flanged vessel with an approximate liquid volume hold-up of 500 ml under the experimental conditions employed. The vessel was designed and tested for maximum operating conditions of 300°C and 100 bar. The reactor vessel is heated by a removable electrical heating jacket that clamps tightly onto the vessel during use. The reactor set-up is shown in Figure 2.2.

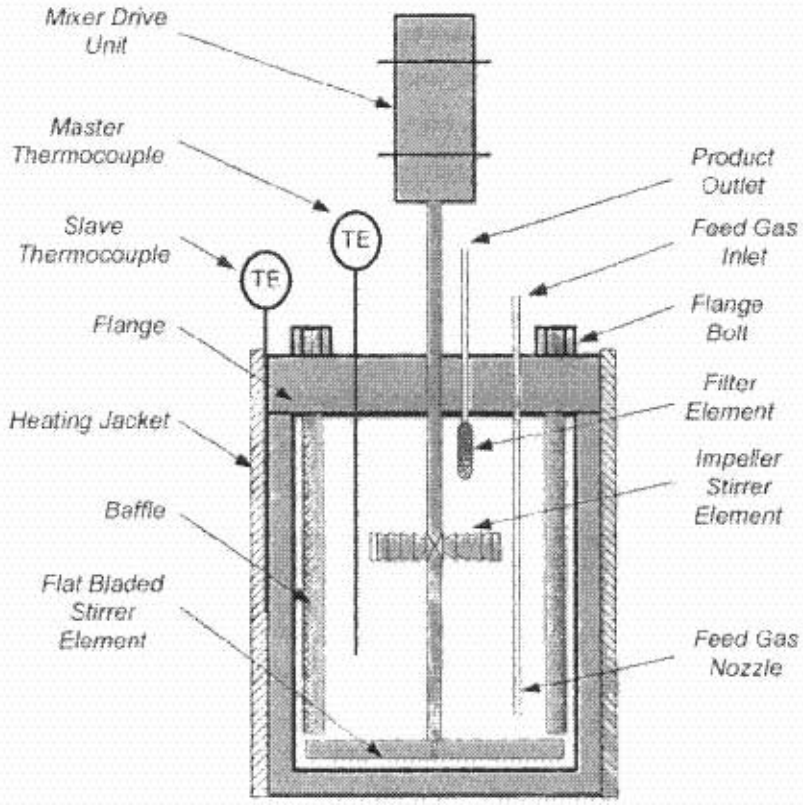


**Figure 2.2** Schematic of experimental reactor vessel and internals[36]

### 2.1.2 Temperature Control System

System temperature was controlled by five loops *viz.* reactor bomb temperature, temperature of product outlet line from reactor bomb to hot knock out pot, hot knock-out pot temperature, temperature of line from hot knock-out pot to cold knock-out pot and sample point and the reactor flange temperature.

Two temperature controllers control the heating of the reactor bomb contents and heating jacket. The reactor bomb operating temperature is controlled through a combination of the master and slave temperature controllers. The process value on the master heat controller indicates the temperature of the reactor bomb contents and maintains the desired temperature by controlling the heating jacket *via* the slave controller. The

process value on the slave controller indicates the temperature of the heating jacket.

The slave controller can be used in isolation, if it is set on "Local" mode control and will only control the heating jacket. This is done to "pre-heat" the reactor bomb when loading and melting the wax slurry medium prior to fastening the reactor bomb to its flange. The temperature of the heated lines, heavy product knock-out pot and sample point is controlled using an individual control loop and heating tape.

Each control loop is supplied with an ON/OFF power selector switch that controls the power to the heating elements. Each control loop is also supplied with a temperature trip to prevent uncontrolled heating leading to temperature run aways. The trip setting for the reactor bomb temperature is associated with the slave controller temperature. If a temperature trip is experienced, the power to the heating element is shut down.

### 2.1.3 Pressure Control System

A grove type backpressure regulator controlled the system pressure. Its set point was set manually by using argon. Two pressure indicators (PI) were available on the system, one on the reactor bomb itself as well as one to indicate the pressure of the tail gas after the knockout traps. A difference in pressure between the reactor and the tail gas PI indicated a possible blockage in the system. Blockages may cause over-pressure on the system. To this end, the reactor system was protected with relief valves (RV's) in case of over-pressure situations.

### 2.1.4 Gas Feed

Argon and hydrogen gases used in this study were sourced from AFROX as high purity cylinder gas. CO was obtained as cylinder gas from the SASOL n-butanol plant. Each feed gas cylinder is equipped with an in-line pressure regulator set to a maximum delivery pressure of *ca.* 50 bar.

Mass flow controllers (MFC) measure and control the flow of gasses to the reactor. Each MFC is rated for a specific gas based on its specific heat capacity ($C_p$). The mass flow controllers are therefore calibrated with the gas intended to be used with a specific mass flow controller. The MFC requires a 10 bar pressure differential ($\Delta P$) between the inlet and outlet in order to operate and is rated to work at certain pressures *e.g.* 30 bar inlet pressure and 20 bar outlet pressure. Care should be taken that a MFC is calibrated for a specific pressure range; *i.e.* a MFC calibrated for a 30 bar inlet pressure and 20 bar outlet pressure will not work if there is a 50 bar inlet pressure and 40 bar outlet pressure.

Moisture traps were installed to remove some of the entrained moisture from the gas supply stream. This is necessary since the presence of moisture is detrimental to the MFC. The traps are made of 75 ml Swagelock™ pressure vessels and packed with approximately 50 g of 3 Å molecular sieves. They were operated at room temperature. Between the moisture trap and MFC there was also a 15 µm online filter to remove any entrained solids.

### 2.1.5 Liquid Product Recovery

The reactor was fitted with two knock out vessels; one for heavy products *i.e.* wax (hot trap) and the other for the lighter products *i.e.* cold condensate and water (cold trap). The hot trap is 1 L in volume and operated at 210°C with a drain valve which is temperature rated. The cold trap is 2 L in volume and is operated at room temperature.

The mixed product stream from the reactor thus passes to the hot trap where the liquid carried from the product stream is separated from the vapour stream. The vapour stream then passes to the cold trap where the water and organic products are condensed out.

## 2.2 Experiments

For the runs done in this study the catalyst used was a precipitated iron catalyst similar to the Ruhrchemie precipitated iron catalyst[21].

### 2.2.1 Catalyst Loading

The reactor was charged with 350 g H1 wax. The wax was then melted at 150°C. Once all wax was molten, 20 g of the catalyst was added to the wax medium. The reactor was subsequently sealed and the stirrer (operating at 450 rpm) turned on to ensure uniform distribution of the catalyst through the wax medium. The temperature was then increased from 150°C to 230°C. The reactor was kept under an inert atmosphere of argon (flowing at approximately 200 $ml_{(N)}$/min) after sealing and during heating.

### 2.2.2 Activation and start-up of Fischer-Tropsch Synthesis

The catalyst was reduced *in situ* using synthesis gas or CO at 230°C and 12 bar for 36 h using a gas hourly space velocity (GHSV) of 6000 $ml/g_{cat}.h$. The hydrogen to carbon monoxide ratios in the synthesis gas used for the activation of the catalyst are given in Table 2.2. The synthesis gas ratios were varied in order to try and prove the stated hypothesis that deactivation can be correlated to the high CO content of the gas through enhanced carbon deposition during both activation and the Fischer-Tropsch synthesis. The synthesis gas ratios were thus varied between two extremes (2.0 and pure CO) and a ratio between these (1.0).

After the activation process, the knock-out pots were drained and the GHSV increased to 10 000 $ml/g_{cat}.h$. Temperature and pressure were increased to 240°C and 20 bar respectively, at which conditions the Fischer-Tropsch synthesis was performed. The space velocity was adjusted during synthesis to maintain a constant conversion of synthesis gas. It was aimed to maintain a $H_2$ + CO conversion of between 30 and 35%. Therefore the space velocity was adjusted if the $H_2$ + CO conversion dropped below *ca.* 30%

**Table 2.2** Overview of activation procedures employed ($T_{activation}$ = 230°C, $p_{activation}$ = 12 bar, GHSV during activation = 6000 $ml/g_{cat}.h$, activation time = 36 h)

| Experiment Number | Run Number | $H_2/CO$ Ratio during activation | $H_2/CO$ Ratio during Fischer-Tropsch Synthesis |
|---|---|---|---|
| 1(activation) | R074 | CO | - |
| 2 (activation) | R071 | 1.0 | - |
| 3 (activation) | R068 | 2.0 | - |
| 4 (activation) | D113 | $H_2$ | - |
| 5 (activation + FTS) | C046 | CO | 1.0 |
| 6 (activation + FTS) | R076 | 1.0 | 1.0 |
| 7 (activation + FTS) | R079 | CO | 2.0 |
| 8 (activation + FTS) | R073 | 2.0 | 2.0 |

### 2.2.3 Fresh Feed and Tail Gas Analysis

A gas chromatograph (GC) equipped with a thermal conductivity detector (TCD) was used to analyse for the permanent gases $H_2$, CO, $CO_2$, Ar, $CH_4$ and $N_2$. Figure 2.3 shows a typical TCD analysis of the GC calibration gas.

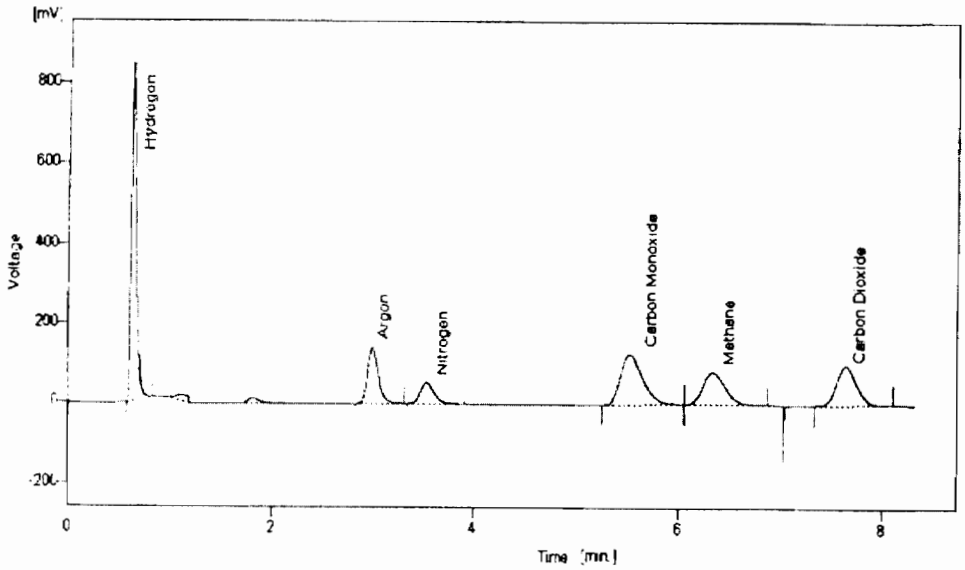


**Figure 2.3** TCD analysis of the GC calibration gas[36]

### 2.2.3.1 Data Evaluation

#### 2.2.3.1.1 Calculation of flow rates of various compounds from gas chromatographic analysis[37]

Flow rate of the various compounds are based on argon which is co-fed at a known flow rate. Argon is used as an internal reference and is typically co-fed at *ca.* 10 mol% of the total feed stream to the reactor. The flow rates of the other components of the feed gas (*e.g.* CO and $H_2$) are calculated using the peak areas obtained in the GC analysis with TCD (Equation 2.1)

$$F_j = f_j \cdot \frac{A_j}{A_{Ar}} \cdot F_{Ar} \qquad (2.1)$$

where $F_j$ = flow rate of compound j

$F_{Ar}$ = flow rate of argon

$f_j$ = compound specific calibration factor

$A_j$ = peak area of compound j in GC trace

$A_{Ar}$ = peak area of argon in GC trace

### 2.2.3.2 Calculation of conversion and rate of reaction

The conversion of component i is calculated from the flow rate of that component in the tail gas (TG) using the fresh feed flow rate (FF) minus the tail gas flow rate.

$$X_i = \frac{F_{i,FF} - F_{i,TG}}{F_{i,FF}} \qquad (2.2)$$

The usage ratio, U, of $H_2$ to CO is defined as the amount of $H_2$ consumed relative to the amount of CO consumed (Equation 2.3).

$$U = \frac{F_{H_2,FF} - F_{H_2,TG}}{F_{CO,FF} - F_{CO,TG}} \qquad (2.3)$$

The activity can be calculated from the amount of CO consumed minus the amount of $CO_2$ formed (Equation 2.4, where $m_{catalyst}$ is the mass of the unreduced catalyst).

$$r_{FT} = \frac{(F_{CO,\,feed} + F_{CO_2,\,feed}) - (F_{CO,\,tail} + F_{CO_2,\,tail})}{m_{catalyst}} \qquad (2.4)$$

The basic assumption underlying the above equation is that there is no (significant) carbon deposition taking place.

### 2.2.4 Unloading of Slurry

The slurry obtained for characterization after activation and Fischer-Tropsch synthesis was unloaded as follows:

a) When stopping the reaction, the reactor was cooled down to 200°C while keeping gas flow constant (same as under which the reaction was done);

b) Once 200°C was reached argon flow was increased to maximum;

c) After argon flow was fully opened hydrogen flow was decreased by 150 ml/min and CO flow by 100 ml/min;

d) The above step was repeated until the hydrogen and CO was completely closed;

e) Pressure in the reactor was then reduced to atmospheric pressure;

f) The reactor was then cooled to 150°C while stirring at reduced speed (150rpm) under argon in order to remove all synthesis gas from the wax;

g) After 150°C was reached, stirring was stopped and the reactor opened halfway to remove all the internals from the wax while still having argon flowing through the system until the wax solidified.

## 2.3 Catalyst Characterization

Catalyst samples were analysed using Mössbauer Absorption spectroscopy (MAS) and powder X-Ray Diffraction (XRD) to verify their phase compositions. Transmission Electron Microscopy was used to observe carbon deposition in the various activated and spent catalyst samples.

Activated as well spent catalyst samples for MAS were submitted without any pre-treatment *i.e.* coated in wax. Samples for XRD and TEM were washed 2 – 3 with warm (~70°C) cyclohexane and filtered before analysis.

### 2.3.1 Mössbauer Absorption Spectroscopy

The MAS experiments were performed using constant acceleration spectrometer equipped with $^{57}$Co/Rh sources. The data were recorded at room temperature typically over a velocity range of ± 12 mm/s. The spectra were analyzed by means of a least squares program "Normos" that models them as a combination of quadrupole doublets and sextets based on a Lorentzian line-shape profile. The individual absorption features were then identified on the basis of their isomer shift (δ), quadrupole splitting (Δ) and magnetic hyperfine field ($B_{hf}$) values. The relative amount of each phase was determined from the area of the absorption peaks. Metallic iron (α-Fe) was used to calibrate the velocity scale of MAS and the isomeric shift values of all the species were reported relative to it.

### 2.3.2 X-Ray Diffraction

The wax encapsulated sample was packed in a stainless steel cup sample holder and then placed in an Anton Paar XRK600 chamber coupled to a Panalytical X'Pert Pro multi-purpose diffractometer (XRD-1). A diffractogram was acquired before heating and thereafter at 100 °C, 110 °C, 120 °C and 140 °C, using a heating rate of 1 °C/min. The samples were heated under an inert atmosphere (using Ar at a flow rate of 50 $ml_N$/min). Phase

identification was done using X'Pert HighScore Plus software. The instrument settings were as follows:

| | | |
|---|---|---|
| Tube voltage | : | 40 kV |
| Tube current | : | 50 mA |
| Source | : | Cobalt (wavelength 1.78897 Å) |
| Soller slit | : | 0.04 rad. |
| Beam mask | : | 10 mm |
| Fixed divergence slit | : | 1° |
| Anti-scatter slit | : | 2° |
| Filter | : | Iron |
| Detector | : | X'Celerator |
| Detector active length | : | 2.121° |
| Scan from | : | $2\theta = 5°$ |
| Scan to | : | $2\theta = 105°$ |
| Scan axis | : | Gonio |
| Scan mode | : | Continuous |
| Step size | : | $2\theta = 0.0167°$ |

### 2.3.3 Transmission Electron Microscopy

TEM specimens were prepared by suspending the catalyst samples in methanol and then pipetting a small amount of this suspension on to a holey carbon coated copper grid. The grid was left for about 2 min in order to allow the methanol to evaporate before insertion of the sample into the instrument.

A Philips CM200 TEM operating at 200kV and fitted with a Gatan Image Filter was used to observe carbon deposition in the various activated and spent catalyst samples. Images were taken digitally using a Peltier-cooled Tietz (TVIPS) 2k x 2k CCD camera mounted below the viewing chamber.

# 3 Results

## 3.1 Activation and Fischer-Tropsch Synthesis

### 3.1.1 Catalyst Activation

It should be noted that the activation of the catalyst with synthesis gas (having ratios of either 1.0 or 2.0) leads to some Fischer-Tropsch activity. However, because the activation was performed at a rather low temperature of 230°C, the Fischer-Tropsch activity is expected to be rather low.

The activity, as defined in Chapter 2.2.3.2, is given below (Equation 2.4) and describes the above mentioned Fischer-Tropsch activity, *i.e.*, it describes the conversion of CO into hydrocarbons, $H_2O$ and $CO_2$ (which is produced by Equation 1.2 and not, to any considerable extent, by Equation 3.2).

$$r_{FT} = \frac{(F_{CO,\,feed} + F_{CO_2,\,feed}) - (F_{CO,\,tail} + F_{CO_2,\,tail})}{m_{catalyst}} \qquad (2.4)$$

$$nCO + 2nH_2 \rightarrow (-CH_2-)_n + nH_2O \qquad (1.1)$$

$$CO + H_2O \rightarrow H_2 + CO_2 \qquad (1.2)$$

$$2CO + H_2 \rightarrow (-CH_2-) + CO_2 \qquad (3.1)$$

$$2CO \rightarrow CO_2 + C \qquad (3.2)$$

However, when activating with CO gas, no Fischer-Tropsch activity can occur with only the deposition of carbon being possible along with the accompanying formation of $CO_2$ (Equation 3.2). In view of this therefore, the observed activity during activation is described as the rate at which a certain number of moles of CO is converted resulting in a net production of Fischer-

Tropsch products and $CO_2$ in the case of synthesis gas activation, or the net production of carbon and $CO_2$ in the case of CO activation. If one is to consider the difference in the amount of CO in the fresh feed and tail gas, the rate at which the number of moles of CO converted to hydrocarbon products, $CO_2$ and carbon and can be described by Equation 3.3.

$$r_{CO\ converted} = \frac{F_{CO,\ feed} - F_{CO,\ tail}}{22.4 \times m_{catalyst}} \qquad (3.3)$$

Thus when activating the catalyst with CO (Figure 3.1) a rate of 0.71 μmol CO converted/$g_{cat}$/s was recorded after 36 hrs of activation. Here the rate of CO conversion during activation can be directly linked to carbon deposition according to Equation 3.2.

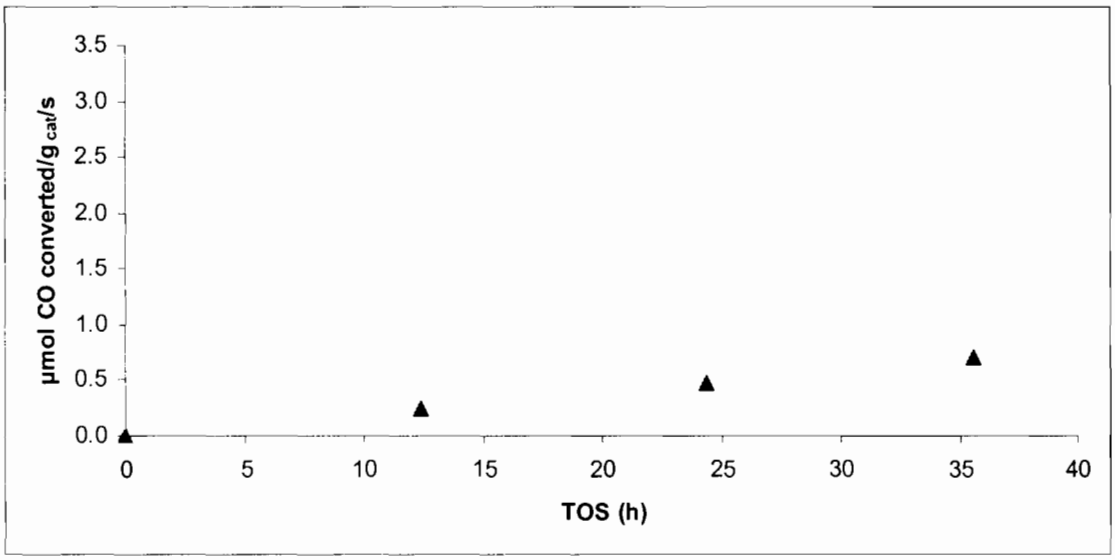


**Figure 3.1** Activity during activation with CO (Run R074: $T_{activation}$ =230°C, $P_{activation}$ = 12 bar; GHSV = 6000 $ml_n/g_{cat}/hr$)

The rate of CO transformation into Fischer-Tropsch products and $CO_2$ during activation with synthesis gas as a function of time is shown in Figure 3.2 and Figure 3.3. In general it was observed that the rate of CO conversion increased with increasing activation time, which might be ascribed to the formation of the active phase during the activation process. The rate of CO conversion after 36 h of activation with an $H_2/CO$ ratio of 1.0 was observed to be lower than the rate after the same time period using an $H_2/CO$ ratio of 2.0. The CO conversion rates for the three different activation procedures are summarized in Table 3.1.

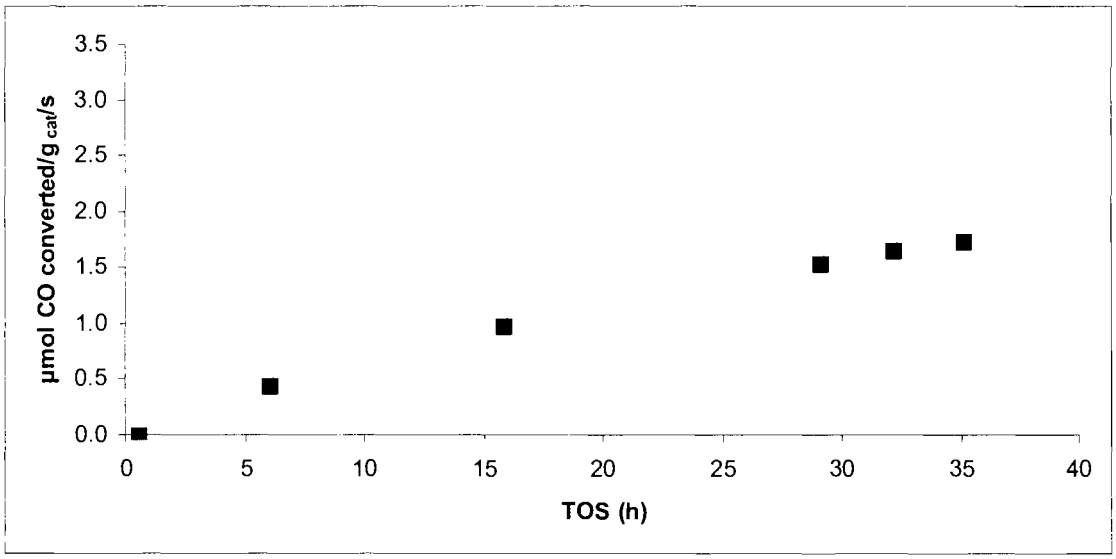


**Figure 3.2** Activity during activation with $H_2/CO$ ratio of 1.0 (Run R071: $T_{activation}$ =230°C, $P_{activation}$ = 12 bar; GHSV = 6000 $ml_n/g_{cat}/hr$)

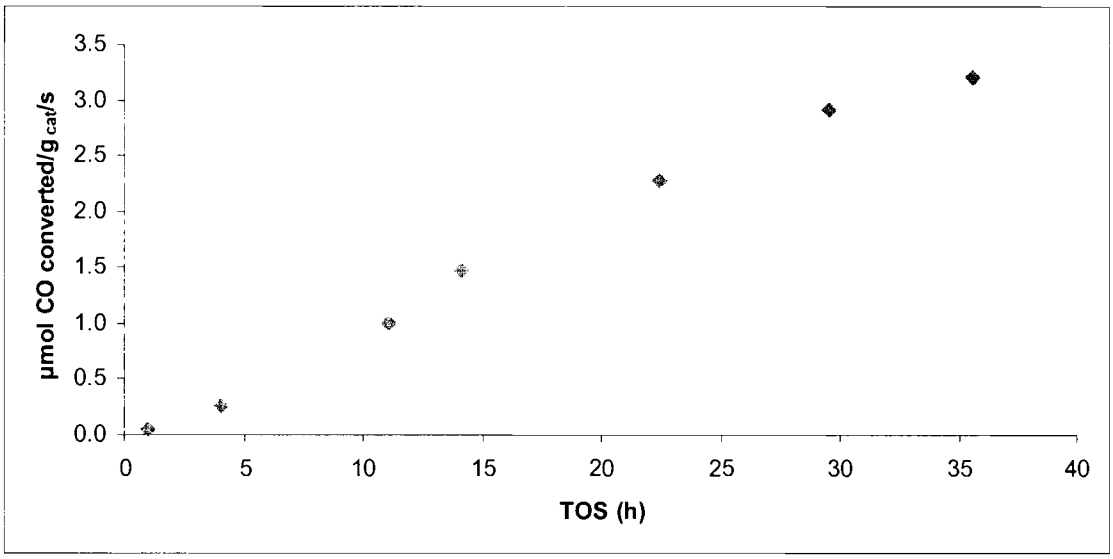


**Figure 3.3** Activity during activation with $H_2/CO$ ratio of 2.0 (Run R068: $T_{activation}$ =230°C, $P_{activation}$ = 12 bar; GHSV = 6000 $ml_n/g_{cat}/hr$)

**Table 3.1** Summary of maximum CO conversion rates reached after each activation procedure

| Run Number | $H_2/CO$ Ratio during activation | Maximum CO conversion rate achieved (µmol CO converted/$g_{cat}$/s) |
|---|---|---|
| R074 | CO | 0.71 |
| R071 | 1.0 | 1.97 |
| R068 | 2.0 | 3.21 |

### 3.1.2 Fischer-Tropsch Synthesis

After the catalysts were activated using either pure CO or synthesis gas having $H_2$/CO ratios of 1.0 or 2.0, they were subjected to the Fischer-Tropsch synthesis at 240°C with synthesis gas having $H_2$/CO ratios of either 1.0 or 2.0 for approximately 200 h.

The activity of the catalyst when using CO as activating gas and followed by the Fischer-Tropsch synthesis with synthesis gas having an $H_2$/CO ratio of 1.0 is shown in Figure 3.4 (dashed line indicates end of activation). A maximum activity of 7.55 µmol CO converted/$g_{cat}$/s was achieved during the Fischer-Tropsch synthesis; the activity during the Fischer-Tropsch synthesis defined as in Equation 2.4. A decline in catalytic activity was observed after *ca.* 100 h time on stream.

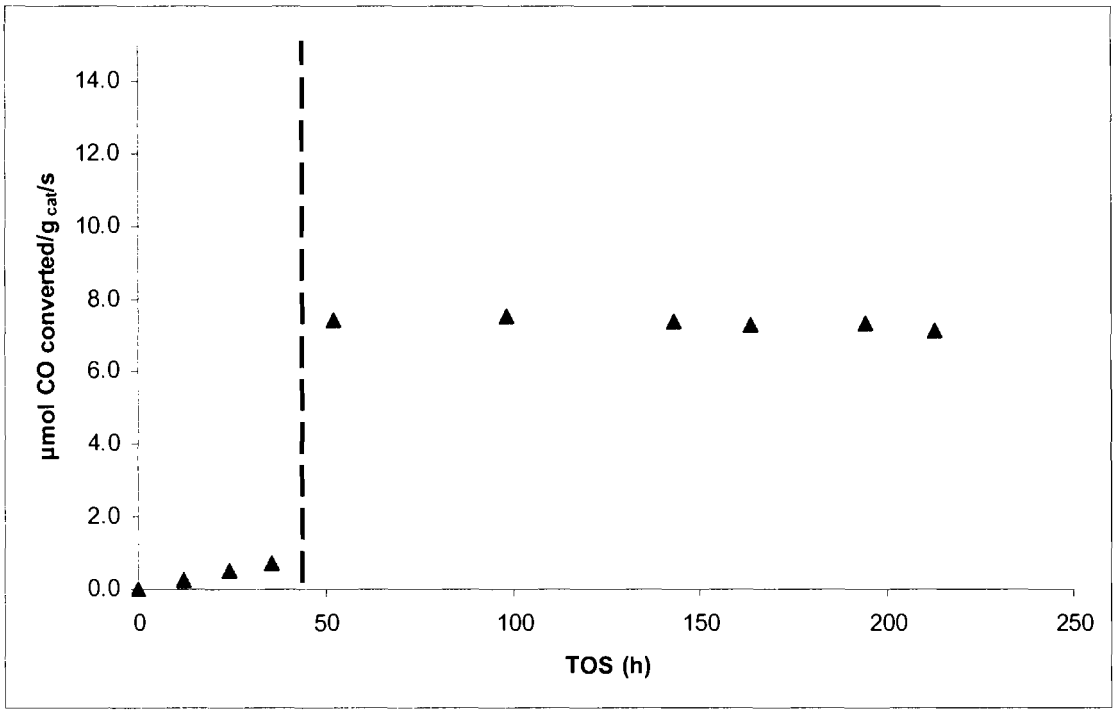


**Figure 3.4** Catalyst activity using CO as activating gas and followed by FTS with syngas having an $H_2$/CO ratio of 1.0 (Run C046: $T_{activation}$ =230°C, $P_{activation}$ = 12 bar; GHSV = 6000 $ml_n/g_{cat}$/hr, activation = 36 hrs; $T_{Fischer\text{-}Tropsch}$ =240°C, $P_{Fischer\text{-}Tropsch}$ = 20 bar, GHSV = 10000 $ml_n/g_{cat}$/hr)

The activity of the catalyst when using syngas with an $H_2$/CO ratio of 1.0 during both activation and the Fischer-Tropsch synthesis is shown in Figure 3.5 (run R076). A maximum activity of 7.67 µmol CO converted/$_{g.cat}$/s was achieved during the Fischer-Tropsch synthesis. The catalyst started deactivating after *ca.* 80 h time on stream.

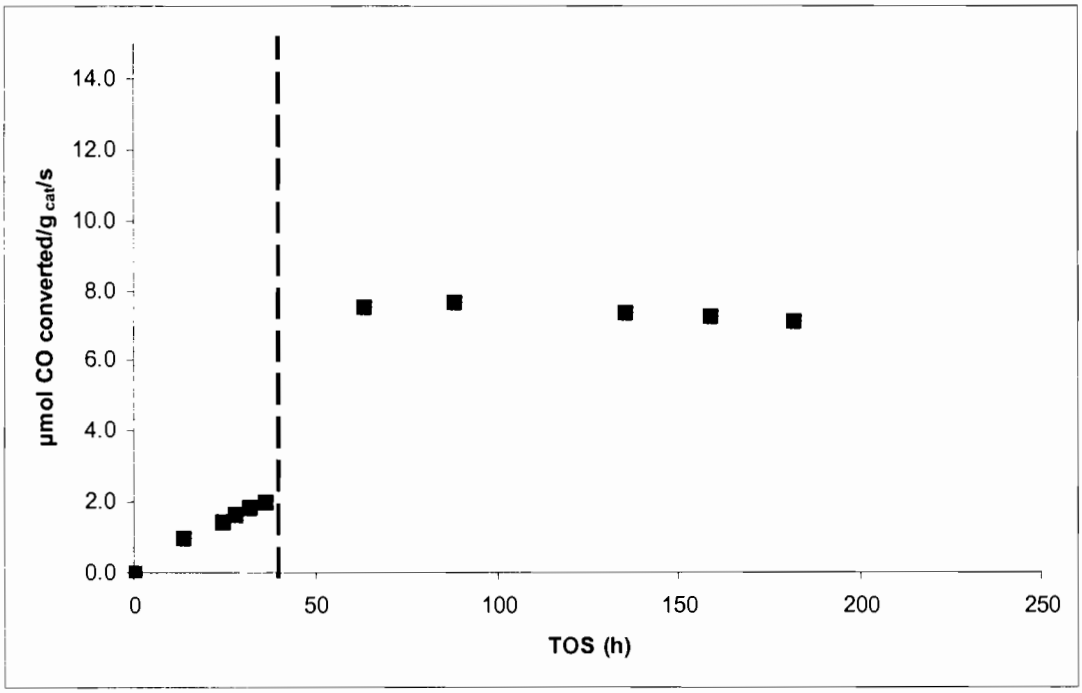


**Figure 3.5** Catalyst activity when using syngas with an $H_2$/CO ratio of during both activation and FTS (Run R076: $T_{activation}$ =230°C, $P_{activation}$ = 12 bar; GHSV = 6000 $ml_n/g_{cat}$/hr, activation = 36 hrs; $T_{Fischer\text{-}Tropsch}$ =240°C, $P_{Fischer\text{-}Tropsch}$ = 20 bar, GHSV = 10000 $ml_n/g_{cat}$/hr)

The activity of the catalyst when using CO as activating gas and followed by the Fischer-Tropsch synthesis with synthesis gas having an $H_2$/CO ratio of 2.0 is shown in Figure 3.6 (run R079). A maximum activity of 11.8 µmol CO converted/$_{g.cat}$/s was achieved during the Fischer-Tropsch synthesis. A decline in the catalyst activity was observed after *ca.* 164 h.

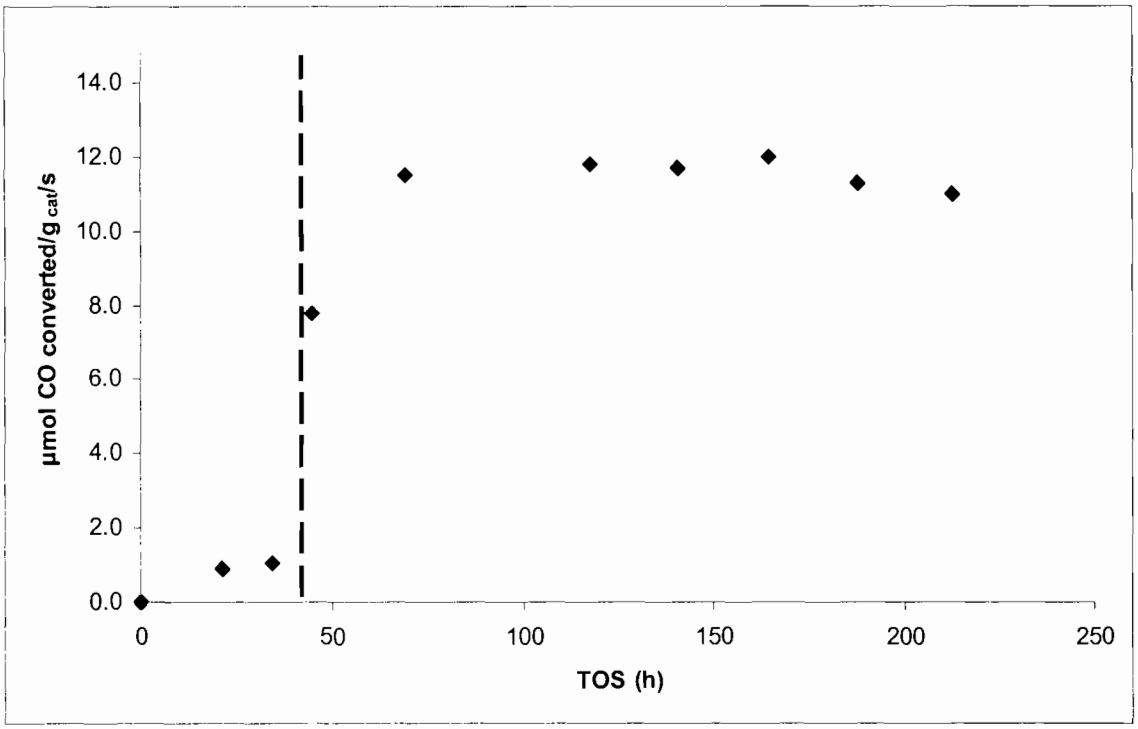


**Figure 3.6** Catalyst activity using CO as activating gas and followed by FTS with syngas having an $H_2/CO$ ratio of 2.0 (Run R079: $T_{activation}$ =230°C, $P_{activation}$ = 12 bar; GHSV = 6000 $ml_n/g_{cat}/hr$, activation = 36 hrs; $T_{Fischer\text{-}Tropsch}$ =240°C, $P_{Fischer\text{-}Tropsch}$ = 20 bar, GHSV = 10000 $ml_n/g_{cat}/hr$)

The activity of the catalyst when using syngas with an $H_2/CO$ ratio of 2.0 during both activation and FTS is shown in Figure 3.7 (run R073). A maximum activity of 9.94 µmol CO converted/$_{g.cat}$/s was achieved during the Fischer-Tropsch synthesis. Similarly to run R079, a decline in the catalyst activity was observed after *ca.* 163 h time on stream. The above results are summarized in Table 3.2.

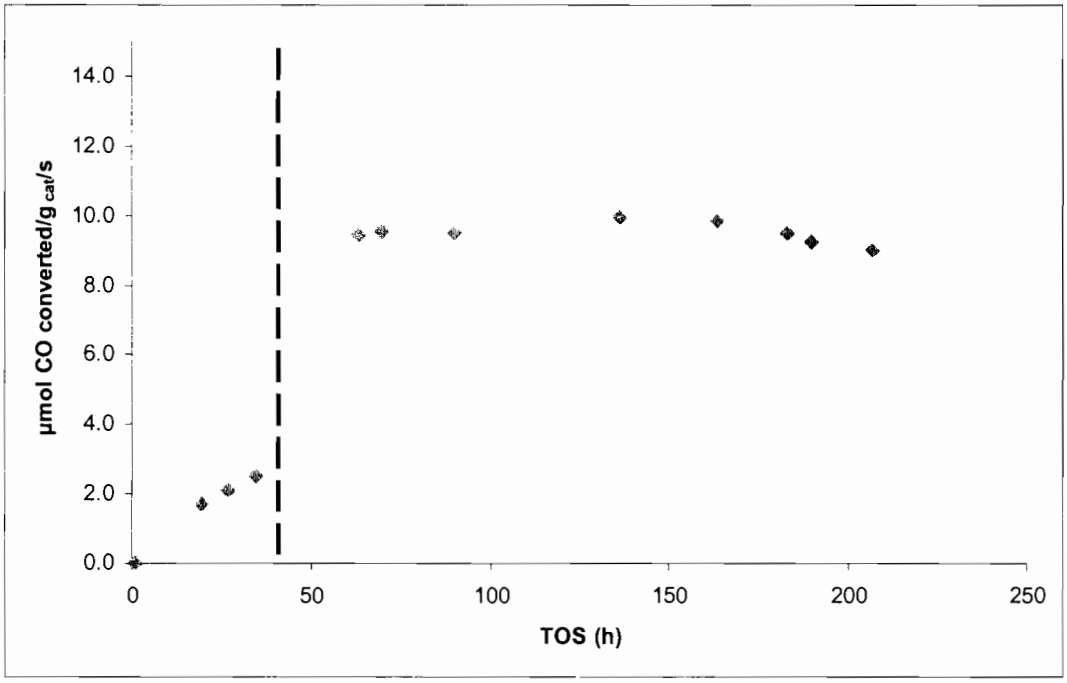


**Figure 3.7** Catalyst activity when using syngas with an $H_2/CO$ ratio of 2.0 during both activation and the Fischer-Tropsch synthesis (Run R073: $T_{activation}$ =230°C, $P_{activation}$ = 12 bar; GHSV = 6000 $ml_n/g_{cat}/hr$, activation = 36 hrs; $T_{Fischer\text{-}Tropsch}$ =240°C, $P_{Fischer\text{-}Tropsch}$ = 20 bar, GHSV = 10000 $ml_n/g_{cat}/hr$)

**Table 3.2** Summary of maximum activities reached during the Fischer-Tropsch synthesis after the different activation procedures

| Run Number | $H_2/CO$ Ratio during activation | $H_2/CO$ Ratio during Fischer-Tropsch Synthesis | Maximum Fischer-Tropsch Activity Achieved (µmol CO converted/$g_{cat}$/s) |
|---|---|---|---|
| C046 | CO | 1.0 | 7.55 |
| R076 | 1.0 | 1.0 | 7.67 |
| R079 | CO | 2.0 | 11.8 |
| R073 | 2.0 | 2.0 | 9.94 |

## 3.2 Characterization of Activated and Spent Catalysts

Activated and spent catalysts were characterized by means of room temperature Mössbauer Absorption Spectroscopy (MAS), X-ray Diffraction (XRD) and Transmission Electron Microscopy (TEM). Due to equipment availability, not all samples were analyzed with each technique. Table 3.3 indicates which characterization techniques each sample was subjected to.

**Table 3.3** Table indicating the characterization techniques each sample was subjected to

| Experiment Number | Run Number | $H_2$/CO Ratio during activation | $H_2$/CO Ratio during Fischer-Tropsch Synthesis | Characterization |
|---|---|---|---|---|
| 1(activation) | R074 | CO | - | MAS, XRD, TEM |
| 2 (activation) | R071 | 1.0 | - | MAS |
| 3 (activation) | R068 | 2.0 | - | MAS, XRD, TEM |
| 4 (activation) | D113 | $H_2$ | - | MAS, XRD, TEM |
| 5 (activation + FTS) | C046 | CO | 1.0 | MAS, XRD, TEM |
| 6 (activation + FTS) | R076 | 1.0 | 1.0 | - |
| 7 (activation + FTS) | R079 | CO | 2.0 | - |
| 8 (activation + FTS) | R073 | 2.0 | 2.0 | MAS, XRD, TEM |

### 3.2.1 Mössbauer Absorption Spectroscopy (MAS)

**Table 3.**Table 3.4 summarizes the hyperfine parameters of the calcined catalyst after various conditions of activation and the Fischer-Tropsch synthesis.

**Table 3.4** Hyperfine parameters of the calcined catalyst studied under different activation and synthesis conditions

| Sample | δ ($mms^{-1}$) | $E_Q$($mms^{-1}$) | $B_{hf}$ (T) | Iron phase | % Relative Area |
|---|---|---|---|---|---|
| Fresh SBR | 0.37 | 0.70 | - | $Fe^{3+}$ | 100 |
| | 0.37 | 1.21 | | | |
| R074 CO activation | 0.36 | 0.69 | - | $Fe^{3+}$ | 72.3 |
| | 0.39 | 1.04 | - | | |
| | 0.91 | 2.21 | - | $Fe^{2+}$ | 10.0 |
| | 0.32 | 0.08 | 22.0 | $\chi$-$Fe_5C_2$ | 17.7 |
| R071 Activation $H_2/CO$=1.0 | 0.37 | 0.71 | - | $Fe^{3+}$ | 82.6 |
| | 0.39 | 1.22 | - | | |
| | 0.90 | 2.14 | - | $Fe^{2+}$ | 8.7 |
| | 0.29 | 0.08 | 22.0 | $\chi$-$Fe_5C_2$ | 8.7 |
| | 0.20 | 0.11 | 17.9 | | |
| | 0.30 | 0.22 | 11.5 | | |
| R068 Activation $H_2/CO$=2.0 | 0.36 | 0.68 | - | $Fe^{3+}$ | 91.9 |
| | 0.37 | 1.15 | - | | |
| | 0.91 | 2.27 | - | $Fe^{2+}$ | 8.1 |
| D113 $H_2$ activation | 0.37 | 0.71 | - | $Fe^{3+}$ | 69.3 |
| | 0.36 | 1.17 | - | | |
| | 0.92 | 1.85 | - | $Fe^{2+}$ | 14.3 |
| | 0.00 | -0.01 | 33.3 | α-Fe | 16.4 |
| C046 CO activation + FTS $H_2/CO$ = 1.0 | 0.40 | 0.69 | - | $Fe^{3+}$ | 38.9 |
| | 0.41 | 1.08 | - | | |
| | 0.90 | 2.10 | - | $Fe^{2+}$ | 12.3 |
| | 0.30 | -0.02 | 22.4 | $\chi$-$Fe_5C_2$ | 39.8 |
| | 0.20 | 0.05 | 18.1 | | |
| | 0.30 | 0.22 | 11.0 | | |
| | 0.28 | 0.01 | 49.1 | $Fe_3O_4$ | 9.0 |
| | 0.67 | -0.10 | 45.6 | | |
| R073 Activation + FTS $H_2/CO$=2.0 | 0.40 | 0.68 | - | $Fe^{3+}$ | 41.2 |
| | 0.40 | 1.01 | - | | |
| | 0.90 | 2.10 | - | $Fe^{2+}$ | 15.5 |
| | 0.31 | -0.02 | 22.0 | $\chi$-$Fe_5C_2$ | 43.3 |
| | 0.20 | 0.05 | 17.9 | | |
| | 0.29 | 0.21 | 11.5 | | |

δ = isomer shift
$\Delta E_Q$ = electric quadrupole splitting
$B_{hf}$ = magnetic hyperfine splitting (Tesla units, T)

In order to track changes in catalyst composition under different activation as well Fischer-Tropsch synthesis conditions, it was essential to start with the data of a freshly calcined catalyst (Figure 3.8). The spectrum of the calcined catalyst was fitted with two quadrupole doublets with parameters, $\delta$ = 0.31 $mms^{-1}$, $\Delta E_Q$ = 0.58 $mms^{-1}$ for the first doublet and $\delta$ = 0.31 $mms^{-1}$, $\Delta E_Q$ = 1.14 $mms^{-1}$ for the second doublet. The parameters for both doublets were consistent with those of a $Fe^{3+}$ species and in this case they matched those of ferrihydrite ($Fe_5HO_8.4H_2O$).

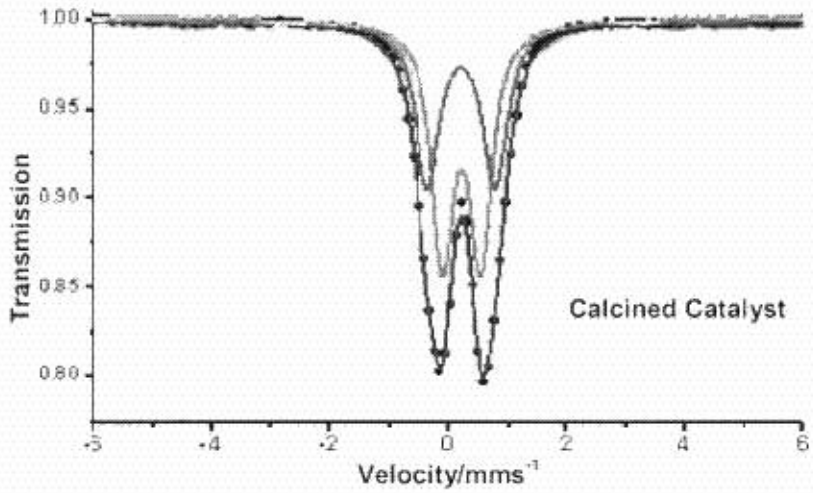


**Figure 3.8** Room temperature MAS spectra of the calcined catalyst

The MAS spectrum of the CO activated catalyst (R074) is shown in Figure 3.9. The spectrum exhibits three quadrupole doublets and three sextets. Two of the quadrupole doublets were due to a $Fe^{3+}$ species contributing about 72% of the total iron bearing components and the other doublet was due to a $Fe^{2+}$ species contributing approximately 10% of total iron content. The three sextets were assigned to Hägg carbide ($\chi$-$Fe_5C_2$) and contributed about 18% of the total iron bearing components.

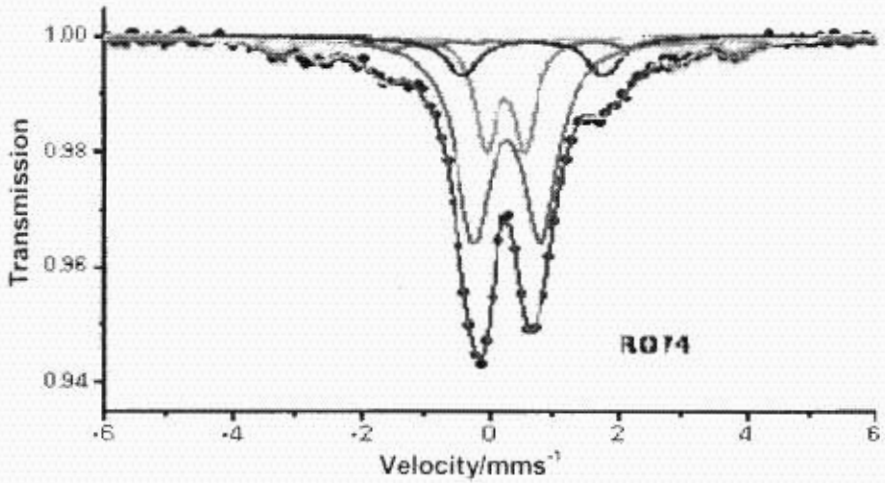


**Figure 3.9** Room temperature MAS spectra of the catalyst activated with CO

When the catalyst was activated using syngas with an $H_2/CO$ of 1.0 (R071), the MAS spectrum exhibited three sextets as well as three quadrupole doublets (Figure 3.10). Two of the quadrupole doublets with parameters $\delta$ = 0.37 $mms^{-1}$, $\Delta E_Q$ = 0.71 $mms^{-1}$ and $\delta$ = 0.39 $mms^{-1}$, $\Delta E_Q$ = 1.22 $mms^{-1}$ were consistent with those of a $Fe^{3+}$ species contributing about 83% of the total iron bearing components. The third doublet with parameters $\delta$ = 0.90 $mms^{-1}$, $\Delta E_Q$ = 2.14 $mms^{-1}$ was due to a $Fe^{2+}$ species contributing about 9% of the total iron content. The three sextets with parameters $\delta$ = 0.29 mm/s, $\Delta$ = 0.08 mm/s, $B_{hf}$ = 22.0 T; $\delta$ = 0.20 mm/s, $\Delta$ = 0.11 mm/s, $B_{hf}$ = 17.9 T and $\delta$ = 0.30 mm/s, $\Delta$ = 0.22 mm/s, $B_{hf}$ = 11.5 T, were assigned to $\chi$-$Fe_5C_2$ contributing about 9% of the total iron bearing components.

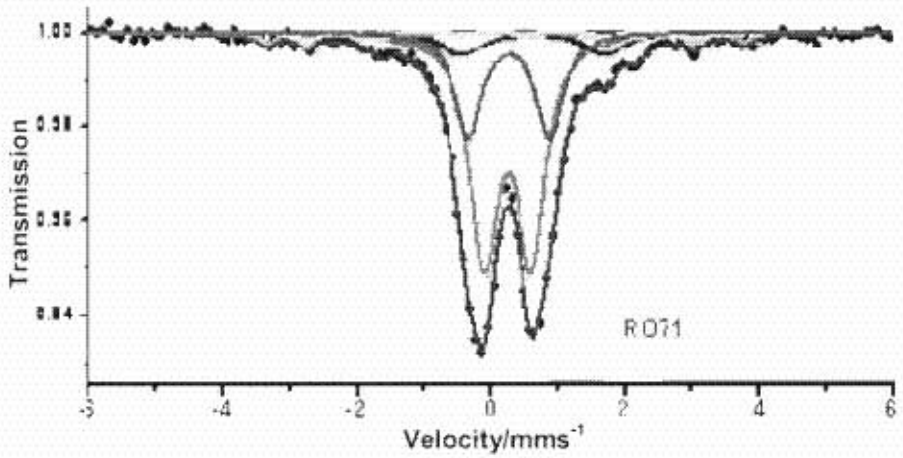


**Figure 3.10** Room temperature MAS spectra of the catalyst activated with syngas having an $H_2/CO$ ratio of 1.0

The MAS spectrum of the catalyst activated using a syngas $H_2/CO$ of 2.0 (R068) is shown in Figure 3.11. It was fitted with three quadrupole doublets, two of which had parameters, $\delta$ = 0.36 $mms^{-1}$, $\Delta E_Q$ = 0.68 $mms^{-1}$ and $\delta$ = 0.37 $mms^{-1}$, $\Delta E_Q$ = 1.15 $mms^{-1}$, and were due to a $Fe^{3+}$ species contributing about 92% of the total iron bearing components. The third quadrupole doublet with parameters, $\delta$ = 0.91 $mms^{-1}$, $\Delta E_Q$ = 2.14 $mms^{-1}$, was due to a $Fe^{2+}$ species contributing about 8%.

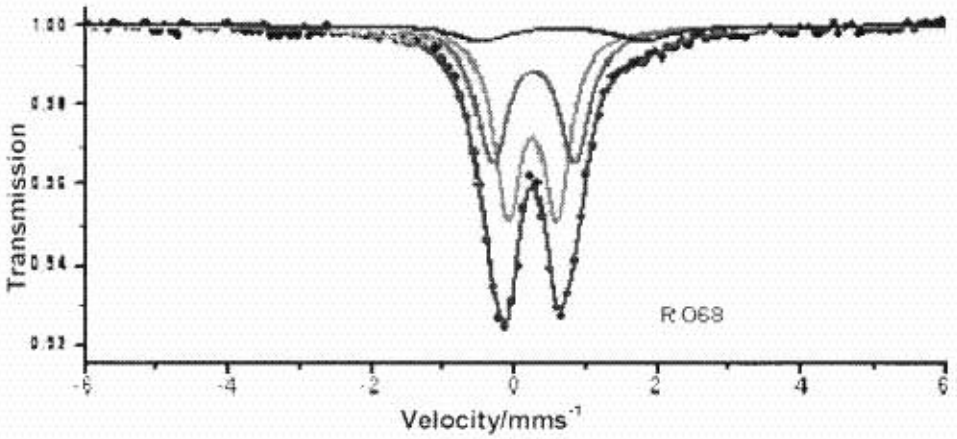


**Figure 3.11** Room temperature MAS spectra of the catalyst activated with syngas having an $H_2/CO$ ratio of 2.0

The MAS spectrum of the catalyst activated using hydrogen gas (D113) is shown in Figure 3.12. The spectrum is fitted with a set of three quadrupole doublets and a sextet. Two of the doublets with parameters, $\delta$ = 0.37 $mms^{-1}$, $\Delta E_Q$ = 0.71 $mms^{-1}$, for the first doublet and $\delta$ = 0.36 $mms^{-1}$, $\Delta E_Q$ = 1.17 $mms^{-1}$, for the second doublet, were due to a $Fe^{3+}$ species contributing about 71% of the total iron contribution. These doublets have similar parameters to those reported for the ferrihydrite phase of the calcined catalyst and are most likely to be due to this phase. The remaining doublet with parameters, $\delta$ = 0.92 $mms^{-1}$ and $\Delta E_Q$ = 1.85 $mms^{-1}$, was due to a $Fe^{2+}$ species contributing about 14% of the total iron content. The sextet was fitted with parameters, $\delta$ = 0.00 $mms^{-1}$, $\Delta E_Q$ = -0.01 $mms^{-1}$, $B_{hf}$ = 33.3 T, and was consistent with metallic iron (α-Fe) that contributed about 16% of the iron content.

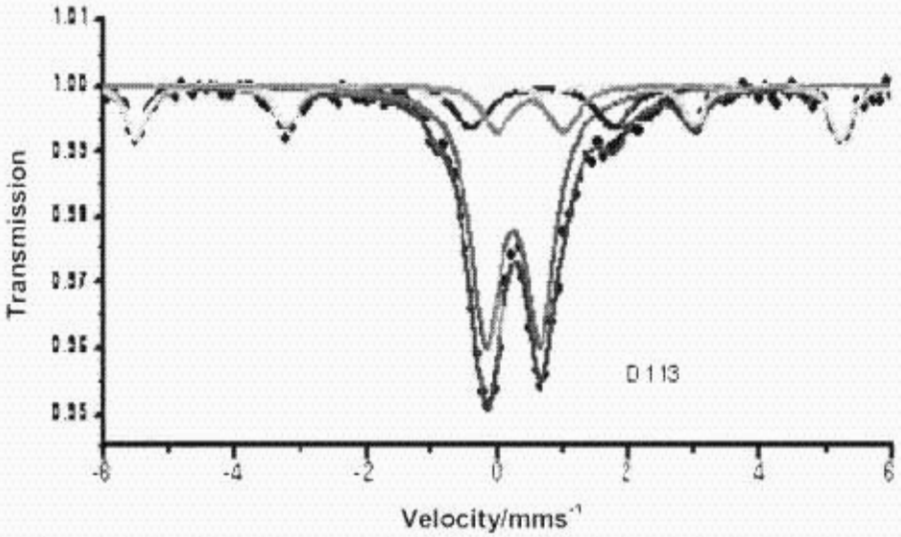


**Figure 3.12** Room temperature MAS of $H_2$ activated sample

The spectrum of the catalyst sample that had been activated with CO and subjected to the Fischer-Tropsch synthesis with a syngas $H_2$/CO ratio of 1.0 (C046) is shown in Figure 3.13. It exhibits three quadrupole doublets in conjunction with five sextets. Two of the quadrupole doublets were due to a $Fe^{3+}$ species that gave a combined iron contribution of about 39%. The third doublet was assigned to a $Fe^{2+}$ species contributing approximately 12% to the total iron content. The three sextets were assigned to $\chi$-$Fe_5C_2$ and gave an overall iron content contribution of about 40%. The remaining two sextets with parameters, $\delta$ = 0.28 mm/s, $\Delta E_Q$ = 0.01 mm/s, $B_{hf}$ = 49.1 T and $\delta$ = 0.67 mm/s, $\Delta E_Q$ = -0.10 mm/s, $B_{hf}$ = 45.6 T, were assigned to magnetite ($Fe_3O_4$) and gave an overall iron content contribution of about 9%.

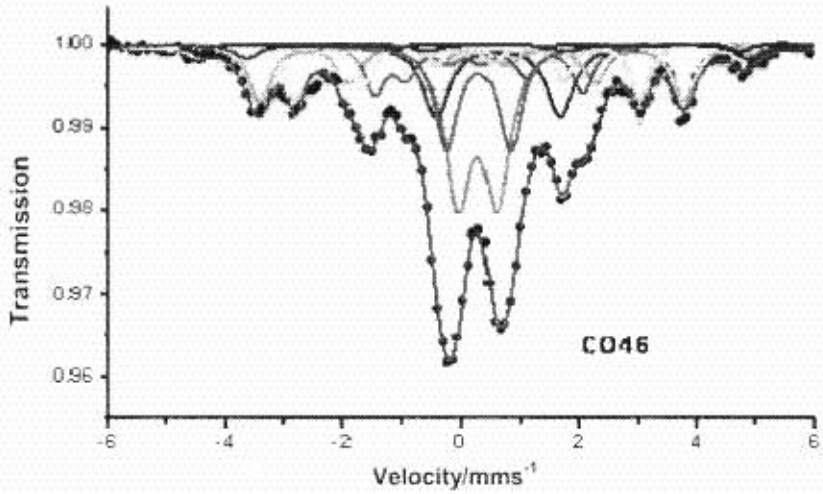


**Figure 3.13** Room temperature MAS spectra of the catalyst that was activated with CO and subjected to the Fischer-Tropsch synthesis using an $H_2/CO$ ratio of 1.0

The phase composition of the catalyst that was activated and subjected to the Fischer-Tropsch synthesis using an $H_2/CO$ ratio of 2.0 (R073) is shown in Figure 3.14. The spectrum was fitted with three quadrupole doublets and three sextets. The assignment of sub-spectra was done such that a $Fe^{3+}$ species contributed about 41%, a $Fe^{2+}$ species contributed about 16% and $\chi$-$Fe_5C_2$ about 43% of the total iron bearing components.

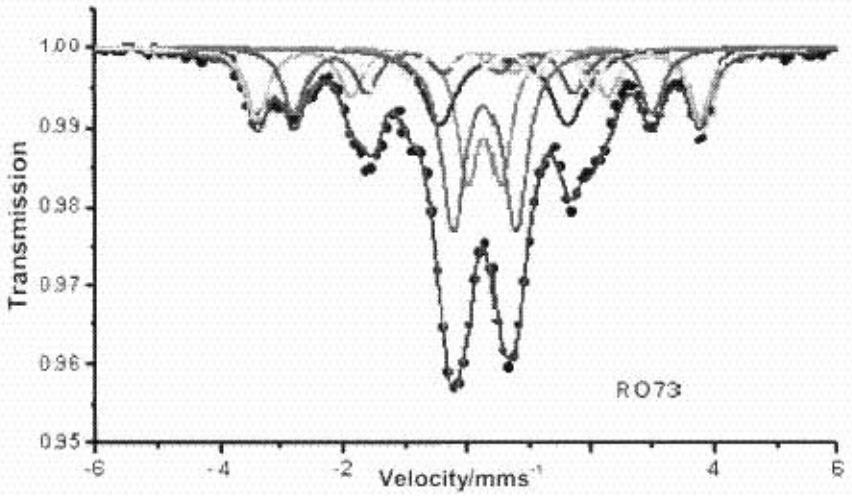


**Figure 3.14** Room temperature MAS spectra of the catalyst that was activated and subjected to the Fischer-Tropsch synthesis using an $H_2/CO$ ratio of 2.0

### 3.2.2 XRD Results

X-ray diffractograms before and after wax melt experiments are shown in Figure 3.15 and Figure 3.16 respectively. Diffraction peaks due to wax dominated the diffractograms obtained before heating. The wax peaks were no longer present in the diffractogram after heating and subsequent melting of the wax, but, as a consequence of the small crystallite size of the sample material, the diffractograms obtained after wax melting have reflections with low intensity and poor resolution.

A prominent peak, due to an iron carbide phase, at a diffraction angle of approximately $2\theta = 51°$ was observed in all samples which had been exposed to either synthesis gas or CO or both. However, due to low intensity counts and poor peak resolution, this peak could not be assigned to a specific iron carbide phase such as $\chi$-$Fe_5C_2$. The intensity of the carbide peak, although higher in samples that had been subjected to the Fischer-Tropsch synthesis (R073 and C046), could still not be unambiguously assigned to a specific carbide phase. In addition to the iron carbide phase, peaks due to the presence of either maghemite ($\gamma$-$Fe_2O_3$) or magnetite ($Fe_3O_4$) were observed in the samples that were subjected to the Fischer-Tropsch synthesis.

The diffractogram of the $H_2$ activated sample, D113, shows a peak at a diffraction angle of approximately $2\theta = 52.5°$ before any wax was melted. This is possibly due to metallic iron ($\alpha$-Fe). In addition a broad peak in the region $2\theta = 17 - 27°$ is observed upon heating the sample and is possibly due to partially melted wax.

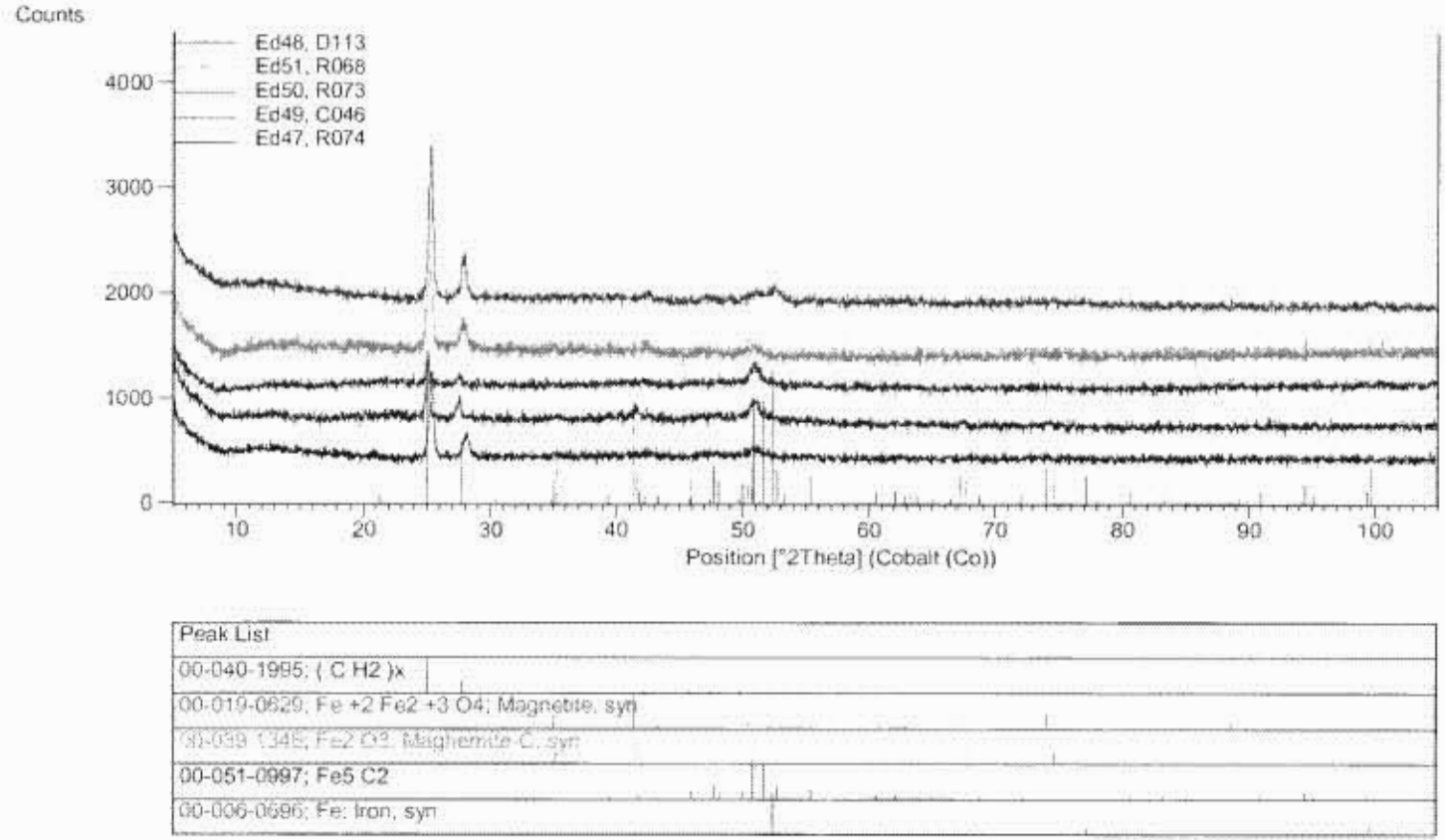


**Figure 3.15** X-ray diffractograms before wax melting

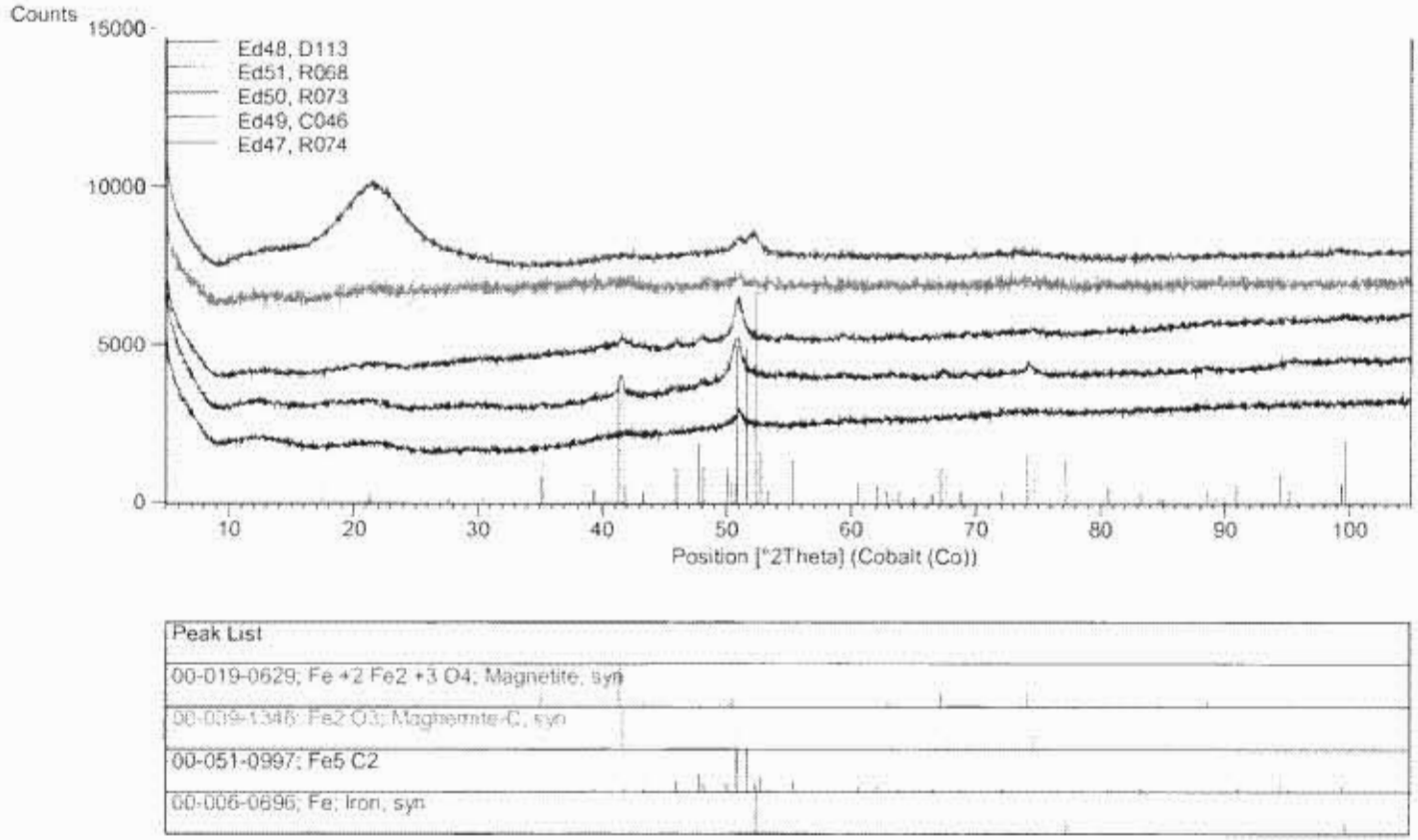


**Figure 3.16** X-ray diffractograms after wax melting

### 3.2.3 TEM Results

TEM images for samples subjected to activation are shown in Figure 3.17. Images of samples which were activated and then subjected to the Fischer-Tropsch synthesis are shown in Figure 3.18.

A variation in the activation procedure leads to clear differences that can be observed in the images for the samples subjected to either $H_2$, CO or syngas activation. For CO activation in particular (R074) it can be seen that crystallites of approximately 20 nm in diameter had started forming.

Distinct differences can also be observed for samples that have comparatively been exposed to the least amount of CO during both activation and synthesis (R073 – activation $H_2$/CO ratio of 2.0 and a Fischer-Tropsch synthesis $H_2$/CO ratio of 2.0) and the most CO during both activation and synthesis (C046 – CO activation and a Fischer-Tropsch synthesis $H_2$/CO ratio of 1.0). For R073 and C046 eliptical crystallites of approximately 20 – 50 nm in size were observed. These crystallites however appear more dispersed in sample R073.

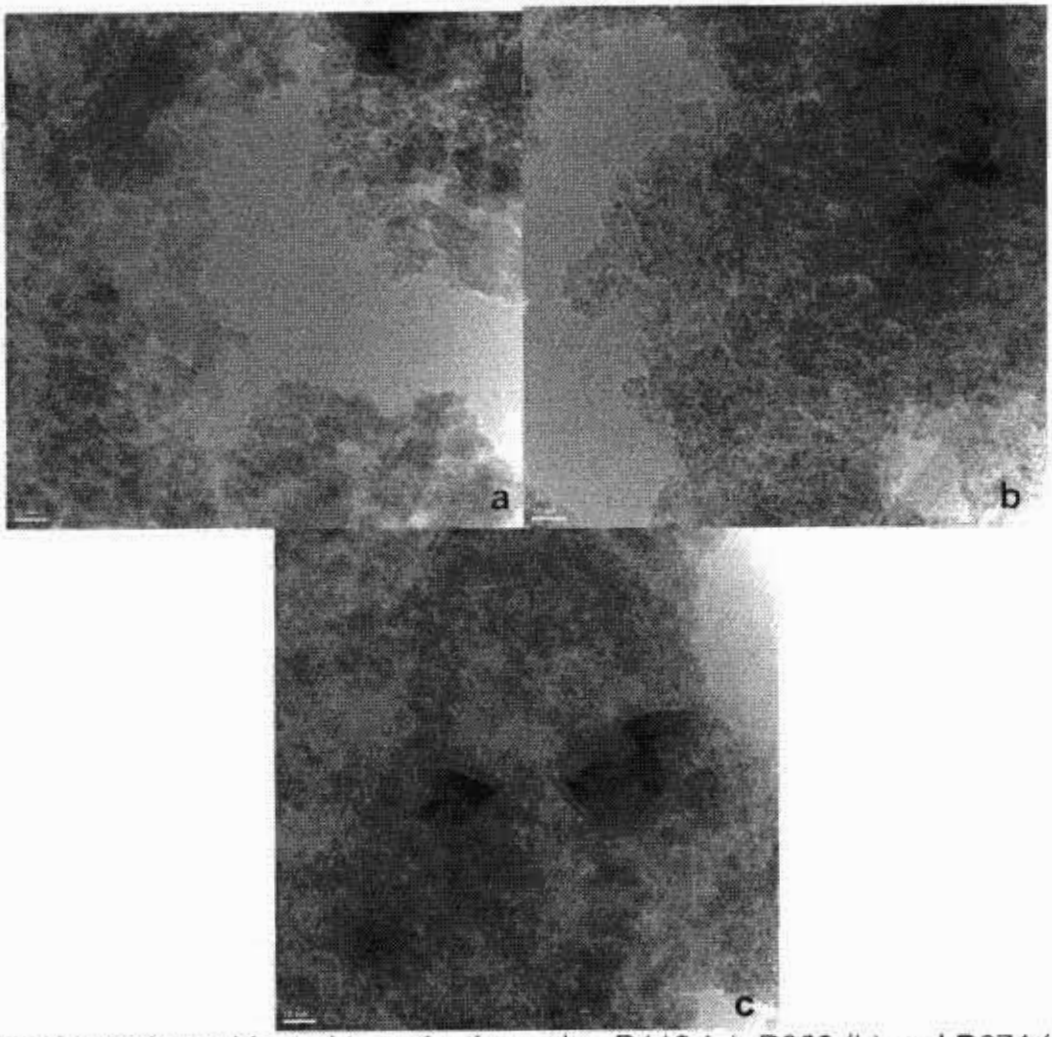


**Figure 3.17** TEM images of samples subjected to activation only - D113 (a), R068 (b) and R074 (c)

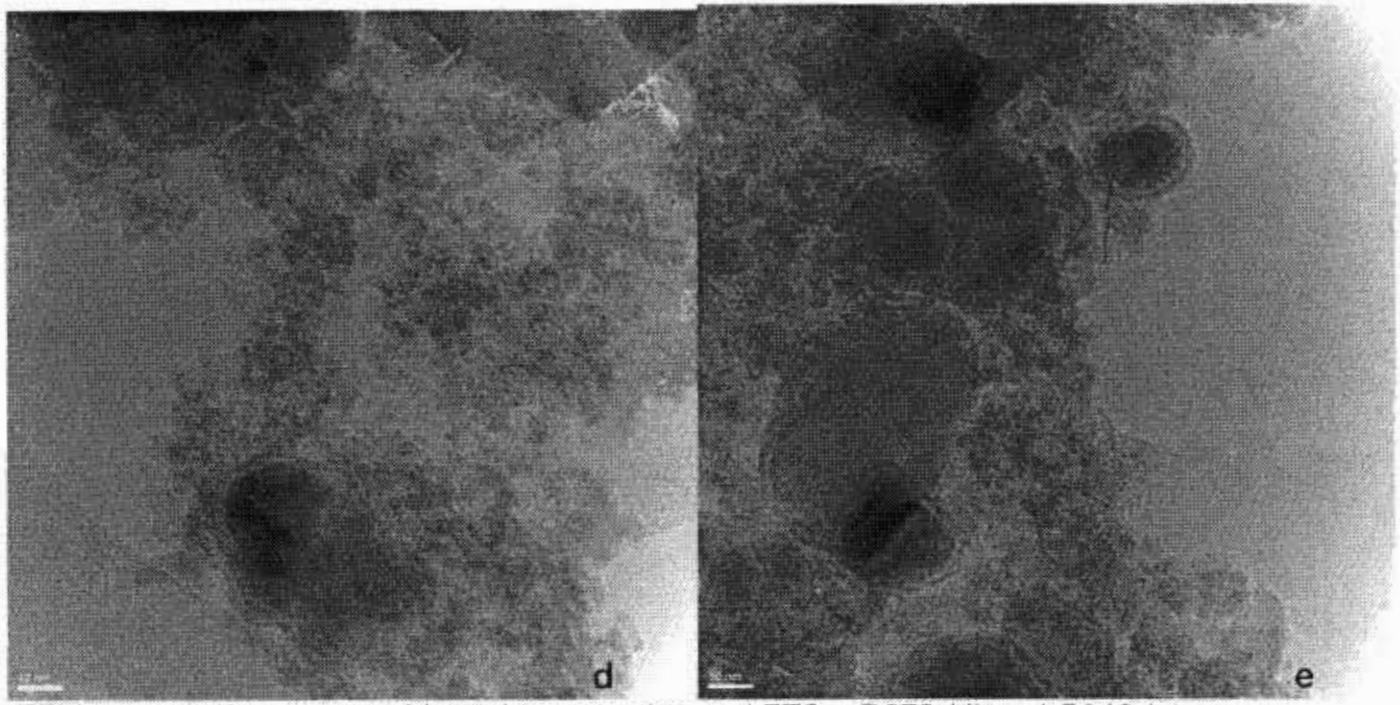


**Figure 3.18** TEM images of samples subjected to activation and FTS – R073 (d) and C046 (e)

# 4 Discussion

## 4.1 Activation and Fischer-Tropsch Synthesis

### 4.1.1 Catalyst Activation

The rate of CO conversion during activation of the catalysts at various partial pressures of CO is shown in Figure 4.1. The activation was carried out for 36 h under 12 bar total pressure at a temperature of 230°C. The differing conditions during each activation led to varying rates of CO conversion due to the varying CO and $H_2$ partial pressures.

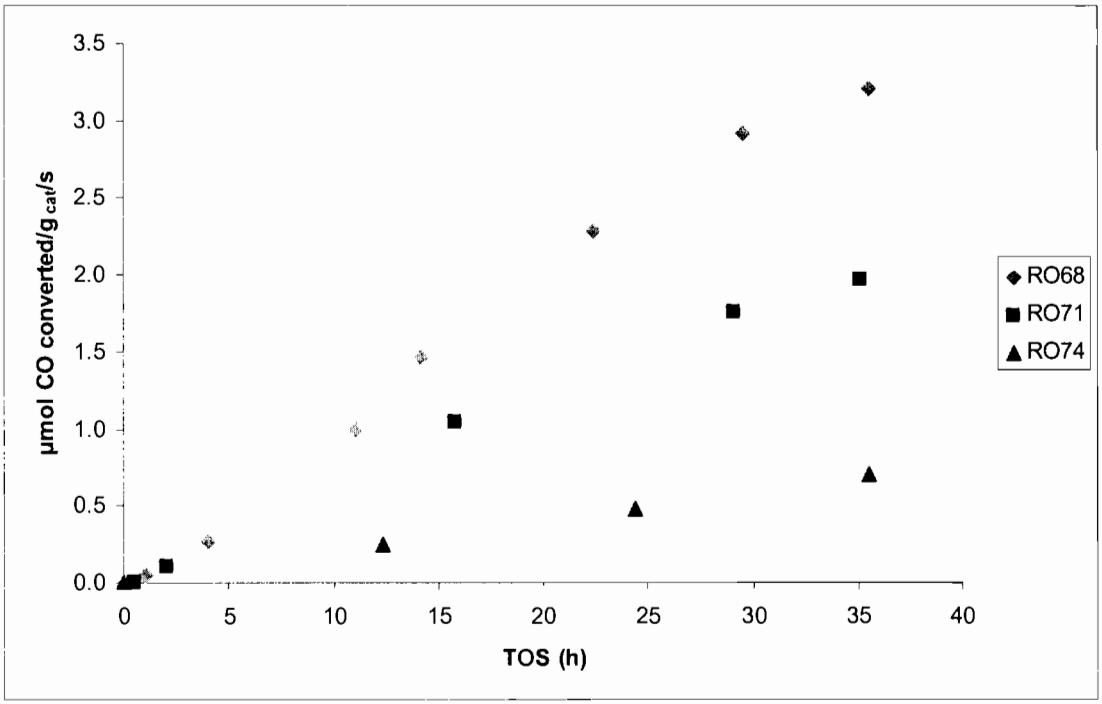


**Figure 4.1** Comparison of activity during activation with CO (R074) and syngas having $H_2$/CO ratios of 2.0 (R068) and 1.0 (R071)

The rate of CO conversion at the end of each activation hence cannot be directly compared due to the varying conditions employed. The different activation procedures can however be evaluated and compared with each in terms of initial Fischer-Tropsch activity after introduction of synthesis conditions.

By comparing the iron phases present, according to MAS, with the rate of CO conversion at the end of each activation procedure, one can assess how the activating gas was consumed and in which manner it transformed the catalyst into a phase that would be active for the Fischer-Tropsch synthesis. Table 4.1 shows the relationship between activating gas used and the iron phases detected by MAS after 36 h of activation.

**Table 4.1** Relationship between activating gas and iron phases present after activation

| Sample | Activation $H_2/CO$ Ratio | Iron Phases Present (MAS) | % Relative Area |
|---|---|---|---|
| R074 | CO | $Fe^{3+}$, $Fe^{2+}$, $\chi$-$Fe_5C_2$ | 72.3, 10, 17.7 |
| R071 | 1.0 | $Fe^{3+}$, $Fe^{2+}$, $\chi$-$Fe_5C_2$ | 82.6, 8.7, 8.7 |
| R068 | 2.0 | $Fe^{3+}$, $Fe^{2+}$ | 91.9, 8.1 |

What can be observed from the above table is that the catalyst sample activated with pure CO (R074) produced the most iron carbide. This points to the fact that, as expected, during CO activation Equation 3.2 is the predominant reaction taking place and results in carbon deposition as either carbidic or graphitic carbon and $CO_2$ formation. In fact it can be estimated that during the 36 hrs of activation with pure CO, approximately 45.4 mmol $C/g_{cat}$ was incorporated into or deposited on the catalyst.

Furthermore, combining the fact that MAS indicates the presence of 17.7% Hägg carbide, and the estimation that the amount of carbon deposited on or incorporated into the catalyst at the end of activation corresponds to 45.4 mmol, this leads to the conclusion that approximately 0.74 mmol of carbon deposited, is present as iron carbide. Therefore approximately 44.7 $mmol/g_{cat}$ is deposited as free carbon (see Appendix A for calculation).

In addition, comparing the TEM images of the activated samples (Figure 3.17) it can be seen that for the CO activated sample, structures similar in appearance to the model proposed for a stable iron catalyst during synthesis[13] are present (Figure 4.2)

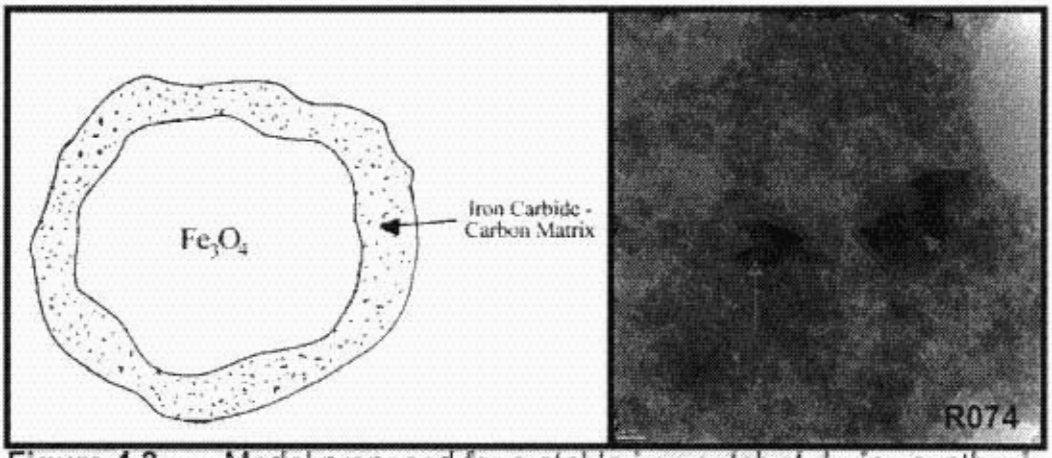


**Figure 4.2** Model proposed for a stable iron catalyst during synthesis and structures in the TEM image of the CO activated sample (R074)

Again, this gives an indication of the manner in which CO is converted during activation with pure CO gas; the deposition of carbon as carbidic carbon resulting in the structures as seen above. Clear evidence of graphitic carbon is however not visible from the TEM images.

For the catalyst sample activated with a synthesis gas $H_2$/CO ratio of 1.0 (R071), the amount of Hägg carbide present was found to be approximately 8.7% according to MAS. This would suggest that, due to the relatively high CO content of the activating gas (as compared to the sample activated with a synthesis gas $H_2$/CO ratio of 2.0), the deposition of carbon resulting in Hägg carbide formation occurs.

Since there is now $H_2$ present, some Fischer-Tropsch synthesis can also take place as a result of the presence of the carbide phase which had formed. Thus for sample R071 the rate at which CO is converted is most likely due to carbide formation (in conjunction with some graphitic carbon deposition) as well as to some Fischer-Tropsch activity.

In the same vain it could be said that the observed rate of CO conversion during activation using a synthesis gas $H_2$/CO ratio of 2.0 (R068), can be attributed to the conversion of CO into Fischer-Tropsch products and $CO_2$; the comparatively higher $H_2$ partial pressure resulting in the greater contribution of Fischer-Tropsch activity in the conversion of CO.

However, no iron carbide phase, which would facilitate any Fischer-Tropsch activity, was found to be present according to MAS. This could however be explained by looking at the transitions the catalyst undergoes before reaching its active form.

During activation an iron catalyst will transform from hematite to magnetite and then to iron carbide[17,22,23,24]. van Steen *et al* (2008) proposed transitions between the various phases in a precipitated iron-based Fischer-Tropsch catalyst (see Figure 4.3)[10]. Although this shows the transitions of a catalyst during the Fischer-Tropsch synthesis, it would not be unreasonable to assume that steps (a), (c) and (d) may also occur during activation with synthesis gas.

Thus for R068, it could be said that during the beginning stages of activation, carbon gets incorporated into the magnetite phase and forms iron carbides as in steps (a) to (c) of Figure 4.3. This results in Fischer-Tropsch activity during activation and the water which then forms due to this Fischer-Tropsch activity can re-oxidize some of the iron carbides to form magnetite as in steps (d) to (a). For this reason then, no carbide phase is possibly detected by MAS.

However, if one considers the XRD diffractogram of sample R068 (Figure 3.16), a slight hump is observed in the region of approximately $2\theta = 52°C$ which could possibly be attributed to the Hägg carbide phase. However, due to poor peak resolution and low intensity counts, this cannot be said with certainty.

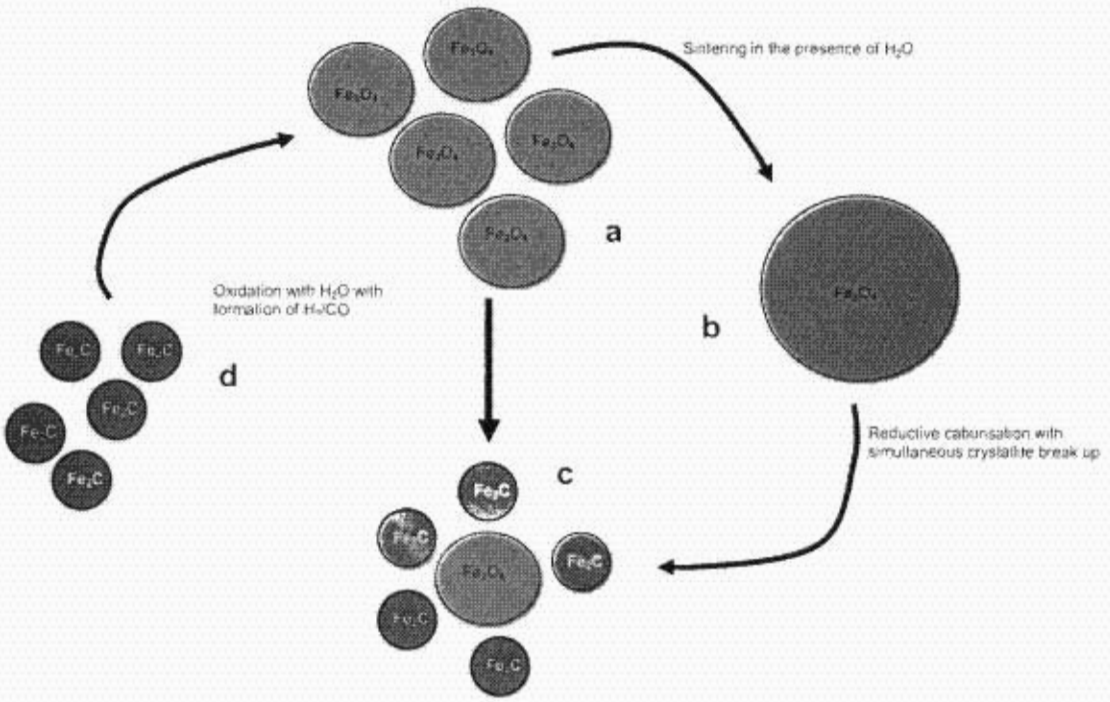


**Figure 4.3** Dynamic transitions of a precipitated iron-based Fischer-Tropsch catalyst[10]

On the other hand, no magnetite ($Fe_3O_4$) phase was detected by MAS either. One possibility for magnetite not being detected as a distinct phase is because it is an iron (II, III) species and is thus probably detected as either $Fe^{3+}$ or $Fe^{2+}$ and contributes to the reported (by MAS) percentage relative areas of the these species. Since $Fe^{3+}$ and $Fe^{2+}$ are in the high spin state in magnetite,[38] it is certainly possible that MAS could detect magnetite as either $Fe^{3+}$ or $Fe^{2+}$ and thus for this reason MAS shows a contribution to the total iron content of 91.9 and 8.1% for $Fe^{3+}$ and $Fe^{2+}$ respectively.

Added to the above, small crystallite sizes of the magnetite phase could contribute to the fact that it is not detected by MAS. Again looking at the XRD diffractogram of sample R068, it can be noticed that to all intents and purposes, no peaks (except for the slight hump which could be attributed to Hägg carbide) are visible. This poor peak resolution and low intensity counts are indicative of small crystallite sizes; crystallite sizes below 100nm exhibiting line broadening due to incomplete destructive interference in scattering directions[35]. Figure 3.17(b) confirms the small

crystallite size of sample R068; all of the crystallites appearing to be less than 10 nm in size.

The assumption that small magnetite crystallite size is responsible for it not being detected by MAS is supported by Hartridge *et al* (1997) who studied single phase magnetite powders with crystallite sizes ranging from 8 – 50 nm using XRD and MAS. They found that quadrupole splitting of the B sites increased with decreasing crystallite size before the spectrum collapsed into a doublet at the smallest sizes, *i.e.*, it thus became increasingly difficult to identify the single magnetite phase as crystallite sizes decreased[39].

For sample R068 then, it can be said, that the rate of CO conversion is most likely predominantly due to Fischer-Tropsch activity after initial carbide formation. However, since no clear evidence for this could be gathered by the characterization techniques employed, the nature of CO conversion during activation with a synthesis gas $H_2$/CO ratio of 2.0 is purely conjecture. If however MAS at cryogenic temperatures were to have been available, the above assumptions may have been confirmed. This is because at these low temperatures, the Mössbauer intensity can be considerably improved resulting in improved identification of distinct phases[35].

### 4.1.2 Fischer-Tropsch Synthesis

Figure 4.4 shows the comparative activities of the various samples during the Fischer-Tropsch synthesis (dotted line indicates end of activation). The Fischer-Tropsch synthesis was carried out at a temperature of 240°C and under 20 bar total pressure. The gas hourly space velocity was adjusted to maintain a synthesis gas conversion of approximately 30%.

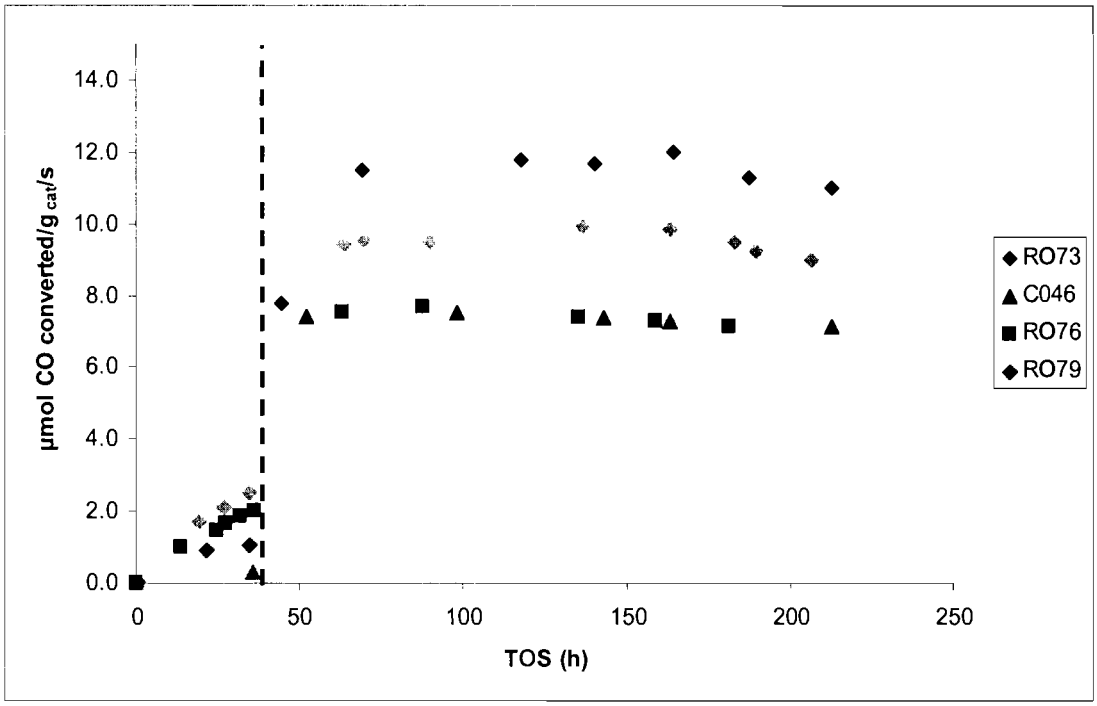


| Run | Activation $H_2/CO$ ratio | FTS $H_2/CO$ ratio |
|---|---|---|
| R073 | 2.0 | 2.0 |
| R076 | 1.0 | 1.0 |
| C046 | CO | 1.0 |
| R079 | CO | 2.0 |

**Figure 4.4** Comparative activities of samples during Fischer-Tropsch synthesis

From the above figure, the effect of the activation procedures can be compared by looking at the initial activities under the Fischer-Tropsch synthesis after activation.

Samples activated with CO (C046) and a synthesis gas $H_2/CO$ ratio of 1.0 (R076) were subjected to the Fischer-Tropsch synthesis with a synthesis gas $H_2/CO$ ratio of 1.0. It can be seen that approximately the same initial activity was achieved after switching to synthesis conditions. Also, their activities remained approximately identical throughout their time on stream and exhibited similar deactivation profiles.

The similar initial activities observed could be explained by combining the results obtained from the various characterization techniques, *i.e.*, XRD, MAS and TEM.

According to MAS, CO activation results in the formation of almost twice as much Hägg carbide as compared to activation with synthesis gas having an $H_2/CO$ ratio of 1.0 (17.7% compared to 8.7% - see Table 3.4). However, though more iron carbides would have been present at the start of the Fischer-Tropsch synthesis for run C046, the magnetite starts sintering. The subsequent loss in surface area on which carbide formation can take place thus leads to lower than expected Fischer-Tropsch activity, and in this case, the sintering of the catalyst results in Fischer-Tropsch activity which is similar to when having started with approximately half the iron carbide content as is the case with R076.

Evidence of sintering can be seen in the TEM image of sample C046 where there appears to be an agglomeration of large crystallites (Figure 3.18). Also, MAS shows the presence of magnetite which was not detected after activation with CO. As postulated in section 4.1.1, after activation the magnetite crystallites may have been too small to be detected by MAS. Under Fischer-Tropsch synthesis conditions however, the magnetite crystallites sinter and can be detected, with 9% of the spent catalyst composition being attributed to this phase (see Table 3.4). XRD also shows peaks possibly due to magnetite for the spent catalyst (C046) whereas it is not clearly visible in the CO activated sample (R074). Again, this points to sintering with time on stream.

Furthermore, if one looks at the water partial pressures present, it is evident that, due to the higher water partial pressures present during run C046 as compared to run R076 (Figure 4.5), conditions were more favourable for sintering to occur as depicted in Figure 4.3.

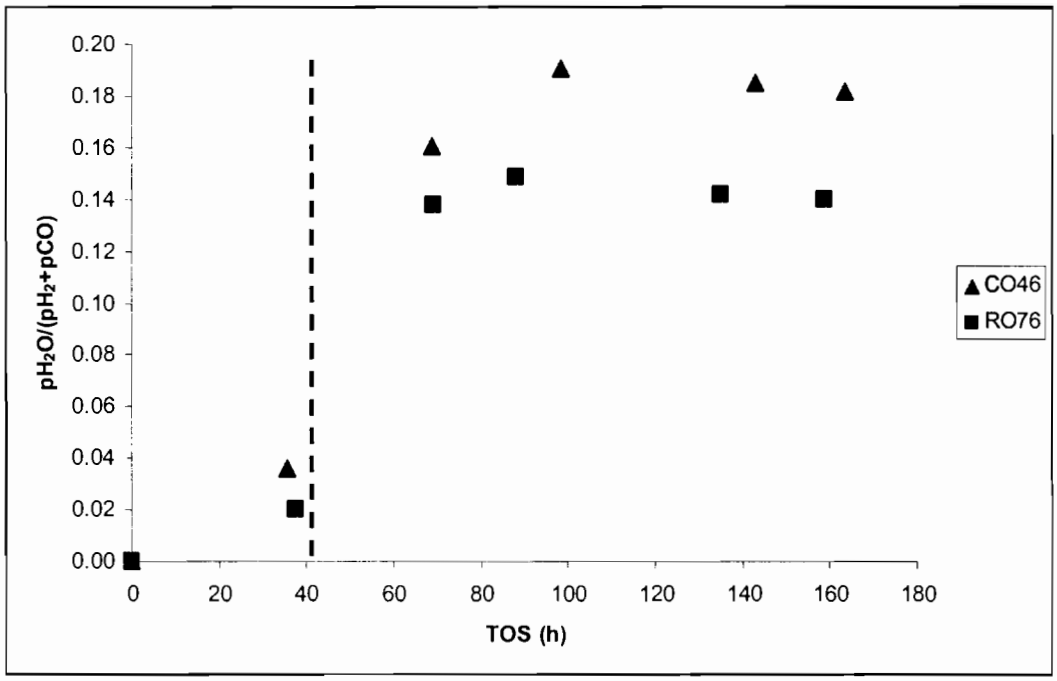


**Figure 4.5** Comparison of the ratios of water partial pressures to synthesis gas partial pressures during activation and synthesis for runs C046 and R076 (dotted line indicates end of activation)

The higher water partial pressures could be ascribed to the greater amount of iron carbide that would have been present after CO reduction. This resulted in comparatively higher initial Fischer-Tropsch activity resulting in more water being formed. However, this higher activity is not apparent due to the sintering induced by the higher water partial pressures produced by said higher Fischer-Tropsch activity.

Comparing samples activated with CO (R079) and with a synthesis gas $H_2/CO$ ratio of 2.0 (R073), it can be seen that differing initial activities were obtained when subjected to the Fischer-Tropsch synthesis with a synthesis gas $H_2/CO$ ratio of 2.0. The CO activated sample exhibited a greater initial activity as compared to the synthesis gas activated sample (11.5 versus 9.43 µmol CO converted/$g_{cat}$/s). Since CO activation yielded the larger percentage of Hägg carbide as compared to activation with a synthesis gas $H_2/CO$ ratio of 2.0 (17.7% as compared to 0% - see Table 3.4), it would thus be expected for this to be the case.

The respective Fischer-Tropsch activities of each sample were both sustained for approximately 160 h time on stream before deactivation set in.

Comparing the Fischer-Tropsch activities of the two CO activated samples (C046 and R079), the higher activity was obtained with the sample subjected to the Fischer-Tropsch synthesis with a synthesis gas $H_2/CO$ ratio of 2.0 (R079). This is to be expected since a higher $H_2$ partial pressure would result in greater Fischer-Tropsch activity. It was however previously stated that the greater carbide content of a CO activated catalyst led to sintering during the Fischer-Tropsch synthesis which in turn led to reduced catalyst activity. It could be argued then that, by following this reasoning, the sample subjected to the Fischer-Tropsch synthesis with a synthesis gas $H_2/CO$ ratio of 2.0 after CO activation should have exhibited even lower activity due to even higher Fischer-Tropsch activity leading to more water being formed and thus leading to an even greater degree of sintering.

As an explanation to the above, seemingly contradictory, observation it was earlier calculated that during CO activation, only approximately 0.74 mmol of carbon deposited forms iron carbide, with approximately 44.7 $mmol/g_{cat}$ being deposited as free carbon. Now if one looks at the methane selectivity for run R079 (CO activation and Fischer-Tropsch synthesis with a synthesis gas $H_2/CO$ ratio of 2.0), a peak in methane selectivity is observed during the initial stages of the Fischer-Tropsch synthesis whereas this is not the case for run R076 (Figure 4.6).

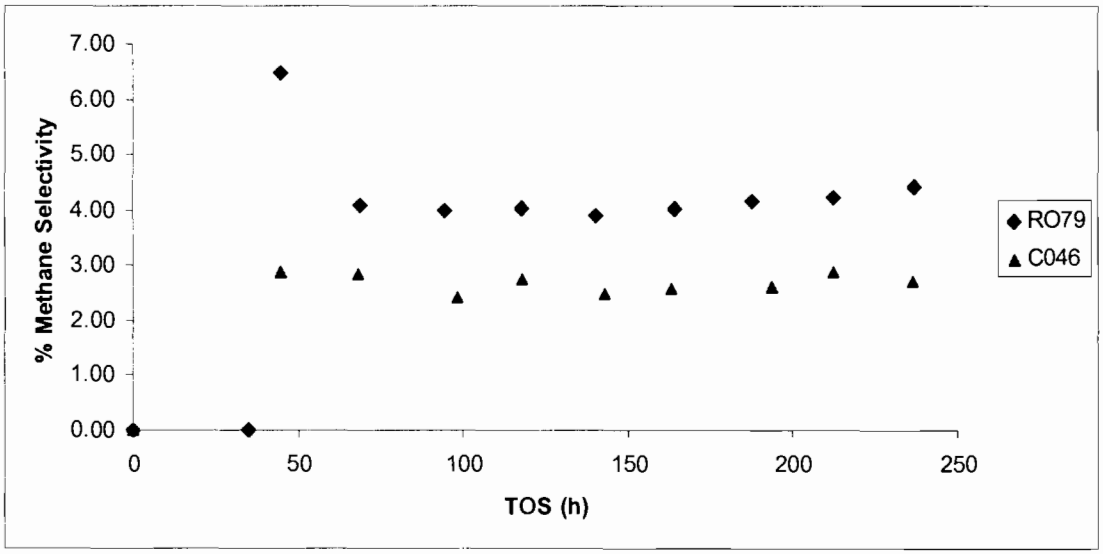


**Figure 4.6** Comparison of methane selectivities during runs R079 and C046

A reason for the above observation could be that carbon which had been deposited during activation with CO is being converted to methane upon the introduction of $H_2$ during the Fischer-Tropsch synthesis as in Equation 4.1.

$$C + 2H_2 \rightarrow CH_4 \qquad (4.1)$$

The peak in methane selectivity seen for R079 could thus be due to the higher $H_2/CO$ ratio of the synthesis gas introduced at the start the Fischer-Tropsch synthesis; the excess $H_2$ present reacts with the excess carbon deposited on the surface of the catalyst therefore effectively cleaning the catalyst surface to a certain extent. However, due to less $H_2$ being present at the initiation of the Fischer-Tropsch synthesis of run C046, this cleaning effect facilitated by excess $H_2$ occurs to a lesser extent and results in lower Fischer-Tropsch activity as compared to run R079 due to the fouled catalyst.

It should be kept in mind that with a lower synthesis gas $H_2/CO$ ratio of 1.0 during the Fischer-Tropsch synthesis, as for run C046, the possibility for CO being converted to graphitic carbon, which could lead to further fouling during the Fischer-Tropsch synthesis, also exists.

By looking at the deactivation profile of run C046, it is noticeable that deactivation starts almost from after the initiation of the Fischer-Tropsch synthesis. This could be seen as an indication that continual carbon deposition is indeed taking place along with the sintering of crystallites. This therefore leads to C046 having lower Fischer-Tropsch activity that R079.

## 4.2 Catalyst Deactivation

Figure 4.7 shows the start of deactivation (vertical dashed line) and the slopes of the deactivation profiles for the catalyst samples which had been subjected to activation with CO (R079) and with a synthesis gas $H_2/CO$ ratio of 2.0 (R073) and then to the Fischer-Tropsch synthesis with a synthesis gas $H_2/CO$ ratio of 2.0.

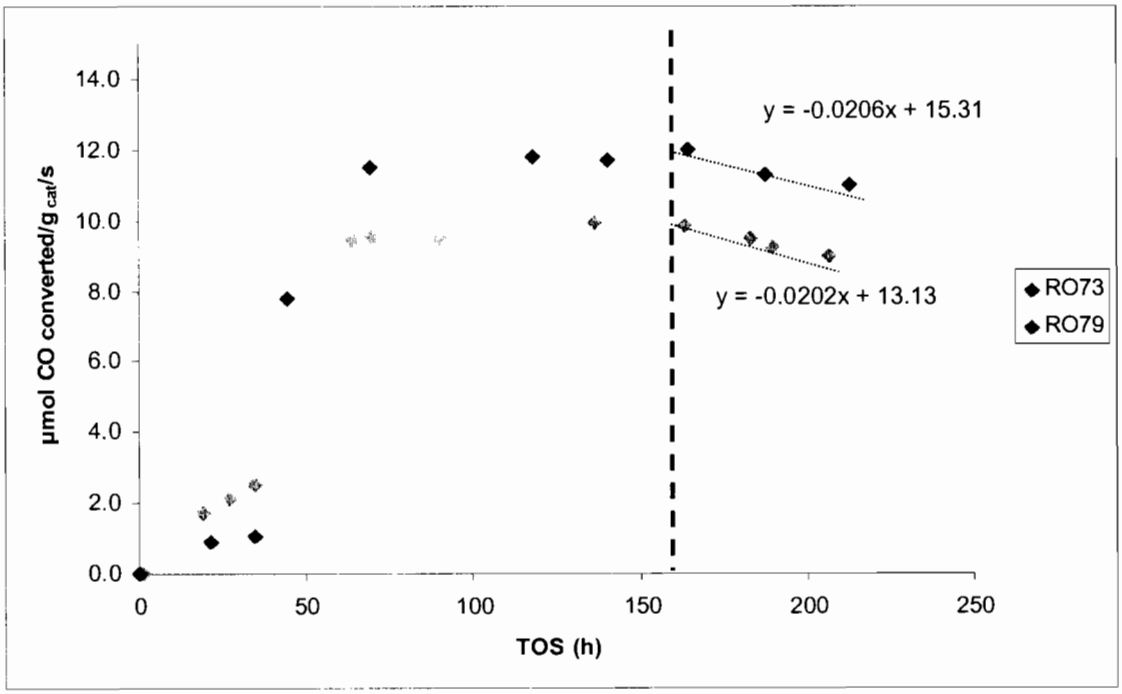


| Run | Activation $H_2/CO$ ratio | FTS $H_2/CO$ ratio |
|---|---|---|
| R073 | 2.0 | 2.0 |
| R079 | CO | 2.0 |

**Figure 4.7** Graph indicating the onset of deactivation and slope of the deactivation profiles for runs R073 and R079

As can be seen, deactivation set in after approximately the same time on line for both samples and had identical slopes. This therefore suggests that the mechanism of deactivation for both samples were the same.

Figure 4.8 shows the deactivation profiles of the samples that had been activated with CO (C046) and a synthesis gas $H_2/CO$ ratio of 1.0 (R076) and subjected to the Fischer-Tropsch synthesis with a synthesis gas $H_2/CO$ ratio of 1.0.

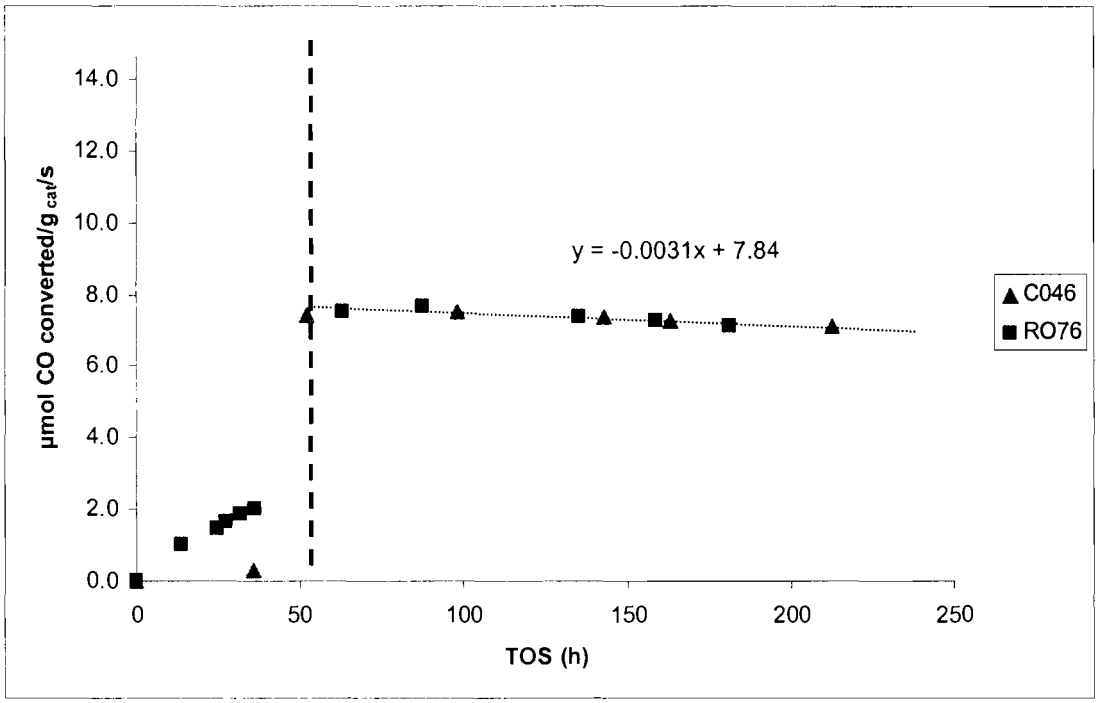


| Run | Activation $H_2/CO$ ratio | FTS $H_2/CO$ ratio |
|---|---|---|
| R076 | 1.0 | 1.0 |
| C046 | CO | 1.0 |

**Figure 4.8** Graph indicating the onset of deactivation and slope of the deactivation profiles for runs R076 and C046

For these samples it can be seen that deactivation also set in at approximately the same time and that the slope of the deactivation profiles for each run was the same. This suggests that for these samples the deactivation mechanism would also be the same but different to that occurring in R073 and R079.

In terms of deactivation rate equations (Chapter 1, section 1.3.6) the slope of the deactivation profile gives the deactivation rate constant. In the above cases, $k_d$ = 0.02 μmol CO/$g_{cat}$/s for R073 and R079 and $k_d$ = 0.003 μmol CO/$g_{cat}$/s for R076 and C046.

### 4.2.1 Modelling of Catalyst Deactivation

In Chapter 1, section 1.3.6, various types of deactivation rate equations for different types of deactivation mechanisms are presented (Table 1.7). It was seen that deactivation can occur not just as a result of a single deactivation mechanism, but can also occur due to a combination of deactivation mechanisms. Table 4.2 shows the rate equations that can be applied to the run data obtained and the type of deactivation it describes.

**Table 4.2** Rate equations and the type of deactivation it describes (from ref. 26,32, 33, 34)

| Rate Equation | Type of deactivation it describes |
|---|---|
| $1/A^P t^{np}+1$ (Voorhies Equation) | Describes the amount of carbon on the surface of a catalyst after a time *t*. The fouling parameter, A, would be the value $k_d$ obtained from the slope of the deactivation profile (if $p$ = 1). This equation could empirically describe deactivation due to carbon deposition. |
| $-da/dt = k_d$ | Describes exponential deactivation. This would occur in a situation where a deactivation mechanism results in a continuous loss of activity once it takes effect. |
| $-da/dt = k_d.a$ | Describes deactivation which is as a result of independent occurrences on the catalytic surface. |
| $-da/dt = k_d/a$ | Describes deactivation due to a combination of mechanisms. |

When attempting to fit the data to the rate equations in the following sections, only data for runs C046 and R079 are used. Of course, the data for runs R076 and R073 could also have been used since their deactivation profiles and values for $k_d$ are the same as for C046 and R079 respectively.

It should further be noted that due to limited time allocated for the use of the reactor system, time on line was limited to at most 250 h. The time of experimentation was thus too short to distinguish between the various deactivation models given in literature. The evaluation of the models is therefore only an indication of how well they may describe the deactivation of the catalyst and were extrapolated with a view to determine what reaction time should be chosen to verify either of the models.

#### 4.2.1.1 Fitting data to the Voorhies Equation ($1/At^n + 1$)

Figure 4.9 shows the deactivation profiles for run C046 as well as the values obtained by fitting the data to the rate equation.

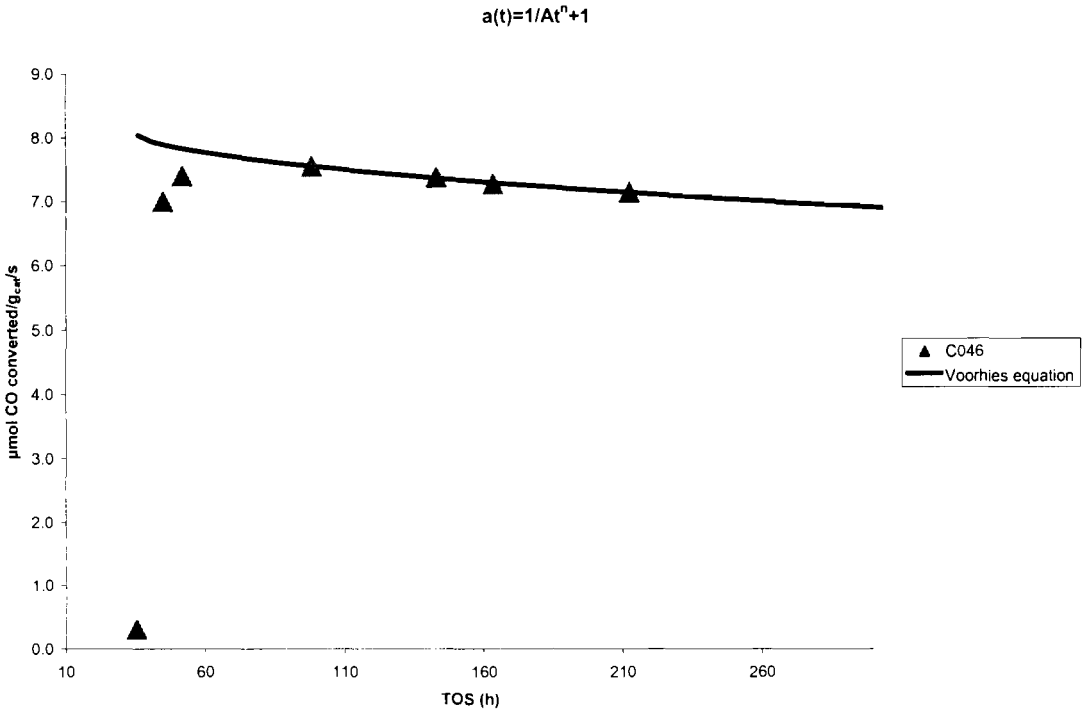


**Figure 4.9** Comparison between deactivation profile for run C046 and values obtained after fitting run data to the rate equation

It can be seen from the above figure that values obtained from the rate equation fit the actual data during deactivation quite well. The predicted long-term deactivation behaviour for run C046 is shown in Figure 4.10.

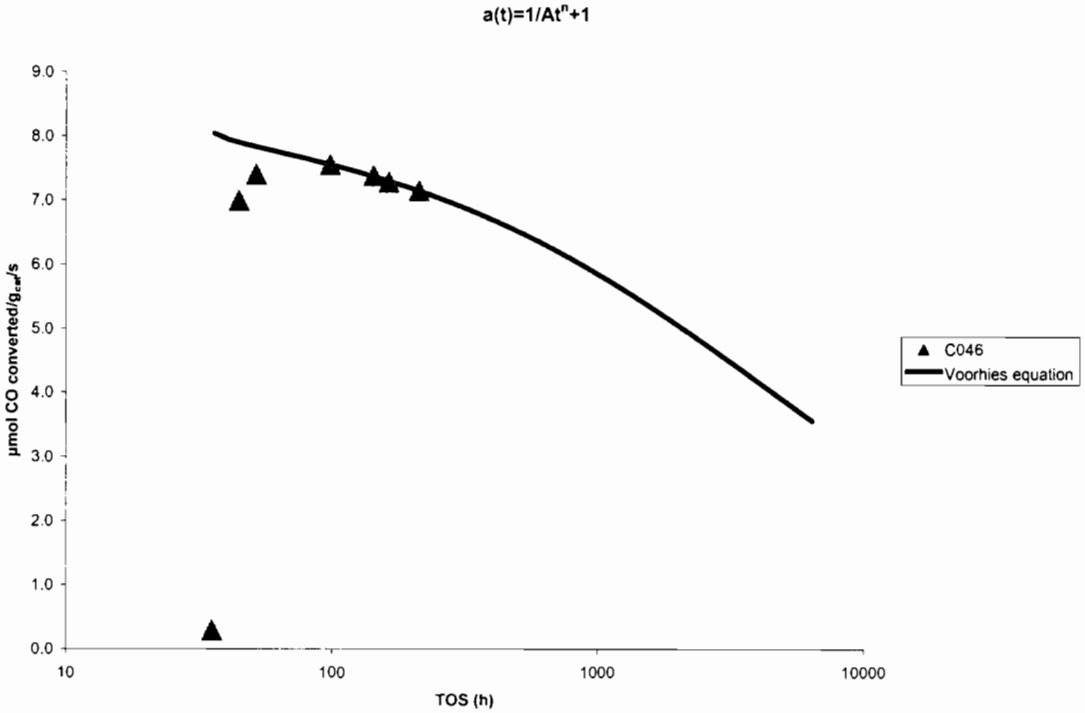


**Figure 4.10** Predicted long-term deactivation behaviour for run C046

To determine whether the deactivation will follow the predicted trend, the run would have to be repeated and continued for a longer time period.

In the case of run R079 it can be seen once again that the values obtained from the rate equation fit the actual data during deactivation quite well (Figure 4.11).The predicted long-term deactivation behaviour for run R079 is shown in Figure 4.12. Again a longer run would be needed to determine whether deactivation would follow the predicted trend.

It can be seen that the Voorhies equation fits the actual data obtained for C046 and R079 quite well and therefore suggests that a possible deactivation mechanism at play is fouling due to carbon deposition. In

the case of C046 and R076, carbon deposition would seem to occur from after the start of the Fischer-Tropsch synthesis, whereas it only starts occurring after approximately 163 h time on stream for R073 and R079.

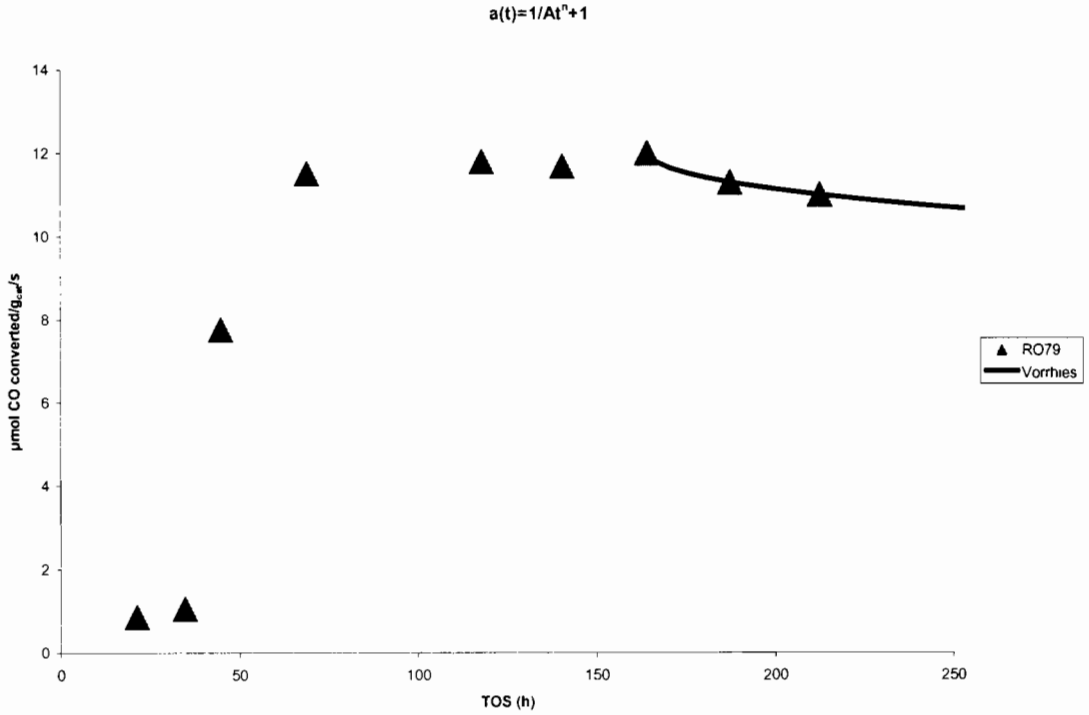


**Figure 4.11** Comparison between deactivation profile for run R079 and values obtained after fitting run data to the rate equation

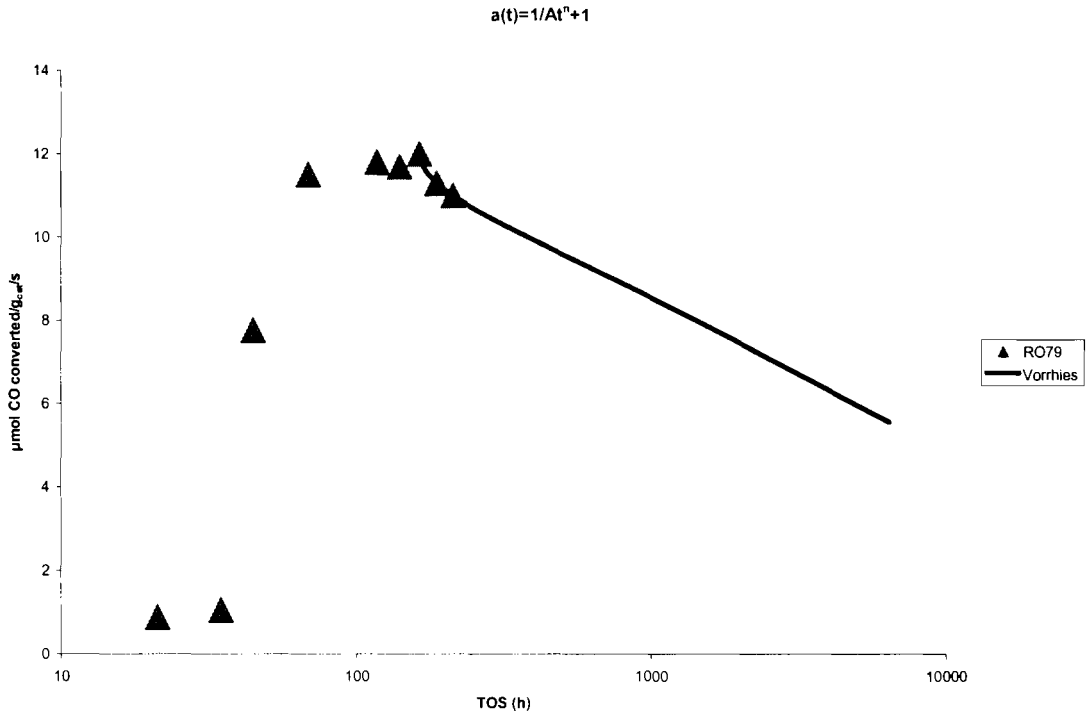


**Figure 4.12** Predicted long-term deactivation behaviour for run R079 according to the Voorhies equation

### 4.2.1.2 Fitting data to the equation -da/dt = $k_d$.a

Solving for $a$ yields the following equation:

$$a = e^{-k_d.t} \qquad (4.2)$$

Figure 4.13 shows the deactivation profile for run C046 as well as the values obtained by fitting the data to the above rate equation.

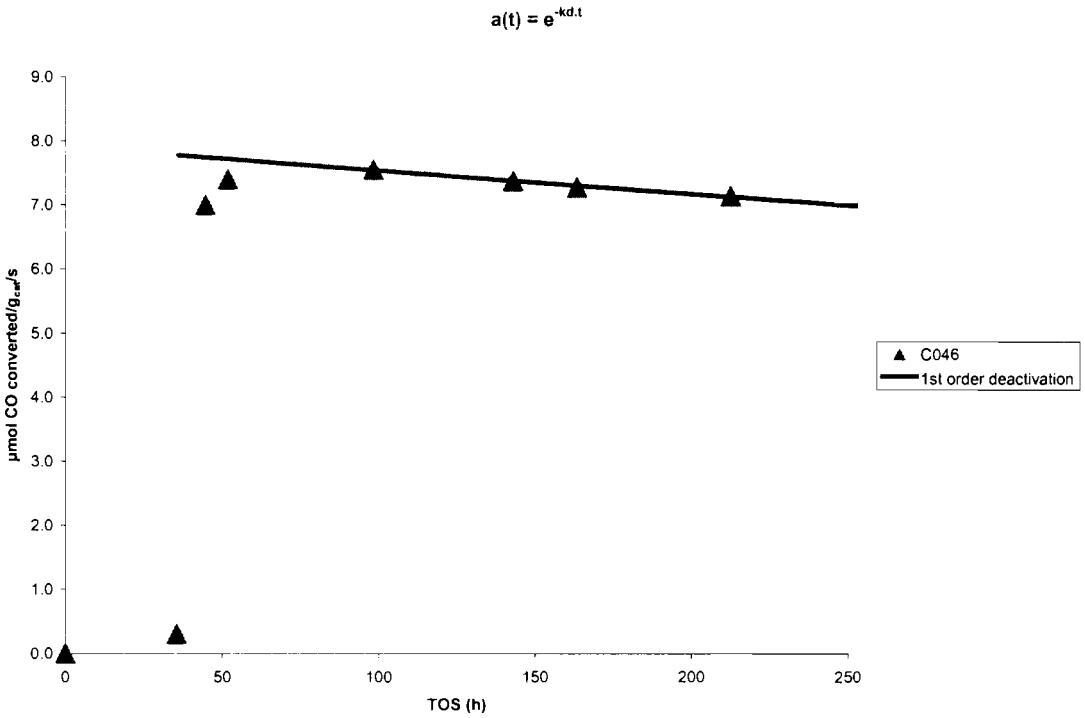


**Figure 4.13** Comparison between deactivation profile and values obtained after fitting run data to the rate equation $a = e^{-k_d.t}$ for run C046

As with the Voorhies equation, the values obtained fit the actual values quite well. The predicted long-term deactivation behaviour for run C046 is shown in Figure 4.14

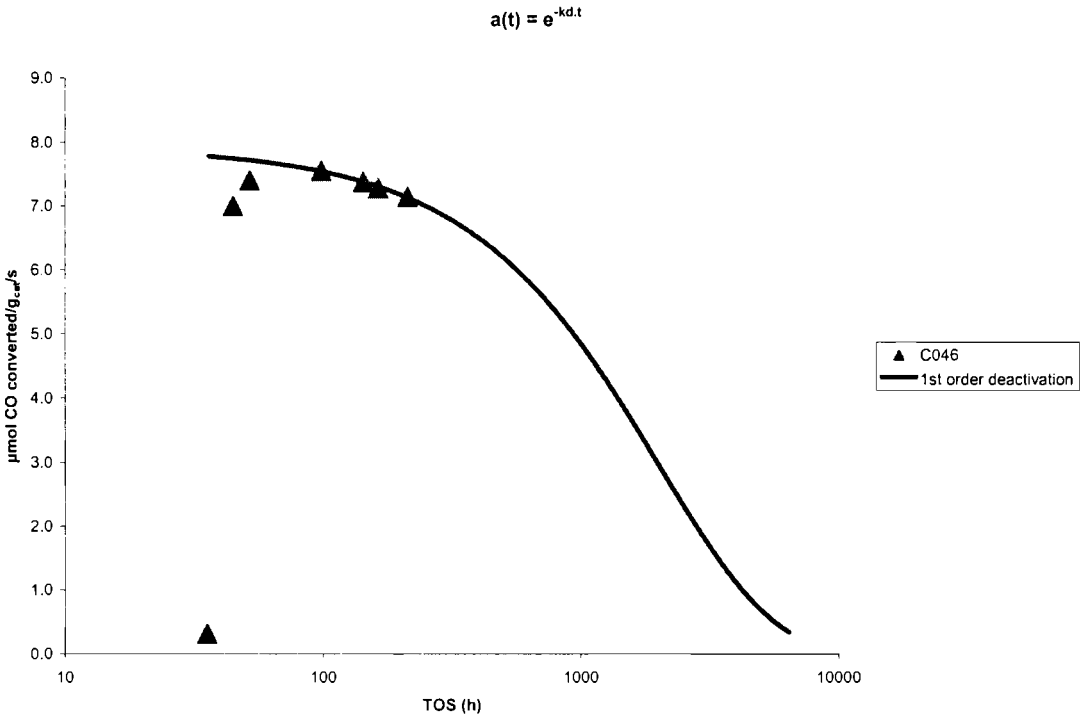


**Figure 4.14** Predicted long-term deactivation behaviour for run C046 according to the rate equation $a = e^{-k_d t}$

Compared to the Voorhies prediction, the first order deactivation predicts a much faster rate of deactivation for run C046 which would reach nearly zero activity after 10000 h time on stream, although the predicted rate of deactivation also appears to slow down as zero activity is approached.

For run R079, the predicted values using the equation $a = e^{-kd.t}$ again fit the actual values obtained during the observed deactivation quite well (Figure 4.15).

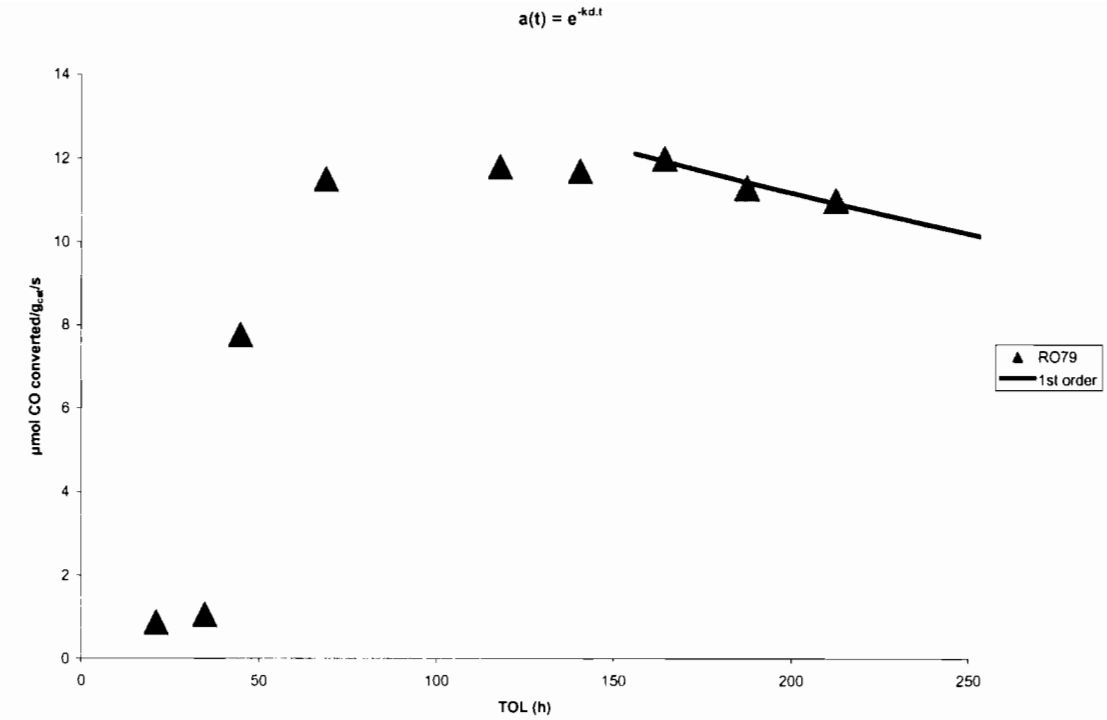


**Figure 4.15** Comparison between deactivation profile and values obtained after fitting run data to the rate equation $a = e^{-k_d t}$ for run R079

Again the predicted rate of deactivation is initially quite fast and then decreases as zero activity is approached (Figure 4.16). The actual behaviour can once again however only be observed if longer runs are to be performed.

Since the rate equation fits the actual data for both C046 and R079 once again, and it describes a situation where a deactivation mechanism results in a continuous loss of activity once it takes effect, it suggests again that the deactivation mechanism is similar in both cases, but which sets in earlier for C046 than it does for R079. Carbon deposition can be an example of such a mechanism. Also, the possibility that sintering (which is also an irreversible process at the Fischer-Tropsch synthesis conditions employed) resulted in low Fischer-Tropsch activity for run C046. This suggests then that since the rate equation fits the actual data for R079 as well, sintering is a mechanism of deactivation for R079 (and R073) as well.

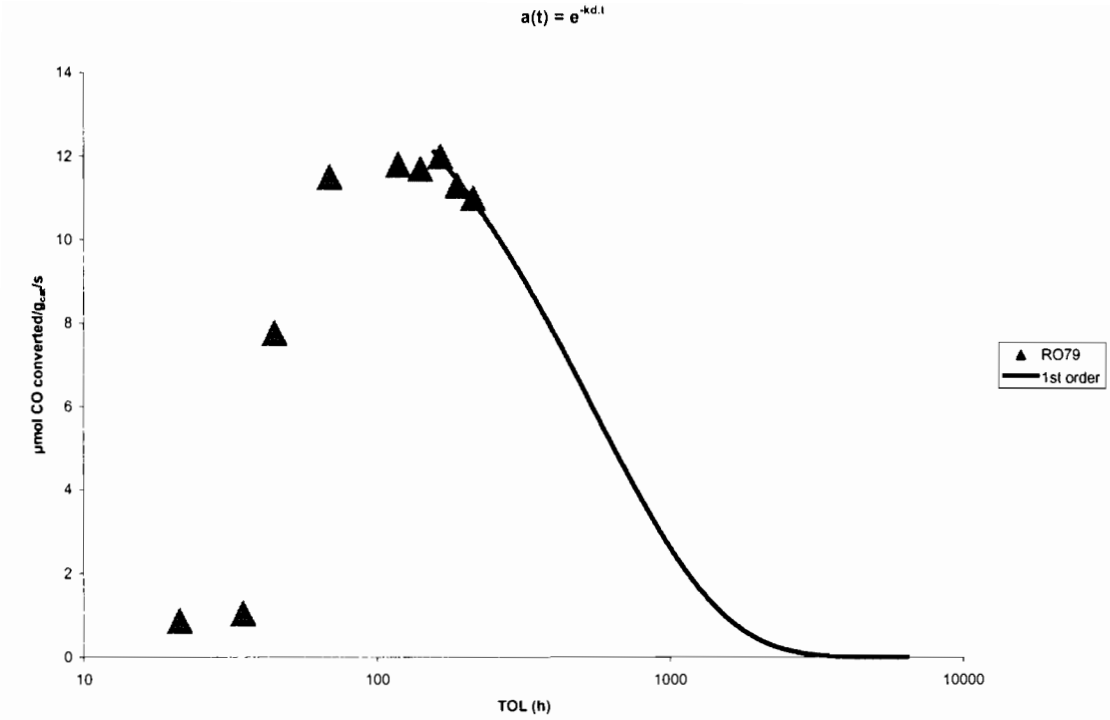


**Figure 4.16** Predicted long-term deactivation behaviour for run R079 according to the rate equation $a = e^{-k_d t}$

#### 4.2.1.3 Fitting data to the equation -da/dt = $k_d$/a

Solving for $a$ yields the following equation (see Appendix B):

$$a = k_d.t[(1-n)+1]^{[1/(1-n)]} \qquad (4.3)$$

Figure 4.17 shows the deactivation profile for run C046 as well as the values obtained by fitting the data to the above rate equation.

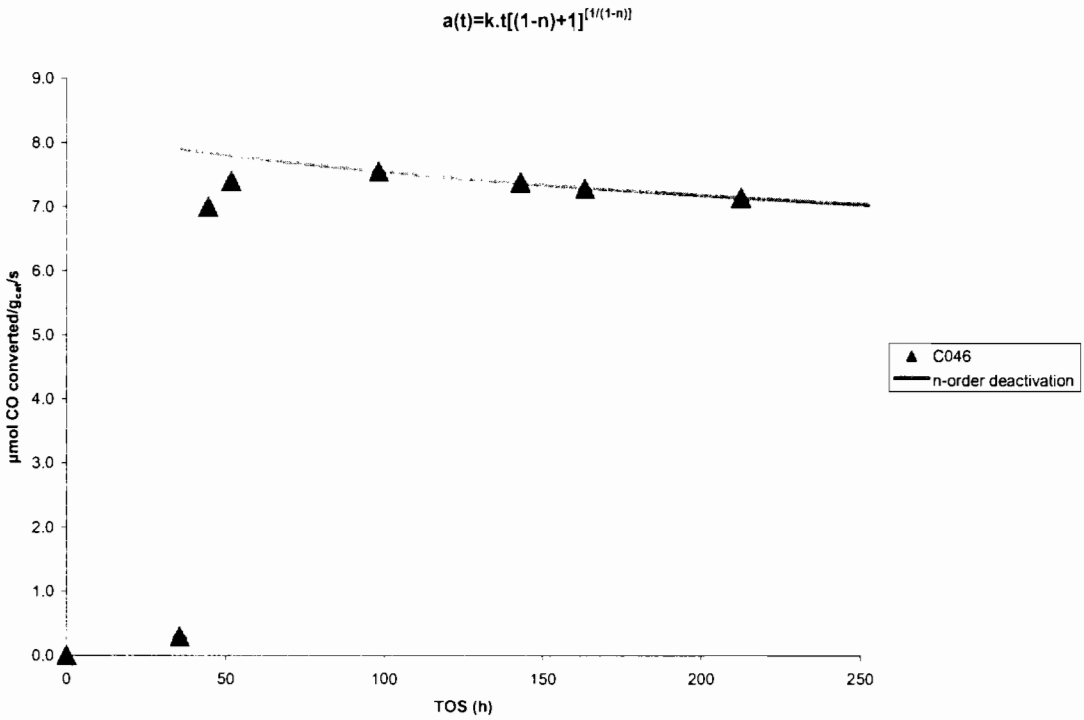


**Figure 4.17** Comparison between deactivation profiles and values obtained after fitting run data to the rate equation

From the above again it can be seen that the actual activity values and those predicted by the rate equation are quite similar. The predicted long-term behaviour is shown in Figure 4.18. The predicated deactivation rate appears to slow somewhat with time on stream. This would be consistent with initial deactivation due to one type of mechanism followed by a different type resulting in slower deactivation.

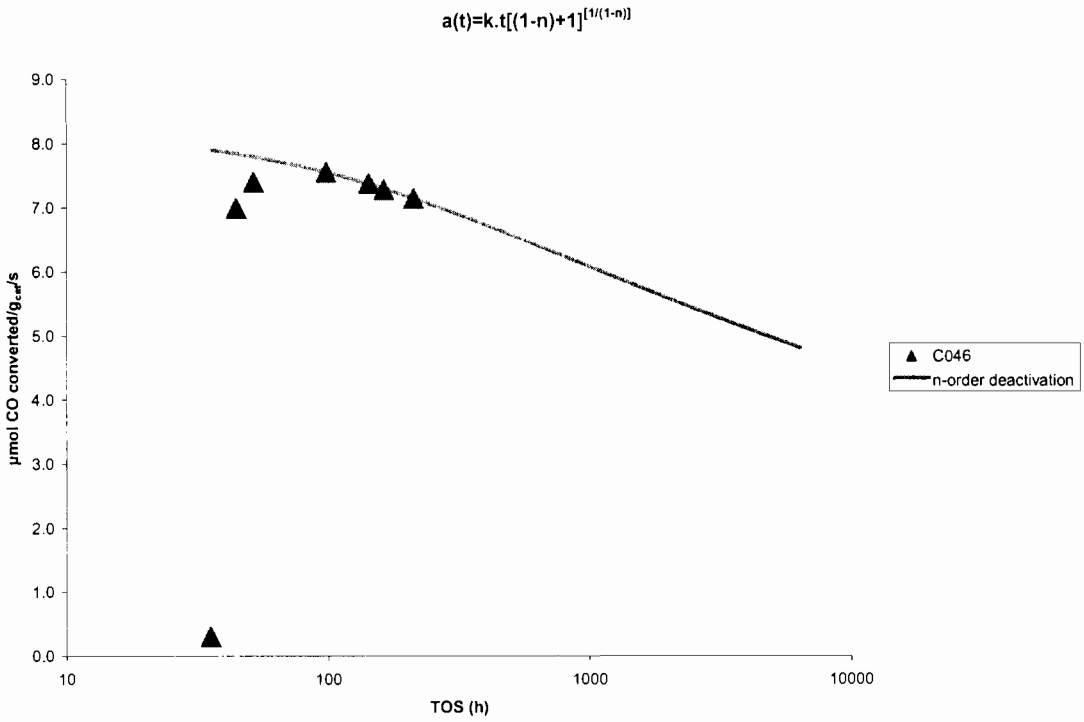


**Figure 4.18** Predicted long-term deactivation behaviour for run C046 according to the rate equation

In the case of run R079 however, a good fit of the predicted and actual values could unfortunately not be achieved suggesting then that only one type of deactivation mechanism is at play for R073 and R079.

#### 4.2.1.4 Speculation as to Mechanisms of Deactivation Occurring

From Figure 4.8 it can be seen that activation with CO resulted in a gradual deactivation from relatively soon after switching to Fischer-Tropsch synthesis with a synthesis gas $H_2/CO$ ratio of 1.0. It was speculated in section 4.1.2 that sintering, along with carbon deposition, could be responsible for the low Fischer-Tropsch activity of run C046 despite the fact that a high percentage of iron carbide would have formed during activation. If one then combines this with the fact that the Voorhies equation, the equation describing exponential deactivation and the equation describing combination deactivation mechanisms all fit the actual data for run C046, the above speculation becomes plausible.

Firstly, the Voorhies equation describes carbon deposition. Under the Fischer-Tropsch synthesis conditions employed this would be an irreversible deactivation mechanism, which is described by the exponential deactivation rate equation (Equation 4.2). Secondly, since the rate equation describing a combination of deactivation mechanisms (Equation 4.3) also fits the data for run C046, and with evidence of sintering (also an irreversible deactivation mechanism at the Fischer-Tropsch conditions employed) from TEM, it follows then that the most likely mechanism of deactivation for run C046 is a combination of sintering and carbon deposition.

Although the deactivation profile for run R076 is similar to run C046, it cannot be said with certainty, in the absence of TEM images for the this sample, whether deactivation in this case was also a combination of sintering and fouling due to carbon deposition. R076 was activated with synthesis gas having an $H_2/CO$ ratio of 1.0 which would have resulted in half the iron carbide content as compared to a CO activated sample such as C046. This in turn would have resulted in initial low Fischer-Tropsch activity with deactivation brought about by fouling due to carbon deposition from the high CO content synthesis gas used during the Fischer-Tropsch synthesis. Seeing as the exponential deactivation rate

equation (Equation 4.2) fits the actual data for run R076, fouling due to carbon deposition is most likely the mechanism in this case.

For run R079, it was seen that the Voorhies equation and rate equation describing exponential deactivation (Equation 4.2) fitted the actual data. However, the rate equation describing a combination of deactivation mechanisms does not fit the data for R079. This would imply that only one deactivation mechanism is at play for run R079 as most likely it is for R073. A clue to the deactivation mechanism taking might be found by looking at the TEM image of the spent catalyst of run R073 (Figure 3.18a). A large crystallite, approximately 50 nm in size, is visible whereas no such structures were apparent after activation with synthesis gas having an $H_2/CO$ ratio of 2.0 (Figure 3.17b). This would suggest that sintering is the single deactivation mechanism taking place for runs R073 and R079, and at the Fischer-Tropsch synthesis conditions employed, this would be irreversible. Although the Voorhies equation fits the actual data for these two runs, fouling due to carbon deposition would be unlikely due to the relatively high $H_2/CO$ synthesis gas ratio of 2.0 used during the Fischer-Tropsch synthesis.

# 5 Conclusions

It was hypothesized that although CO, according to literature, is a superior activating gas, it results in more rapid catalyst deactivation due to carbon deposition. To this end a set of runs were performed in order to prove or disprove the stated hypothesis

From the activation and synthesis runs done, it was observed that the activation procedure certainly had an effect on catalyst performance during the Fischer-Tropsch synthesis.

CO activation resulted in the formation of a larger percentage of iron carbides. When combined with a synthesis gas $H_2/CO$ ratio of 2.0 during the Fischer-Tropsch synthesis it resulted in the highest activity. On the other hand, CO activation combined with a synthesis gas $H_2/CO$ ratio of 1.0 during the Fischer-Tropsch synthesis resulted in activity which was not only lower, but set in almost immediately after switching to synthesis conditions. This proved to be the case with a catalyst activated and subjected to the Fischer-Tropsch synthesis with a synthesis gas $H_2/CO$ ratio of 1.0 as well. Deactivation was thus found to be more a function of the Fischer-Tropsch synthesis conditions as apposed to the activation conditions; carbon deposition due to the low $H_2/CO$ ratio of the synthesis gas possibly being the cause of more rapid deactivation.

Deactivation rate equations, including that which would describe deactivation due to carbon deposition, were fitted to the data obtained for each run. The deactivation rate equations fitted the actual data quite well and therefore could support the speculation that deactivation in a catalyst activated with CO and subjected to the Fischer-Tropsch synthesis with a low $H_2/CO$ ratio is due to carbon deposition.

Furthermore it was speculated that carbon deposition resulted in the inhibition of the cycle of dynamic transitions proposed by van Steen *et al.* (2008) which is required to maintain activity of a precipitated iron-based

Fischer-Tropsch catalyst. The inhibition of these dynamic transitions could then lead to other contributing deactivation mechanisms such as sintering.

In conclusion it can therefore be said that CO activation alone does not lead to more rapid deactivation, but that CO activation combined with a low $H_2$/CO ratio synthesis gas during the Fischer-Tropsch synthesis is the main factor in lower activity and more rapid deactivation.

# References


1. Raje, A., Inga, J.R., Davis, B.H., *Fuel*, **76**, 1997, 273

2. A.P. Steynberg and M.E. Dry (Eds.), *Fischer-Tropsch Technology*, Elsevier (2004)

3. Spath, P.L., Dayton, D.C., *Technical and Economic Assessment of Synthesis Gas to Fuels and Chemicals with Emphasis on the Potential f or Biomass-Derived Syngas*, National Renewable Energy Laboratory Technical Report, December 2003

4. Guettel, R., Kunz, U., Turek, T., *Chemical Engineering & Technology*, **31**, 2008, 746

5. Aruvian Research Market Study Report, *Analyzing Gas to Liquids Market*, January 2008

6. CERA Report, *The Potential of Coal-to-Liquids*, July 2008

7. Wang, J., Jiang, M., Yao, Y., Zhang, Y., Cao, J., *Fuel*, **88**, 2009, 1572

8. Friedmann, S.J., Upadhye, R., Kong, F.M., *Energy Procedia*, **1**, 2009, 4551

9. G.P. van der Laan, A.A.C.M., Beenackers, *Catalysis Reviews – Science and Engineering*, **4** (1999), 255.

10. van Steen, E., Claeys, M., *Chemical Engineering and Technology*, **31**, 2008, 655

11. Bartholomew, C.H., *Applied Catalysis A: General*, **212**, 2001, 17

12. Bukur, D.B., Nowicki, L., Manne, R.K, Lang, X., *Journal of Catalysis*, **155**, 1995, 366.

13. Davis, B.H., *Catalysis Today*, **84**, 2003, 83

14. Luo, M., Davis, B.H., *Fuel Processing Technology*, **83**, 2003, 49

15. Bukur, D.B., Lang, X., Ding, Y., *Applied Catalysis A: General*, **186**, 1999, 255

16. Shroff, M.D., Kalakkad, D.S., Coulter, K.E., Kohler, S. Harrington, M.S., Jackson, N.B., Sault, A.G., Datye, A.K., *Journal of Catalysis*, **156**,1995, 185.

17. Herranz, T., Rojas, S., Perez-Alonso, F.J., Ojeda, M., Terreros, P., Fierro, J.L.G., *Journal of Catalysis*, **243**, 2006, 199

18. Raupp, G.B., Delgass, J., *Journal of Catalysis*, **58**, 1979, 361

19. Bengoa, J.F., Alvarez, A.M., Cagnoli, M.V., Gallegos, N.G., Marchetti, S.G., *Applied Catalysis A: General*, **325**, 2007, 68

20. Emmett, P.H. (Ed.), "*Crystallite Phase and Their Relationship to Fischer-Tropsch Catalysis*", Reinhold, New York, 1956, p 407

21. Bukur, D.B., Okabe, K., Rosynek, M.P., Li, C., Wang, D., Rao, K.R.P.M.,.Huffmann, G.P., Journal of Catalysis, **155**, 1995, 353

22. Barton, G.H., Gale, B., *Acta Crystallographica*, **17**, 1964, 1460

23. Mansker, L.D., Jin, Y., Bukur, D.B., Datye, A.K., *Applied Catalysis A: General*, **186**, 1999, 277

24. Jung, H., Thomson, W.J., *Journal of Catalysis*, **139**, 1993, 375

25. Moulijn, J.A., van Diepen, A.E., Kapteijn, *Applied Catalysis A: General*, **212**, 2001, 3

26. Bartholomew, C.H., Farrauto, R.J., "*Fundamentals of Industrial Catalytic Processes*", John Wiley & Sons, Inc.,2nd ed. (2006), p 294

27. J.L. Figueiredo (Ed), "*Progress in Catalyst Deactivation*", Martinus Nijhoff Publishers (1982), p 31

28. Niemantsverdriet, J.W., van der Kraan, A.M., *Journal of Catalysis*, **72**, 1981, 385

29. Eliason, S.A., Bartholomew, C.H., *Applied Catalysis A: General*, **186**, 1999, 229

30. Kock, A.J.H.M., de Bokx, P.K., Boellaard, E., Klop, W., Geus, J.W., *Journal of Catalysis*, **96**, 1985, 468.

31. de Bokx, P.K., Kock, A.J.H.M., Boellaard, E., Klop, W., Geus, J.W., *Journal of Catalysis*, **96**, 1985, 454

32. Fogler, H.S., "*Elements of Chemical Reaction Engineering*", Prentice-Hall, 3rd ed. (1999),p 635

33. Levenspiel, O., *The Chemical Reactor Omnibook*, OSU Bookstores, (1979), p 31.1

34. Voorhies, A., Journal of Industrial Engineering and Chemistry, **37**, 1945, 318

35. Niemantsverdriet, J.W., "*Spectroscopy in Catalysis*", Wiley-VCH, 2007

36. Malherbe, J.A., *The Effect of Catalyst Pre-Treatment on the Mechanical Integrity and Synthesis Performance of an Iron Based Fischer-Tropsch Catalyst*, Masters Thesis, University of Cape Town, 2006

37. Govender, N.S., *Recycling the Tail-Gas during the Low-Temperature Fischer-Tropsch* Process, Masters Thesis, University of Cape Town, 2005

38. Sasaki, S., *Acta Crystallographica B*, **53**, 1997, 762

39. Hartridge, A., Bhattacharya, A.K., Sengupta, M., Majumdar, C.K., Das, S., Chintalapudi, S.N., *Journal of Magnetism and Magnetic Materials*, **176**, 1997, 89

# Appendix A

This section presents the calculation of the amount of carbon deposited on or incorporated into the catalyst at the end of activation for run (R074).

In Figure 3.1 it is shown that the rate of CO conversion increases linearly with time and is *ca.* 0.7 umol/gcat/s after 36 hrs. This rate is the rate of carbon deposition.

Thus by integration after, 36 hrs:
0.5 x 36hrs x 60min/hr x 60s/min x 0.7 umol C/gcat/s = 45360
*i.e.* 45.4 mmol C/$g_{cat}$ has been deposited.

Let it be assumed that the calcined catalyst contains *ca.* 60% Fe, *i.e.* 0.6g Fe/$g_{cat}$. This equates to 10.5 mmol Fe/$g_{cat}$. According to MAS, 17.7% of all iron is present as carbide and would thus mean that there is 1.84 mmol iron carbide per gram of catalyst.

Taking the iron carbide as Hägg carbide, $\chi$-$Fe_5C_2$ would mean that 0.74 mmol carbon is present in the carbide.

# Appendix B

This section presents the derivation of Equation 4.3

If $-da/dt = k_d/a$

$d/dt(a^n) = -nk_d a^{n-1}$

$= nk_d a^{1-n}$

Therefore solving for a becomes

$a^n = nk_d.t(a^{1-n})$

thus

$a = k_d.t[(1-n)+1]^{[1/(1-n)]}$